THE UNIVERSITY of ADELAIDE

Investigation of Narrowband Acousto-Optic Tunable Filters for Semiconductor Laser Tuning

by

Adam James Gambell

School of Physical Sciences

The University of Adelaide

Thesis submitted for the degree of

Master of Philosophy

November 2019

To my family

Abstract

Wavelength tunable sources find applications in areas of laser surgery, optical coherence tomography, material processing, and differential absorption light detection and ranging. Acousto-optic tunable filters (AOTFs) are wavelength selective devices which allow for better stability than mechanical tuning due to their lack of mechanical movement. Agile tunability is achieved by avoiding inertial effects.

The aim of this thesis was to investigate the performance and limitations of AOTF wavelength controlled external semiconductor laser cavities. The three key components of a typical tunable source are outlined. Conventional tuning mechanisms are compared with AOTFs, and different gain media discussed, with semiconductors being identified as suitable for building AOTF tuned sources.

Initially, two diffraction grating tuned sources were constructed. The first was a Thulium doped fibre laser which produced >1.3 W over 1920 – 2060 nm wavelength range which has since been delivered to OzGrav for characterising the absorption of low hydroxide OH bulk fused silica. The second source was constructed from a superluminescent diode with an Indium Phosphide (InP) active layer and produced >5 mW over 1650 – 1750 nm. This source was subsequently used for characterising a frequency shifting, quasi-collinear AOTF for its tuning relation, response to different driving conditions, and temporal response.

Two tunable laser cavities were built using the quasi-collinear AOTF. The first was based on the InP superluminescent diode and demonstrated >10 mW over 1615 – 1775 nm. However, the laser displayed significant etalon effects in its spectral output. This motivated the construction of a ring-cavity based on an InP semiconductor optical amplifier. This laser produced >5 mW over 1600 – 1750 nm, with ~0.3 nm linewidths and no etalon effects observed in the output. Sweep rates of 10^5 nm/s were demonstrated for both lasers without significant spectral broadening or power modulation. This is of similar magnitude to the fastest previously reported quasi-collinear AOTF tuned semiconductor lasers. Wavelength agility was demonstrated by switching between any two wavelengths in the gain band within the 29 μs interaction time of the AOTF.

Finally, a frequency compensating AOTF device was utilised in the ring-cavity to investigate the effect of frequency shift on laser performance. Operating with no frequency shift allowed for a reduction in linewidth, but made the laser more sensitive to residual etalon effects which had not previously been observed with the frequency shifting AOTF ring-cavity. A +30 kHz frequency shift was significant enough to disturb these intracavity interference effects while being small enough to reduce the linewidth from the 0.3 nm observed with the frequency shifting AOTF to <0.1 nm.

Future directions of research are discussed. These include operation at other wavelengths, and investigating dual wavelength operation.

Contents

List of Tables

List of Figures

Declaration of Authorship

I certify that this work contains no material which has been accepted for the award of any other degree or diploma in my name in any university or other tertiary institution and, to the best of my knowledge and belief, contains no material previously published or written by another person, except where due reference has been made in the text. In addition, I certify that no part of this work will, in the future, be used in a submission in my name for any other degree or diploma in any university or other tertiary institution without the prior approval of the University of Adelaide and where applicable, any partner institution responsible for the joint award of this degree.

I give permission for the digital version of my thesis to be made available on the web, via the University's digital research repository, the Library Search and also through web search engines, unless permission has been granted by the University to restrict access for a period of time.

I acknowledge the support I have received for my research through the provision of an Australian Government Research Training Program Scholarship

Signed:_____

Date:_____

Acknowledgements

First I would like to thank my external and co-supervisors Nikita Simakov and Miftar Ganija. Throughout the project you have consistently taken the time to provide useful feedback and suggestions which were always insightful. You have helped improve my laboratory skills immensely and helped me become a more critical thinker. I cannot thank you enough for the opportunities that you have gone out of your way to provide. I count myself fortunate that you accepted me as a student, and it has been a true pleasure working with you.

I would like to thank my principle supervisor Peter Veitch for your continual support over the duration of the project. When writing this thesis you have provided helpful feedback which I am thankful for.

I also owe thanks to Alexander Hemming and John Haub for their ongoing support and the opportunities which they have offered me.

I would like to thank Peter Shardlow and Andrew Clarkson of the University of Southampton and Jon Ward of Gooch & Housego for their expertise in acousto-optic tunable filters and providing the frequency compensating tunable filter pair. Thanks also go to Jae Daniel for his helpful insight into acousto-optically tuned lasers.

I am grateful to Keiron Boyd, Niel Carmody, and Jesper Munch for their helpful discussions regarding experiments and providing laboratory equipment. I also thank Bob Chivell for his technical assistance.

To my colleagues David, Nicholas, Daniel, Jamie, and Tom, thank you for your support throughout this project and the coursework involved.

Finally, I would like to thank my family and friends for their unwavering support and understanding. I appreciate all that you have done for me.

List of Abbreviations

AO	Acousto-optic
AOTF	Acousto-optic tunable filter
AR	Anti-reflection
ASE	Amplified spontaneous emission
CW	Continuous wave
dB	decibels
DBR	Distributed Bragg reflector
DC	Direct current
DFB	Distributed feedback
DIAL	Differential absorption light detection and ranging
FC-AOTF	Frequency compensating acousto-optic filter
FD-OCT	Fourier domain optical coherence tomography
FSR	Free spectral range
FWHM	Full width at half maximum
HR	Highly reflective
IR	Infra-red
MEMS	Microelectromechanical systems
NA	Numerical aperture
NC-AOTF	Non-collinear acousto-optic filter
OC	Output coupler

OCT	Optical coherence tomography
OSA	Optical spectrum analyser
OSNR	Optical signal to noise ration
PM	Polarisation maintaining
PPM	Photodiode power meter
PRM	Polygon rotating mirror
QC-AOTF	Quasi-collinear acousto-optic filter
QCL	Quantum cascade laser
RF	Radio frequency
SLED	Superluminescent diode
SMF	Single-mode fibre
SOA	Semiconductor optical amplifier
SS-OCT	Swept source optical coherence tomography
TD-OCT	Time domain optical coherence tomography
TPM	Thermal power meter
VBG	Volume Bragg grating
WDM	Wavelength division multiplexing

Chapter 1
Introduction

1.1 Overview

Wavelength tunable sources find applications in areas of laser surgery [1], optical coherence tomography [2,3], material processing, and differential absorption light detection and ranging [4,5]. In some cases, it is beneficial to use an agile source which can rapidly tune to arbitrary wavelengths within a broad laser bandwidth.

While many sources are available providing a wavelength tunable output, each one has its own limitations regarding tuning rates, output power, wavelength span, linewidth, stability, and agility. Common methods of wavelength control use diffraction gratings, Fabry-Perot etalons, dielectric mirrors, prisms, volume Bragg gratings, distributed Bragg reflectors, distributed feedback, and current or temperature tuning. Actuation techniques for mechanical tuning methods typically use micro-electromechanical systems or piezoelectric transducers. An alternate method for tuning utilises acousto-optic tunable filters (AOTFs). These are electronically controlled agile filters which can be both continuously and discretely tuned. They may allow for better stability than mechanical tuning due to their lack of movement.

The first acousto-optically (AO) tuned sources were tunable dye lasers [6,7]. Since then, AO tuned sources based on Ti:Al_2O_3 [8,9], rare-earth doped fibres [10], and semiconductors [11,12] have been demonstrated. Previous AO tuned semiconductor

lasers have been focused on specific applications such as optical coherence tomography (OCT) [13–15] or telecommunication sources [11,16]. The aim of this thesis is to perform a complete investigation into the performance and limitations of these types of lasers.

1.2 Applications of tunable sources

1.2.1 Laser surgery

Lasers are used in surgical applications for precision cutting and coagulation of soft tissue due to their ability to achieve small spatial dimensions at high power levels. The laser penetration depth for human skin has strong wavelength dependence as shown in Figure 1.1. The 2 µm region exhibits short penetration depths due to strong water absorption, promoting its use in skin ablation [17]. The absorption of water changes sharply from wavelengths around 1.7 – 2.0 µm, where there is a local maximum and minimum at ~1940 nm and ~1700 nm of 120 cm^{-1} and 4.5 cm^{-1}, respectively [18]. A tunable source built around these wavelengths could potentially be used to create a laser scalpel with a controllable cutting depth [1].

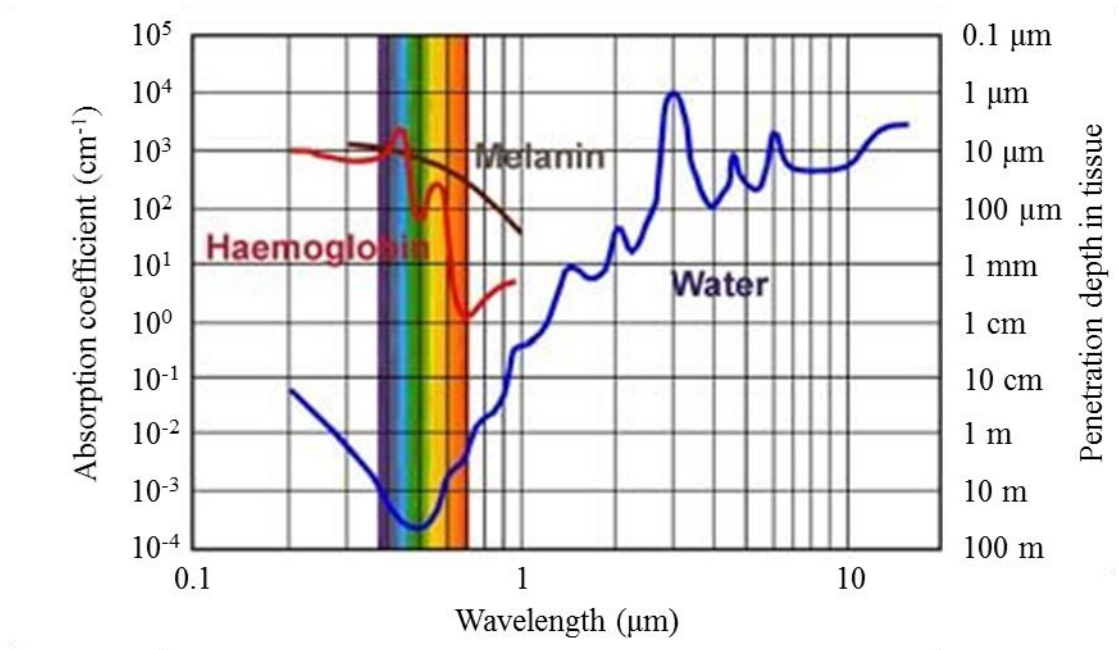

Figure 1.1 Absorption and penetration depth in water and other biological tissue constituents for different wavelengths [17].

1.2.2 Optical coherence tomography

Optical coherence tomography (OCT) is a non-invasive imaging approach able to provide high resolution (µm level) at depths of up to 10's of mm. This has applications in biological imaging [2,3], non-destructive testing [19], and art conservation [20–22]. Figure 1.2 compares the imaging depth and resolution of OCT against other imaging techniques. Where ultrasound provides large penetration depth with lower resolution, and confocal microscopy gives high resolution at small depths, OCT provides a compromise between penetration depth and resolution.

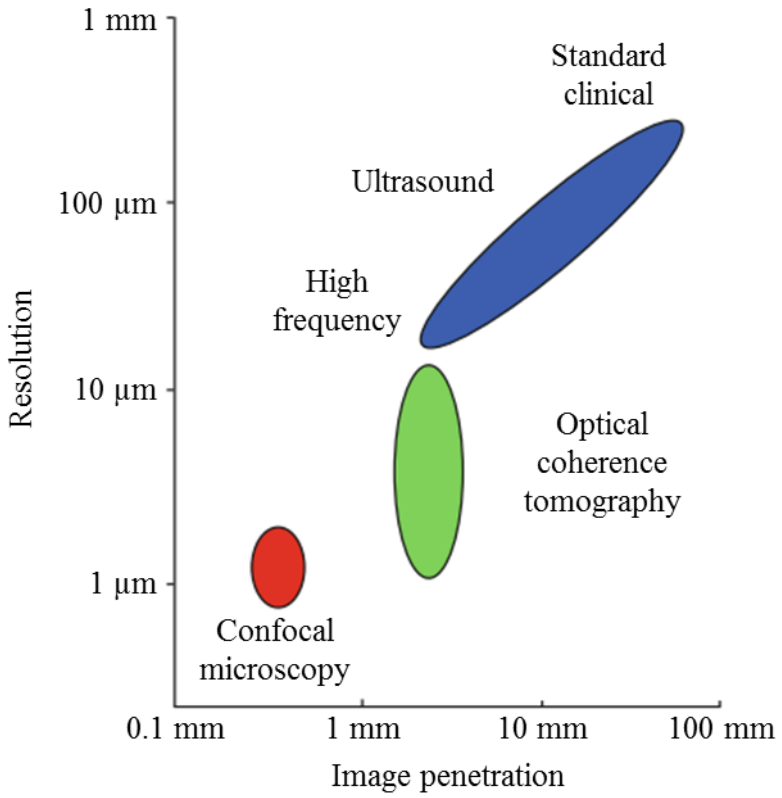

Figure 1.2 Comparison of imaging depth and resolution for various imaging techniques [23]. OCT fills a gap left by the other rapid, non-invasive techniques of ultrasound and confocal microscopy.

The three methods of OCT are time domain OCT (TD-OCT), Fourier domain OCT (FD-OCT) – also known as optical frequency domain OCT or spectral OCT – and swept source OCT (SS-OCT). Both TD-OCT and FD-OCT make use of a broad bandwidth source, while SS-OCT uses a narrow linewidth swept source operating over >50 nm.

The penetration depth of SS-OCT is superior to FD-OCT as demonstrated in Figure 1.3, where a commercial SS-OCT system is compared against conventional SD-OCT.

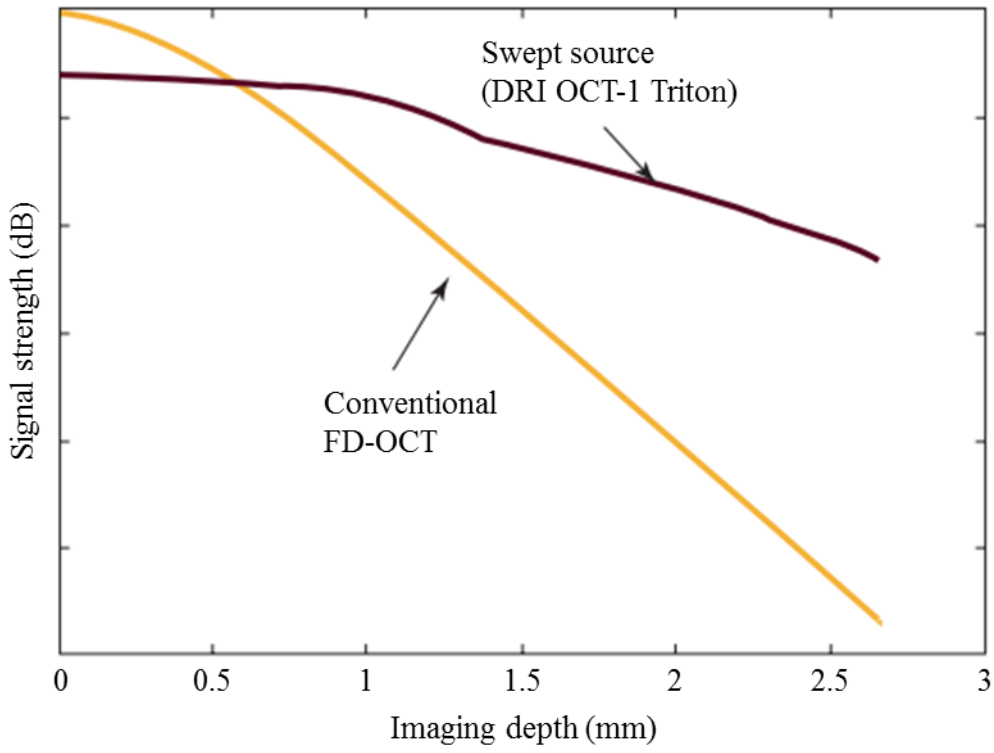

Figure 1.3 Comparison of penetration depth of a SS-OCT system (DRI OCT-1 Triton) with conventional FD-OCT [24].

The performance of a SS-OCT system will be influenced by the swept source's tuning range, wavelength, instantaneous linewidth, and sweep rate. Larger tuning ranges and shorter wavelengths increase axial spatial resolution, while narrower instantaneous linewidths increase the penetration depth [25]. Faster sweep rates enable faster image acquisition, which is desirable for biological imaging where the sample may move.

For biological imaging, the wavelength of OCT sources typically range from 800 nm to 1550 nm [2,3,26]. Shorter wavelengths can give higher resolution, however longer wavelengths can be desirable for use with samples with high optical scattering, such as tissue. The performance parameters of some commercially available SS-OCT systems are shown in Table 1.1. Typical sources for SS-OCT have wavelength spans of >50 nm, output powers in the 10's of mW, and coherence lengths that correspond to instantaneous linewidths in the order of ~0.1 – 0.01 nm.

Table 1.1 Comparison of performance parameters of several commercially available SS-OCT systems [27]. λ_c = central wavelength.

Company	**Sweep frequency (kHz)**	**λ_c (nm)**	**λ span (nm)**	**Coherence length (mm)**	**Output power (mW)**
Axsun	200	1060	100	10	15
	100			12	
	50			18	
	30			50	
	100	1310	140	20	20
Exalos	20	850	60	7	7
	50	1050	90	8	15
	20	1310	150	6	25
NTT	200	1310	100	7	17
Micron optics	100	1310	150	3	>35
Santec	20	1060	120	3	12
	50	1310	140		15
	100	1310	>100	>16	50
		1550			
Insight photonics	100	1310	100	>100	>6
		1550	40	>40	5.5
Thorlabs	100, 200	1310	100	100	25
Optores	750, 1500	1060	>100	~6	>100
		1310			
		1550			

For art restoration, the non-invasive 3D imaging approach of OCT provides advantages over other destructive examination techniques. OCT can be performed over an entire art

piece giving a more complete representation than destructive testing which relies on small samples, typically taken over areas already containing losses or cracks.

For imaging paintwork, the scattering of pigments at wavelengths <2 µm, and the absorption of egg tempura at wavelengths >2.25 µm suggests an optimum operating wavelength region of 2.0 – 2.2 µm [21,28,29]. If higher resolution images are desired, a source based around 1.6 – 2.0 µm could potentially be used at the expense of reduced imaging depth.

1.2.3 Material processing

Lasers have many uses in material processing for welding, ablation, cutting, and engraving. The absorption of different polymers over a 1.6 mm thickness is shown in Figure 1.4. The strong absorption features around 1700 nm due to C-H bond resonant overtones could allow laser welding and processing without using absorption enhancing additives [30].

A wavelength tunable source would allow access to different penetration depths and targeting of specific plastics for heating. If continuously tuning through wavelengths, the source may span absorption features of other polymers, leading to unwanted heating. An agile source that can discretely change its wavelength could avoid this issue.

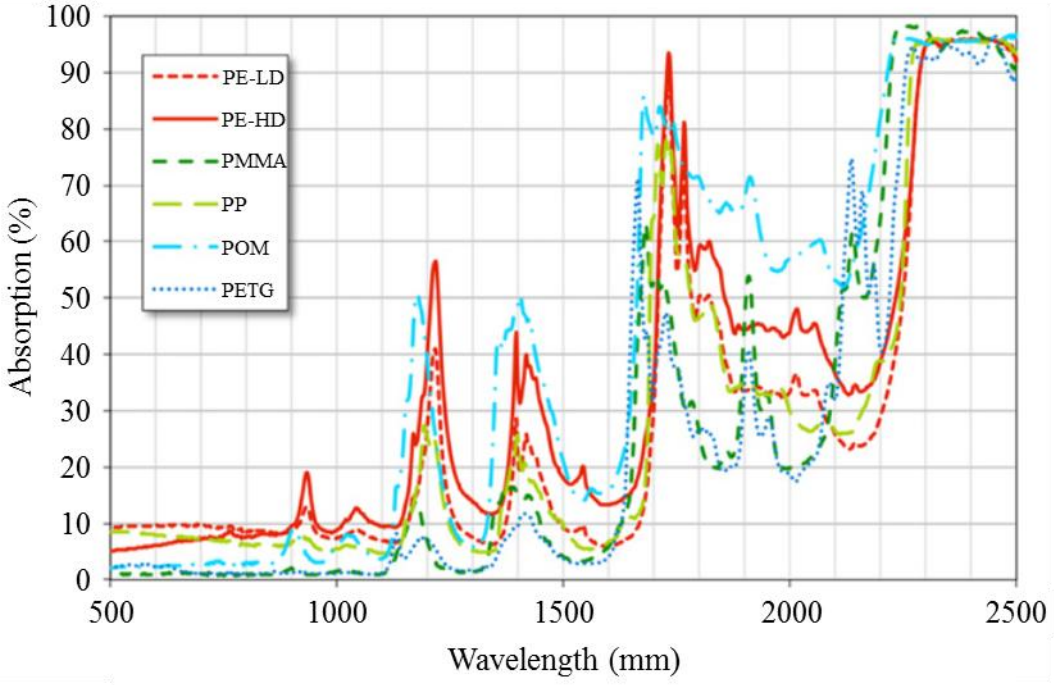

Figure 1.4 Absorption spectra for various polymers over a 1.6 mm sample thickness [31]. PE-LD = low density polyethylene, PE-HD = high density polyethylene, PMMA = polymethylmethacrylate, PP = polypropylene, POM = polyoxymethylene, PETG = glycol-modified polyethyleneterephthalate.

1.2.4 Differential absorption light detection and ranging

Differential absorption light detection and ranging (DIAL) is a remote sensing technique for measuring gases in the atmosphere by switching between an "online" wavelength which is absorbed by the gas of interest and an "offline" wavelength with no absorption. Typically, to switch between "online" and "offline" wavelengths or multiple absorption features of different species, DIAL instruments use either a swept tunable source [4,5], or several fixed wavelength sources which are switched on and off by electro-optic switches [32,33] or micro electromechanical systems (MEMS) [34].

An alternate method to the swept source would be to use a wavelength agile source which can discretely move between wavelengths. The advantage of such a source is shown in Figure 1.5, where the agile source eliminates the unnecessary time taken sweeping between two different absorption features. Consequently, this can improve integration times compared with the wavelength swept source.

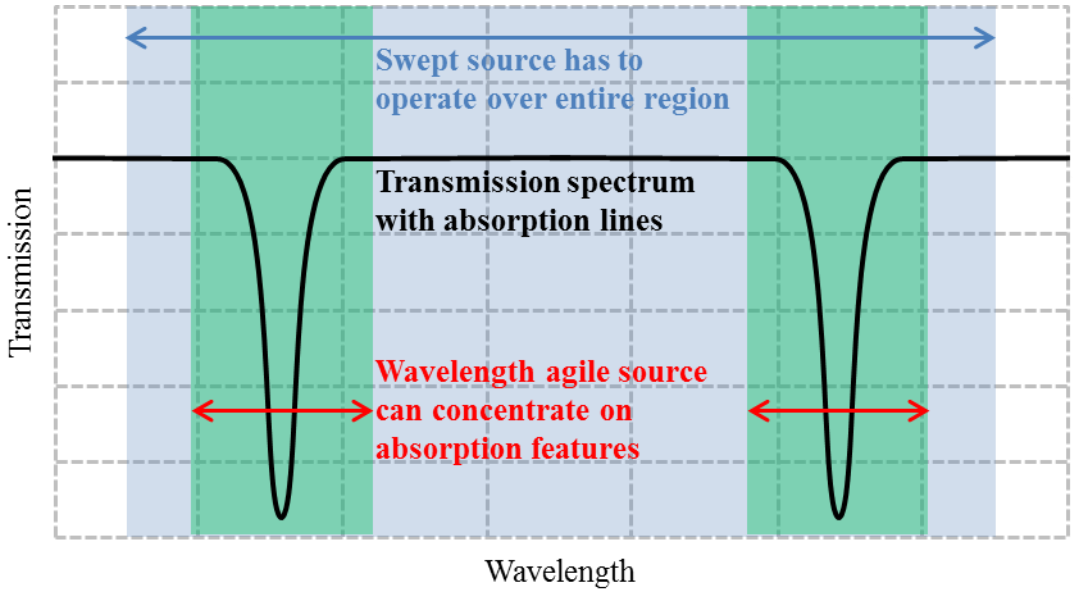

Figure 1.5 Illustration of absorption features and operation of a typical swept source in comparison to a wavelength agile source which may discretely move between wavelengths [35].

1.2.5 Summary

Tunable sources find applications in a wide range of applications, some of which were discussed. Agile sources which can discretely switch between wavelengths is attractive in areas of laser surgery, material processing, and DIAL, where operation at intermediate wavelengths is not of use, or can lead to unwanted absorption. Rapidly wavelength swept sources are ideal for SS-OCT, where 10's of kHz sweep rates and >50 nm tuning ranges are desired with <0.1 nm instantaneous linewidths. Throughout this thesis the performance and limitations of AOTF wavelength controlled external semiconductor cavities will be investigated.

1.3 Outline of thesis

Chapter 1 gave an overview of the applications for tunable wavelength laser sources. These include laser surgery, optical coherence tomography, material processing, and differential absorption light detection and ranging. Emphasis was given to how an agile source, which may discretely change wavelength or be rapidly swept, is advantageous in these areas.

Chapter 2 outlines the typical components which make up a tunable source, which includes the tunable filter, gain media, and cavity configuration. The influence of each on the operating wavelength is discussed. A variety of tunable filters and gain media are presented, with AOTF's and semiconductors identified as suitable for constructing agile sources.

Chapter 3 involves the design and construction of two grating tuned, continuous wave (CW) lasers based on fibre and semiconductor gain media. A 2 μm tunable thulium-doped fibre laser is built for characterising optical absorption in low-OH fused silica. This is necessary to understand for possible upgrades in the next generation gravitational wave detectors, which may operate around the 2 μm wavelength. The semiconductor laser is based on a superluminescent diode (SLED) gain medium and is suitable for characterising optical devices such as the AOTF used in subsequent chapters.

In Chapter 4, an overview of AOTFs is presented including some background theory of operation, and a comparison between different AOTF types. Following this, a quasi-collinear AOTF is characterised using the grating tuned semiconductor laser source from Chapter 3. A tuning curve is obtained for both input polarisations, and curves of diffraction efficiency vs acoustic frequency and RF power are obtained. The optical filter bandwidth is determined, and the AOTF's temporal response investigated. The measurements are compared with theory and the AOTF specifications for validation.

In Chapter 5, the AOTF characterised in Chapter 4 is used to build two tunable semiconductor lasers. The first uses the same SLED gain media as the grating tuned laser from Chapter 3. Steady state, wavelength swept, and wavelength agile operation regimes of this laser are investigated. Etalon effects are observed in its spectrum, which are attributed to reflections within the gain media. A second laser is built based a semiconductor optical amplifier (SOA) gain medium in a ring-cavity. This laser is characterised, and the low reflections in the SOA are shown to reduce the etalon effects in the laser output.

In Chapter 6, the single AOTF that was used to tune both laser cavities from Chapter 5 is replaced with a frequency compensating AOTF (FC-AOTF) pair. The FC-AOTF pair

has a net frequency shift orders of magnitude smaller than that of a single AOTF device, and can be driven to produce no frequency shift at all. The possible advantages that such a device can have on laser performance are investigated by characterising the SOA ring-cavity with the FC-AOTF pair acting as the spectral filter.

Chapter 7 reviews the capabilities and limitations discovered when using AOTFs as the tuning element of lasers. Future directions for research are also highlighted, including transitioning to other wavelengths, and investigating dual wavelength operation.

Chapter 2
Background

2.1 Introduction

The aim of this chapter is to outline the influence that gain media, tunable filters, and cavity design has on the tuning range, tuning rate, and operating wavelength of the laser. A variety of tunable filters and gain media are presented and compared, with focus placed on their usefulness in constructing widely tunable, agile sources.

2.2 Tunable laser basics

Examples of tunable laser cavity models for both standing wave and ring cavities are shown in Figure 2.1(a) and (b), respectively. The standing wave cavity consists of a gain medium and tunable filter placed between a highly reflective (HR) mirror and partially reflective output coupler (OC). The HR mirror and OC provide feedback to increase the circulating intra-cavity power. The OC is partially reflective to allow some light to be transmitted as useful output. The tunable filter provides wavelength control of the laser through its wavelength dependent response.

The ring cavity is similar to the standing wave cavity in that it has a gain medium, HR mirrors and OC, and a tunable filter. However, its geometry is such that light travels in a ring rather than folding back in on itself as done in the standing wave cavity. Additionally, it includes an isolator to block light travelling anticlockwise in the figure,

while transmitting in the other direction. Together the isolator and cavity geometry force light to travel clockwise.

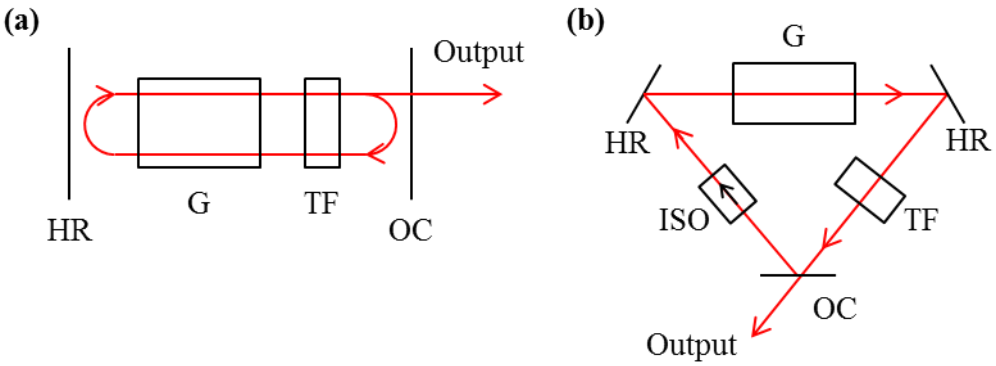

Figure 2.1 Example of tunable laser cavity models. (a) Standing wave cavity. (b) Ring cavity. G = gain medium, TF = tunable filter, ISO = isolator, HR = highly reflective mirror, OC = output coupling mirror.

2.3 Longitudinal modes

The permitted wavelengths at which lasing action can occur are restricted to those which constructively interfere after a round trip of the cavity. These wavelengths are known as the cavity longitudinal modes. The free spectral range (FSR) of the cavity is the separation in frequency space of these modes and is given by [36]

$$\mathrm{FSR} = \Delta\nu = \begin{cases} \dfrac{c}{2n_{eff}L}, & \text{Standing wave cavity} \\ \dfrac{c}{n_{eff}L}, & \text{Ring cavity} \end{cases} \qquad \textbf{2.1}$$

where ν is the frequency of light, L is the cavity length, n_{eff} is the effective refractive index over the cavity length L, and c is the vacuum speed of light. The FSR in frequency space can be mapped to a longitudinal mode spacing $\Delta\lambda$ in the wavelength domain:

$$\Delta\lambda = \frac{c}{\nu^2}\Delta\nu = \frac{\lambda^2}{c}\Delta\nu = \begin{cases} \dfrac{\lambda^2}{2n_{eff}L}, & \text{Standing wave cavity} \\ \dfrac{\lambda^2}{n_{eff}L}, & \text{Ring cavity} \end{cases} \qquad \textbf{2.2}$$

2.4 Operating wavelength of a laser cavity

An example of the laser output using a narrow and broad tunable filter is shown in Figure 2.2(a) and (b), respectively. The laser operates on the cavity longitudinal modes, and ideally the operating modes are determined by the tunable filter alone. Typically, the intra-cavity and output coupling losses are wavelength independent and do not influence the lasing wavelength of the cavity. However, the presence of any unwanted intra-cavity interference may also lead to a wavelength dependent loss, thereby affecting the output wavelength of the laser. The mode(s) which lase will be the ones with the lowest threshold.

If the filter is narrower than any wavelength dependent variation in intra-cavity interference as shown in Figure 2.2(a), then lasing can occur over the tunable filter's peak. However, if the filter is too broad as shown in Figure 2.2(b), then other factors such as the intra-cavity etalons can become more dominant in determining the operating longitudinal modes of the laser. This is a common feature of tunable lasers exhibiting intra-cavity etalons, where in some cases lasing only occurs at the peaks of the etalon interference curve. These peaks are sometimes referred to as etalon modes.

Laser operation on a single longitudinal mode is possible if the longitudinal modes are spaced far enough apart such that only one mode is above threshold for lasing.

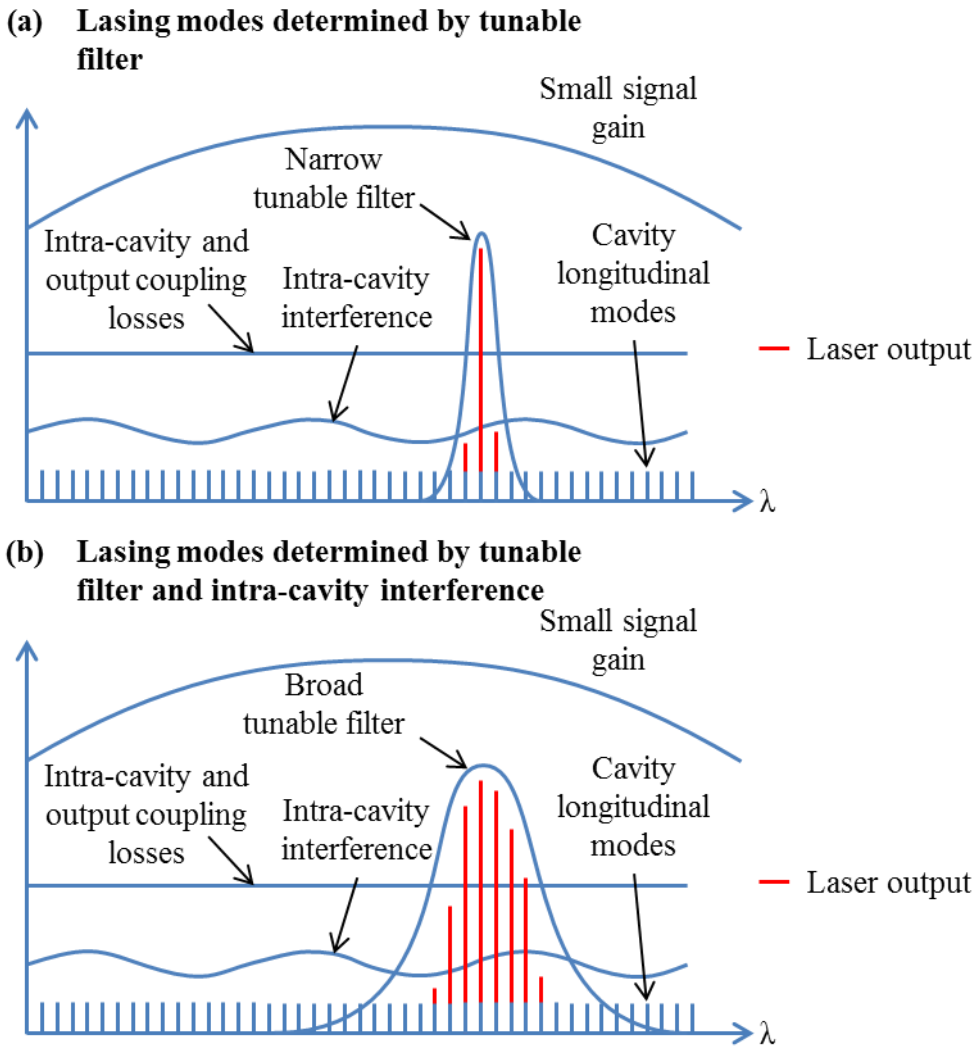

Figure 2.2 Example of the combined effect of a tunable filter and intra-cavity interference on the laser output of a cavity when using a narrow tunable filter in (a), and a broad tunable filter in (b).

The laser output when attempting to continuously tune the filter is shown in Figure 2.3. When moving the filter in the case of a laser operating on multiple longitudinal modes as shown in Figure 2.3(a), then as one mode stops lasing another may appear. The end result is that the spectral envelope appears to move continuously, but the modes operating within the envelope maintain a discrete position as determined by the cavity FSR.

If the laser operates on a single longitudinal mode as shown in Figure 2.3(b), the lasing mode will switch to the next adjacent longitudinal mode as the filter is tuned. If the longitudinal modes are static, then continuously tuning the filter will correspond to the

laser hopping between adjacent cavity longitudinal modes. If the modes can be moved by changing the cavity length or adjusting the round trip phase at the same rate as moving the filter, then true continuous tuning is possible for single longitudinal mode lasers.

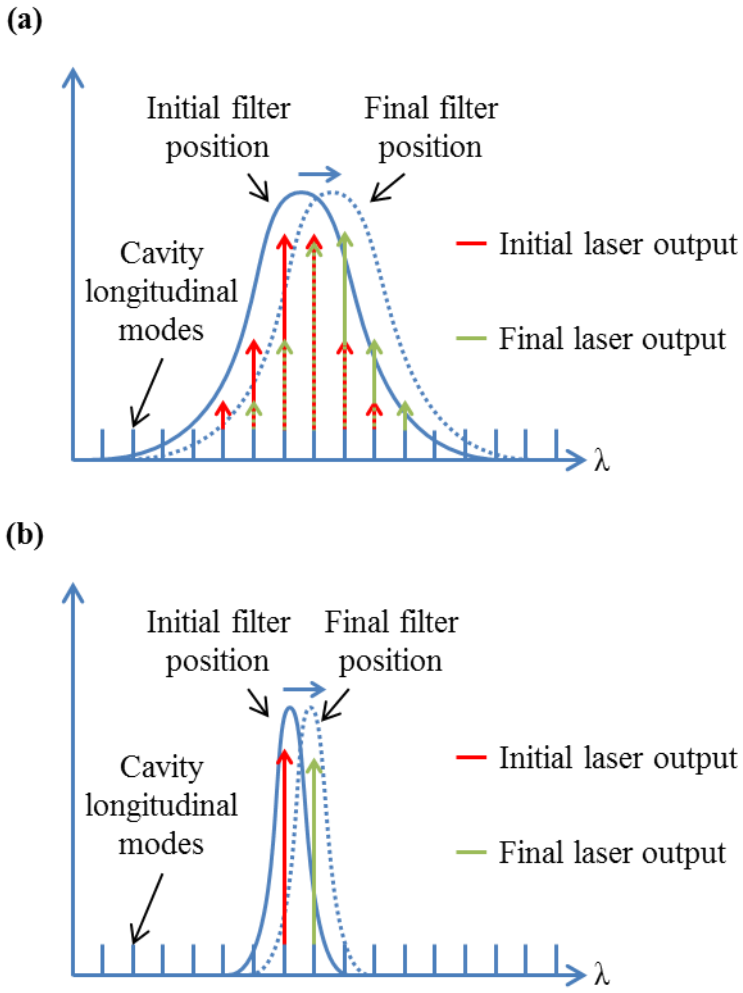

Figure 2.3 Laser output when attempting to continuously tune the spectral filter. In (a), a broad filter is used such that the laser operates on multiple longitudinal modes. In (b), a narrow filter is used such that the laser operates on a single longitudinal mode.

2.4.1 Frequency shifting filter

If the tunable filter used is frequency shifting such that filtered light will be frequency shifted by $\pm f$, this will affect the modes in the cavity. An example of how such a filter affects the dynamics of the laser modes for a positive frequency shift is shown in Figure 2.4. Four lasing modes are present and on interacting with the filter are

frequency shifted by $+f$. After travelling one round trip of the cavity the light from each mode is no longer at the same wavelength. Thus the constructive interference condition described in Section 2.3 for the longitudinal cavity modes is invalid. As such, the condition for forming longitudinal cavity modes is no longer valid for lasers tuned with this type of filter.

It is also feasible that strong intra-cavity etalon modes may also be prevented from forming by using a frequency shifting filter.

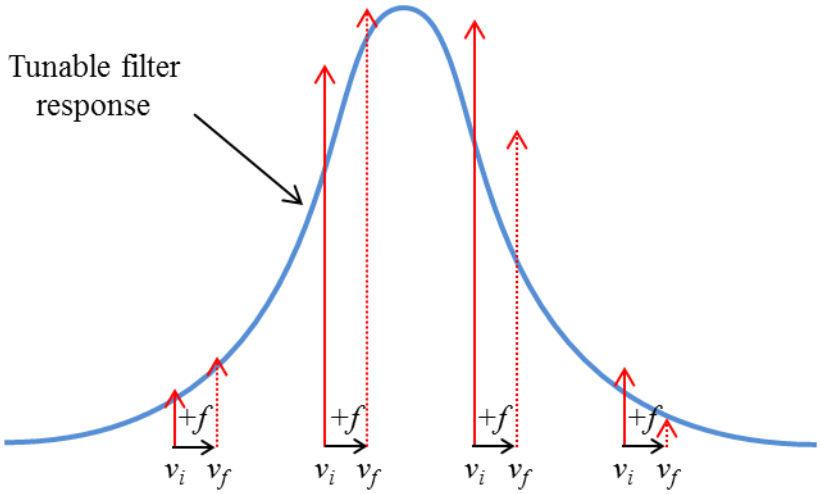

Figure 2.4 Movement of laser modes due to intra-cavity frequency shifting tunable filter. f = frequency shift of optical light due to filter, v_i = initial optical frequency, v_f = optical frequency after being shifted by filter.

2.5 Tunable filters

A variety of spectral filtering mechanisms exist which can be used for tuning the wavelength of a laser cavity. Some rely on mechanical movement while others use temperature or strain tuning, or are electronically controlled. Several commonly used tuning methods are described here and their suitability for agile tuning over a broad wavelength region discussed.

2.5.1 Diffraction grating

Diffraction gratings are one of the most common wavelength tuning mechanisms. They consist of a substrate with periodic grooves and can be reflective or transmissive

depending on the substrate. Light interacting with each groove of the grating creates a set of wavelets [37]. These wavelets will interfere constructively at specific angles which are dependent on the wavelength of light being used. This is shown in Figure 2.5 for a reflective blaze diffraction grating. The relation between diffraction angle α, input angle β, wavelength λ, and the groove spacing d of the grating is given by the grating equation [37],

$$m\lambda = d(\sin\alpha - \sin\beta). \qquad \textbf{2.3}$$

Where α and β are measured with respect to the grating normal, and m is an integer corresponding to the diffraction order.

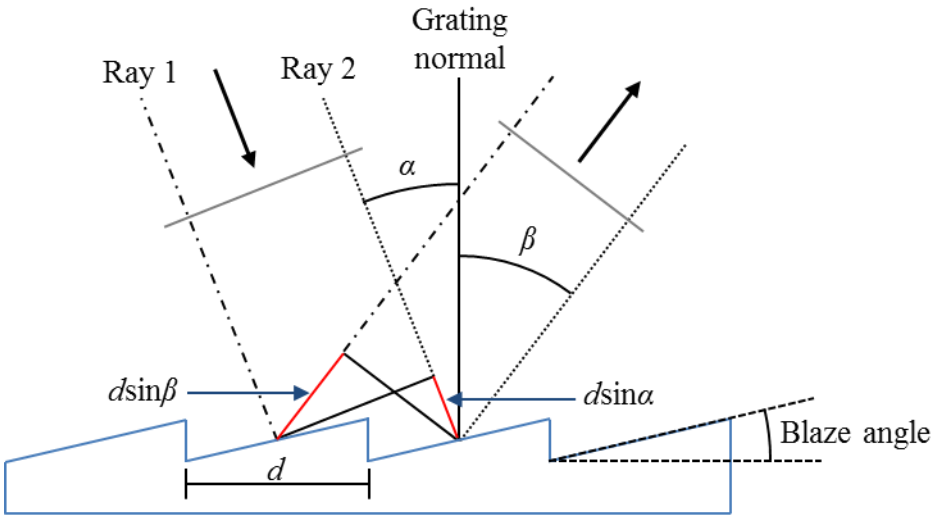

Figure 2.5 Geometry for diffraction off a planar blazed reflective grating. Ray 1 and 2 are parallel rays from a planar wavefront. Adapted from [37].

The theoretical resolving power R for a planar diffraction grating is [37]

$$R = \frac{\Delta\lambda}{\lambda} = \frac{Nd(\sin\alpha + \sin\beta)}{\lambda}, \qquad \textbf{2.4}$$

where $\Delta\lambda$ is defined such that the peaks of two wavelengths separated by greater than $\Delta\lambda$ will be unambiguous. N is the total number of grooves illuminated on the grating surface.

When used for laser tuning, diffraction gratings allow broad tunability typically in the order of 100's of nm. Single longitudinal mode operation of diffraction grating tuned semiconductor lasers are typically be achieved through expanding the optical beam at the grating.

2.5.2 Fabry-Perot etalon

Fabry-Perot etalons consist of two parallel surfaces such that incoming light is transmitted when light is resonant between the surfaces. Two examples are shown in Figure 2.6(a) and (b). In Figure 2.6(a), the etalon consists of two reflective coated surfaces separated by distance *d* on a substrate of refractive index *n*, while in Figure 2.6(b) it consists of an air gap between two spacers separated by distance *d* of refractive index *n*.

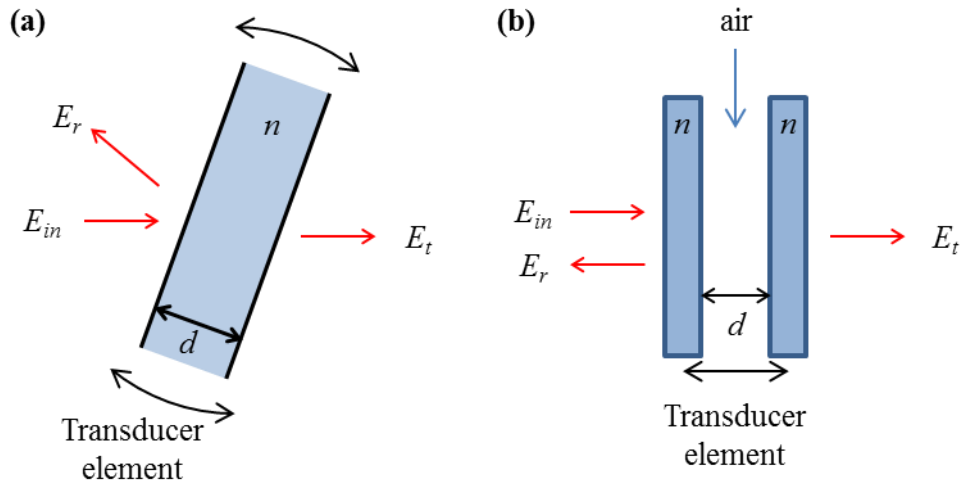

Figure 2.6 Filtering light with two Fabry-Perot etalon types. E_{in} = incident light, E_r = reflected light, E_t = transmitted light.

The resonance condition results in peaks in the transmission at frequencies separated by a FSR. An example transmission function as a function of the optical frequency is shown in Figure 2.7. Each peak (or mode) has a filter bandwidth denoted δv. The filtered frequencies are selected by altering the resonance condition by changing the separation distance *d* or rotating the etalon.

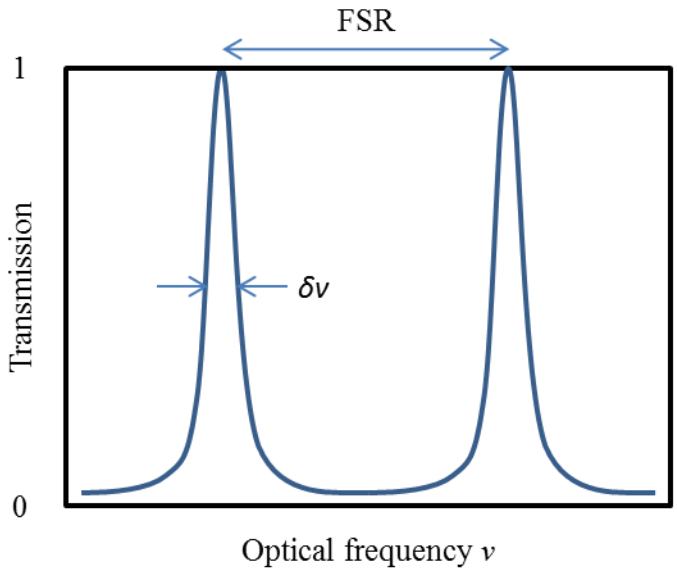

Figure 2.7 Filter transmission of a Fabry-Perot etalon. δv = filter bandwidth, FSR = free spectral range.

If a single etalon is used for tuning, its FSR should be larger than the bandwidth of the gain medium to ensure only a single etalon peak exists across the bandwidth at a given time. Etalons with widths of ~5 μm can achieve FSR's of >100 nm while still maintaining filter bandwidths of $\delta\lambda \sim 0.1 - 0.01$ nm depending on the reflectivity of the surfaces [38,39].

2.5.3 Other tuning techniques

A variety of other tuning mechanisms which are available include dielectric mirrors, prisms, volume Bragg gratings (VBGs), distributed Bragg reflectors (DBRs), distributed feedback (DFB), and current or temperature tuning. The performance of each will influence its suitability for a given application.

Dielectric mirrors transmit wavelengths which are resonant within alternating dielectric layers of high and low refractive index. Tuning is achieved by mirror rotation, with filter bandwidths typically in the order of ~1 – 2 nm.

Prisms filter light by spatially separating their wavelengths into different angles due to the wavelength dependent refractive index of the material. However, the angular dispersion is typically not as great as can be achieved with diffraction gratings, and consequently diffraction gratings are commonly used over prisms for laser tuning.

A volume Bragg grating consists of photosensitive material with a periodic variation in the refractive index written into it. Filtering is achieved through diffraction of light that is resonant with the grating. Angle tuning offers a broad tuning range over 100's of nm, while large refractive index modulation over long interaction lengths allows high diffraction efficiencies and sub nanometre filter bandwidths.

Example DBR and DFB cavity configurations are shown in Figure 2.8(a) and (b) respectively. A DBR uses a periodic structure written into the waveguide of a semiconductor or fibre to act as a wavelength dependent mirror. In a DFB laser cavity, the grating and gain region overlap, and a phase shifting section(s) is added to promote lasing on a single longitudinal cavity mode. DBR and DFB devices can exist for fibres or semiconductors, and tuning is achieved by altering the grating and/or phase shift. With fibres, this is achieved by temperature or strain tuning the grating, while in semiconductors typically current tuning is used. Tuning ranges of DBR or DFB semiconductors and fibres is typically limited to <10 nm.

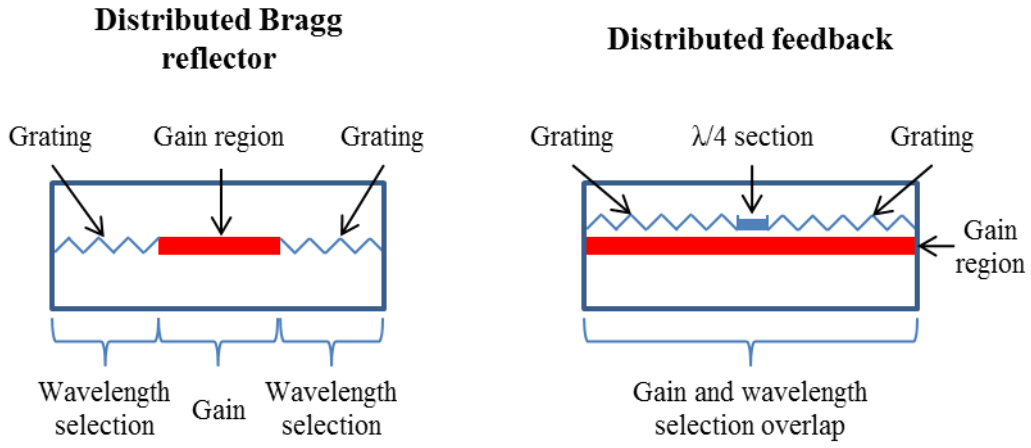

Figure 2.8 Layout of distributed Bragg reflector and distributed feedback.

2.5.4 Acousto-optic tunable filter

An acousto-optic tunable filter (AOTF) is an electronically controlled filter which utilises the acousto-optic effect to diffract light of a specific wavelength. A typical device layout is shown in Figure 2.9. A piezoelectric transducer is driven with an RF electrical signal at frequency *f*, generating an acoustic wave within the material which is able to diffract radiation within a narrow spectral range. Conservation of energy in the acousto-optic interaction requires the filtered light to be shifted in frequency by ±*f*. The

direction of the frequency shift is determined by the direction of the incident optical and acoustic wave vectors with respect to the crystal axes of the material.

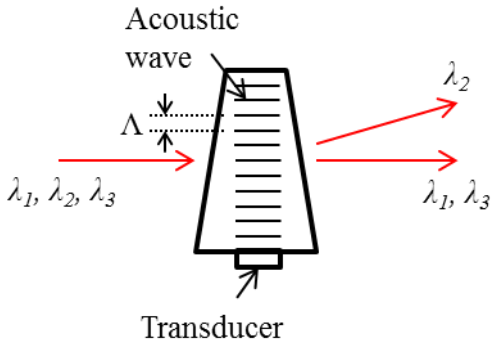

Figure 2.9 Acousto-optic tunable filter operation. Λ = wavelength of acoustic wave.

Selection of the filtered light is achieved by control of the transducer's RF drive frequency, which determines the phase matching condition for diffraction to occur. This tuning mechanism does not involve mechanical movement, with response times limited by the acoustic wave propagation time, which is typically in the order of 1 – 10's of μs, depending on the AOTF's configuration.

The exit facet of the AOTF is typically cut to provide dispersion compensation such that filtered light exits the AOTF at the same angle independent of wavelength. This is attractive for building tunable sources since feedback of the filtered light may be provided by a stationary mirror. Therefore, tunable cavities can be constructed which involve no mechanical movement.

Broad tuning is typically achieved over an octave in wavelength, allowing 100's of nm tuning range, and is limited by the transducer's impedance [40]. The ability to directly control the spectral content and power of the filtered light with high pointing stability by an electrical signal allows agile operation in which the filtered wavelength can be arbitrarily changed without mechanical movement or the need to sweep through intermediate wavelengths.

2.5.5 Mechanical actuation

Filtering techniques which rely on mechanical actuation typically use PZT transducers or micro electromechanical systems (MEMS) for translational motion, and

galvanometers or MEMS for rotational motion. All mechanical actuators will suffer from inertial effects, and fast tuning rates in the order of 10 – 100 kHz is only possible by exploiting mechanical resonance. However, this restricts the mechanical translation or rotation to sinusoidal motion, preventing agile tunability.

2.5.6 Comparison

A comparison of the tuning mechanisms discussed is shown in Table 2.1. Those relying on mechanical actuation can achieve fast tuning rates, however unavoidable inertial effects limit their agility, and arbitrary wavelength tuning is not possible.

Non-mechanical tuning with DBRs and DFB allows rapid inertia free tuning. However, the tuning range of these devices is typically limited to <10 nm.

Despite AOTFs typically having broader pass bandwidths than other filters, they are attractive filters since they are widely tunable over 100’s of nm, purely electronically controlled, and can be tuned to any arbitrary wavelength within an access time of 10’s of μs or less, enabling agile operation.

Table 2.1 Comparison between tuning methods.

Actuation	Spectral filter	Tuning rate	Tuning range (nm)	Resolution (nm)	Possible limitations
Mechanical	Diffraction grating	kHz level	>100	<1	Fast tuning relies on mechanical resonance, preventing agile tunability
	Fabry-Perot etalon	kHz level	>100	<1	
	Dielectric mirrors	kHz level	~10	~1 - 2	
	Prisms	kHz level	>100		
	Volume Bragg gratings	kHz	>100	~1	
Electronic	Distributed Bragg reflector	>1 MHz for diodes	~10	<1	Limited tuning range
	Distributed feedback	>1 MHz for diodes	~10	<1	Limited tuning range
	AOTF	10 - 100 kHz	>100	~1 - 10	Limited resolution

2.6 Gain media

The choice of suitable gain media for tunable sources will be influenced by the desired power levels, wavelength spans, and operating wavelength region. Here, several commonly used gain media are discussed and a comparison made between the characteristics of tunable sources built with them.

2.6.1 Transition metal doped crystals

Transition metals occupy the fourth row of the periodic table, and their electronic configuration is shown in Figure 2.10. In a crystalline structure with a host, the two 4*s* electrons and possibly one or more 3*d* electrons are used in forming the chemical bonds. The remaining 3*d* electrons which participate in lasing are then exposed to the electrostatic forces from other atoms in the crystal. The energies of the 3*d* electrons therefore strongly depend on the lattice structure and corresponding crystal field.

The strong interaction of the transition metal atom with the material lead to broad absorption and emission bands which are dependent on the host material [41]. Accessible wavelength ranges of a variety of transition metal based gain media are shown in Figure 2.11.

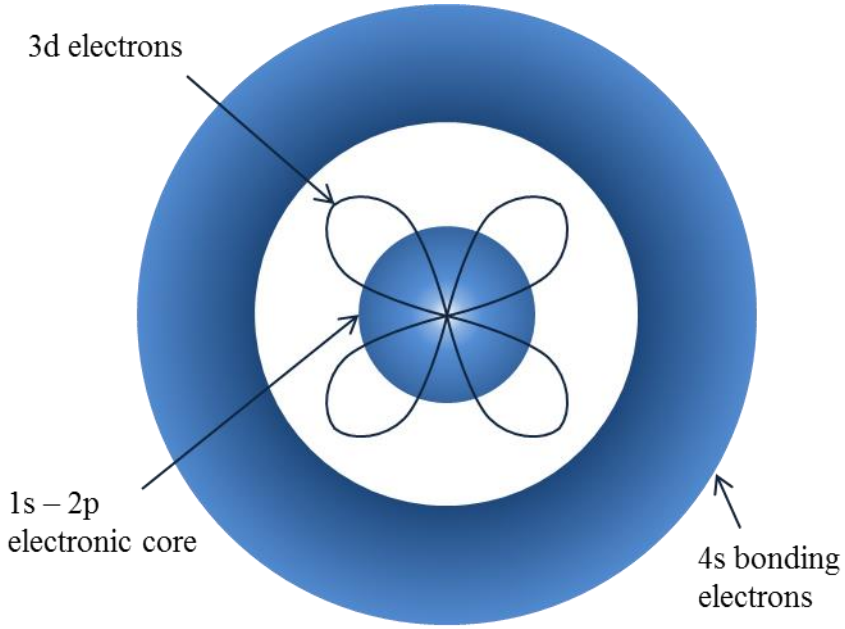

Figure 2.10 Transition metal electronic configuration [42].

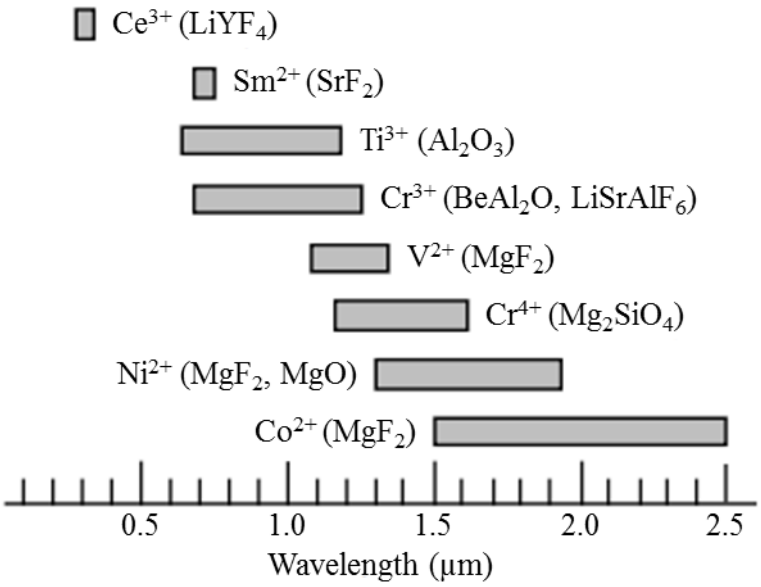

Figure 2.11 Reported wavelength ranges of transition metal crystalline lasers operating at room temperature [43].

The upper state lifetimes of transition metal gain media vary from microseconds to milliseconds. A summary of room temperature lifetimes of some commonly used transition metal gain media is shown in Table 2.2. Ti:Al_2O_3 exhibits one of the shortest lifetimes of these gain media at ~3.15 μs, while Ni:MgF_2 has a much longer ~3 ms lifetime.

Table 2.2 Summary of room temperature upper state lifetimes and emission bands of some commonly used crystalline gain media based on transition metals.

	Upper state lifetime	**Emission region**
Ti:Al_2O_3	~3.15 μs [44]	~0.6 – 1.2 μm
Co:MgF_2	~40 μs [42]	~1.5 – 2.5 μm
Ni:MgF_2	~3 ms [42]	~1.3 – 1.95 μm
Cr:$BeAl_2O_4$	~290 μs [45]	~0.6 – 1.25 μm

2.6.2 Rare-earth doped crystals

In rare-earths, the electrons in the 4*f* shell participate in lasing. The electrons in this shell are protected from the crystal fields by filled outer 5*s* and 5*p* shells. Consequently, the energy levels of rare earths are only weakly dependent on the host lattice, with changes in lasing wavelength due to different hosts occurring in the third or fourth significant figure [41].

The energy levels of rare-earth's in crystals are well-defined and narrow due to the active atoms existing in a well-defined environment [41]. This limits tuning over a continuous range to a few nm at most. Typical operating wavelengths of some commonly used rare earth ions are shown in Table 2.3. The upper state lifetimes of these rare-earth doped crystals can range from 100's of μs to 10's of ms.

Table 2.3 Operating wavelengths of various commonly used rare-earth ions.

Rare earth ion	**Operating λ (μm)**
Nd^{3+}	1.0, 1.3, 1.44, 1.83
Yb^{3+}	1.0
Er^{3+}	1.645, 2.7, 2.9
Tm^{3+}	1.9
Ho^{3+}	2.1

2.6.3 Rare-earth doped fibres

The emission wavelengths of rare-earth doped fibres differ greatly from the bulk crystals discussed in Section 2.6.2. The lack of crystalline structure in glass fibres results in site-to-site variation in the local field that shows up in a variation of the energy levels and various broadening processes, which results in a more or less continuous band of wavelengths that connect two manifolds [41]. The emission regions therefore become orders of magnitude greater than in crystals.

The accessible emission wavelengths of various rare-earth doped fibres are shown in Figure 2.12. Tuning over >100 nm is possible for Nd^{3+} and Yb^{3+} at ~1060 nm, for Er^{3+} at ~1550 nm, and for Tm^{3+} and Ho^{3+} around 1.9 – 2.1 µm. Similar to rare-earth doped crystals, the upper state lifetimes of rare-earth doped fibres are of the order of 0.1 – 10 ms.

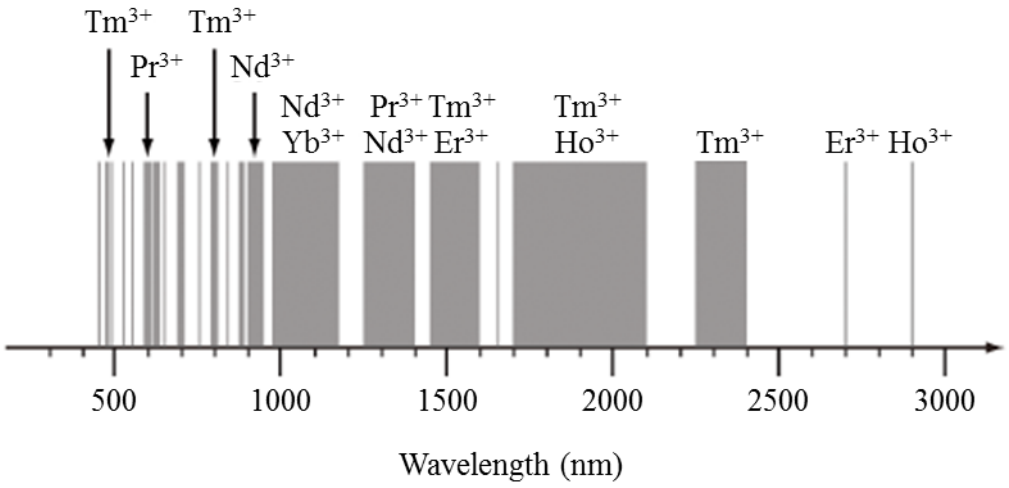

Figure 2.12 Emission wavelength of various rare-earth doped fibre [46].

2.6.4 Semiconductors

Semiconductor gain media are electrically pumped diodes which exhibit broad emission ranges and short upper state lifetimes. They consist of a p-n junction confined by a waveguide structure.

The operating principle is shown in Figure 2.13. Electrons in the valence band are excited to the conduction band when current is injected into the p-n junction, leaving a hole behind. The excited electrons move towards the bottom of the conduction band while the holes move towards the top of the valence band. From here the electron can recombine with the hole, emitting a photon. Stimulated emission can occur for an incoming photon of the correct transition energy.

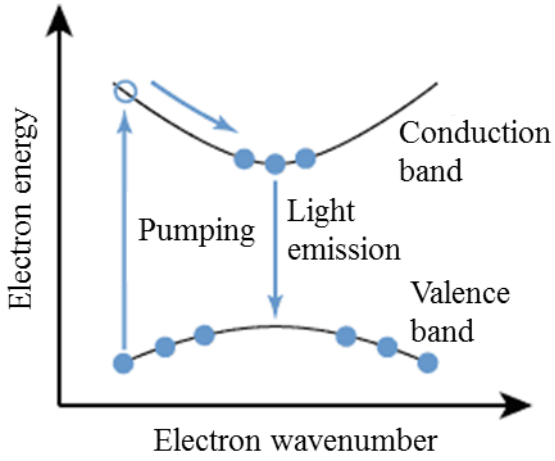

Figure 2.13 Mechanism for light generation in semiconductor optical gain media [47].

The broad range of conduction and valence band energies leads to broad emission wavelengths in the order of 10 – 100 nm for a single diode. Direct bandgap semiconductors are able to cover wavelengths from 0.4 – 2.2 µm as shown in Table 2.4. For wavelengths from 2.2 – 3.5 µm and >3.5 µm, indirect bandgap semiconductors or quantum cascade lasers (QCLs) are used, respectively. The rapid recombination rates results in upper state lifetimes in the order of nanoseconds [48].

Table 2.4 Wavelength ranges covered by various semiconductor devices [49,50].

Semiconductor type	**Spectral range (nm)**
II-VI and III-V	400 – 600
AlGaInP/GaAs	610 – 690
AlGaAs/GaAs	780 – 880
InGaAs/GaAs	880 – 1100
InGaAsP/InP	1100 –1600
InGaAs/InP	1500 – 2100
InGaAsSb/AlGaAsSb	2000 – 2600

2.6.5 Comparison

A comparison between power levels, wavelength spans, operating wavelength regions, and upper state lifetimes of the gain media discussed is shown in Table 2.5. Lasers tunable over >10 nm can be constructed with transition metal doped crystals, rare-earth fibres, and semiconductors. However, the spectral coverage available for transition metal doped crystals and rare-earth doped fibres is limited to certain wavelength regions, while semiconductors can access any wavelength >0.4 µm. For this reason, the focus of this thesis is on the performance and limitations of AOTF tuned semiconductors.

Table 2.5 Comparison of typical spectral coverage and upper state lifetimes between gain media. QCL = quantum cascade laser.

Gain media		**Power**	**λ span**	**Operating λ (µm)**		**Lifetimes**
Crystal	Rare-earth doped	<10 W	<10 nm	1.0, 1.3, 1.5, 1.9, 2.1		0.1 – 10 ms
	Transition metal doped		<100 nm	0.7 – 1.0		1 µs – 1 ms
Fibre		<100 W	~100 nm	1 – 1.2, 1.53 – 1.6, 1.65 – 2.2, 2.7 – 3.2		0.1 – 10 ms
Semiconductor		<0.1 W	~100 nm	Direct bandgap	0.4 – 2.2	1 – 10 ns
				Indirect bandgap	>2.5	
				QCL	>3.5	

2.7 Summary

In this chapter, the operating principles of tunable lasers were presented. The core components required to build a tunable source is the gain medium, tunable filter, and cavity. The source operates on one or more longitudinal modes of the cavity, depending on the strength of the filter.

Ideally, the operating wavelengths are determined by the filter alone. However, if the filter is too weak then intra-cavity etalons effects can influence the operating longitudinal modes.

For a frequency shifting filter, the condition for forming longitudinal modes is no longer valid since the frequency shift per round trip prevents interference from building up.

Several tuning mechanisms were compared, and the advantages of AOTF's over other conventional techniques identified. It provides agile electronic control of the power and wavelength of the filtered light.

Different gain media were presented, with semiconductors suitable for testing the performance and limitations of AOTF tuned sources owing to their broad tuning ranges, and availability across all wavelengths >0.4 μm.

Chapter 3
Diffraction grating tuned lasers

3.1 Introduction

Diffraction grating tuning of laser cavities is a common technique for producing a spectrally controlled output. Such sources are used for spectroscopy [51–55], metrology [56], injection seeding of optical parametric oscillators [57], testing of optical components [58], and optical loss measurements.

The aim of this chapter is to describe two diffraction-grating tuned sources with aim of understanding some of the instrumentation, techniques and critical measurements required to characterise wavelength tuneable sources.

The first laser will involve a well understood fibre gain medium and the second laser will also be used to characterise the semiconductor gain medium that will be employed in subsequent chapters.

3.2 Grating-tuned thulium-doped fibre laser

The sensitivity of advanced gravitational wave detectors is currently limited by thermal noise and absorption induced wavefront distortion. Thus, future upgrades may use

cryogenic silicon test mass mirrors [59]. However, silicon is strongly absorbing at the current 1064 nm detector wavelength. This promotes a change in wavelength to 1550 – 2100 nm. The University of Adelaide node of OzGrav is investigating optical absorption in low OH bulk fused silica in the 1.9 – 2.1 μm wavelength region. To perform these measurements, OzGrav required a laser source with power levels in the order of 1 – 10 Watts tunable over this spectral region. Tunable lasers based on semiconductor gain media are available around 2 μm wavelengths [60–62], however they operate at milliwatt power levels. The power requirements and tunability at these wavelengths are easily met with thulium-doped fibre [63,64].

3.2.1 Fibre background theory

Fibre gain media are based on a glass core doped with active rare-earth ions. When pumping the rare-earth ions with light of the correct wavelength electrons are promoted to a metastable state. This allows for stimulated emission to occur at a signal wavelength. Pumping geometries can be separated into core and cladding pumping. One of the advantages of fibres over traditional free-space optical cavities is that the beam quality is largely determined by the fibre waveguide geometry rather than alignment of optical components.

3.2.1.1 Core pumping geometry

In a core pumped geometry both the signal and pump light are confined to the core of the fibre. This results in a large overlap between the pump mode and the active ions, allowing for high absorption per length of fibre. However, a high brightness pump is required to efficiently couple to the core.

3.2.1.2 Cladding pumping geometry

In cladding pumping, a double clad fibre is used which consists of core, inner cladding, and outer cladding layers. Pump light is confined to the inner cladding. This allows the use of high power, low brightness pump sources such as laser diodes. To prevent cladding light propagating as helical modes, which do not interact with the core, various shaped claddings are used to break the circular symmetry, as detailed in Figure 3.1.

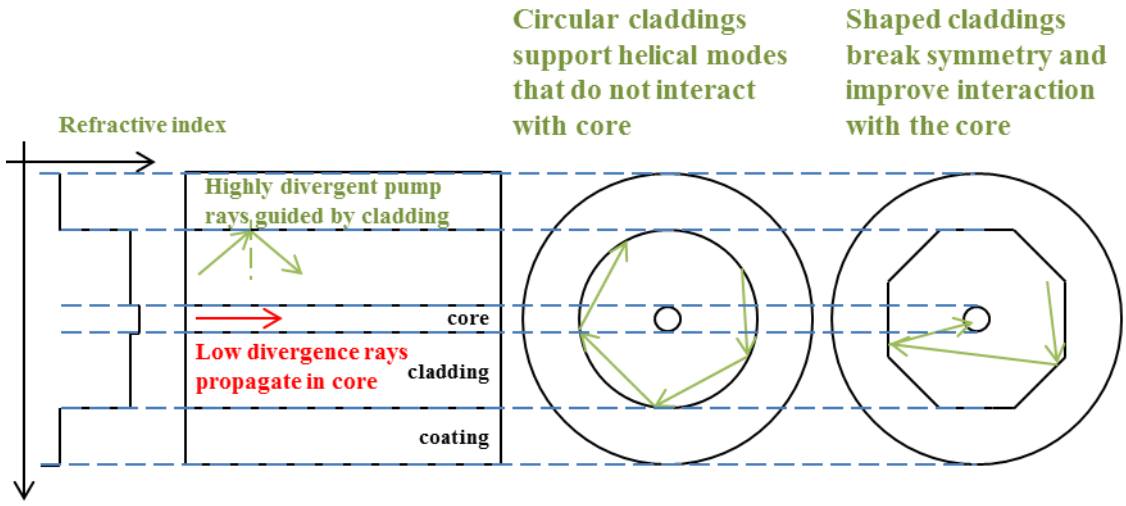

Figure 3.1 Refractive index profiles across core, cladding, and coating regions of double-clad fibres [35]. Also shown are the cross-sections and an illustration of the impact of shaped claddings on the disruption of helical modes in active fibres.

3.2.1.3 Pumping and lasing levels of thulium-doped silica

The energy levels and pumping schemes for thulium ions in a silica host is shown in Figure 3.2. One pumping method is to resonantly pump at 1580 nm into the $^3F_4$ manifold. Another more electrically efficient technique is to pump at 790 nm and utilise cross relaxation. Here, electrons are excited into the $^3H_4$ manifold. The excited ion can then transfer some of its energy to an adjacent ion in the lower $^3H_6$ manifold such that they both end up in the $^3F_4$ lasing manifold. This process is referred to as cross-relaxation and allows a quantum efficiency >1.

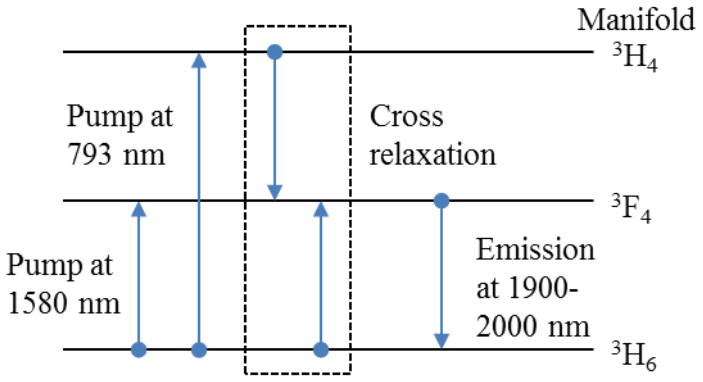

Figure 3.2 Energy levels for the pumping and emission of thulium ions in a silica host [35].

The absorption profile of thulium doped fibre around 790 nm is shown in Figure 3.3.

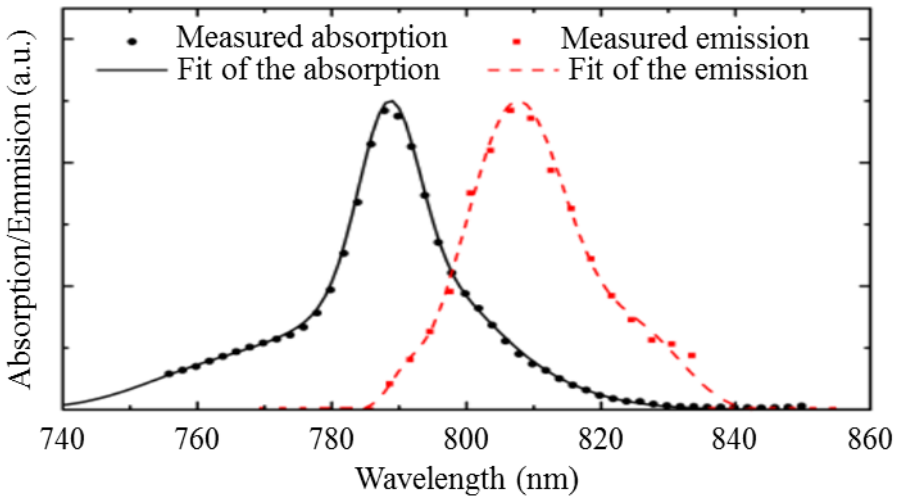

Figure 3.3 Absorption and emission spectra of thulium doped fibre from 740 – 860 nm [65].

The preferred emission wavelength of thulium-doped silica is strongly dependent on the inversion level, as demonstrated in Figure 3.4, where the effective cross-section is shown from 1.5 – 2.2 µm at various inversion levels.

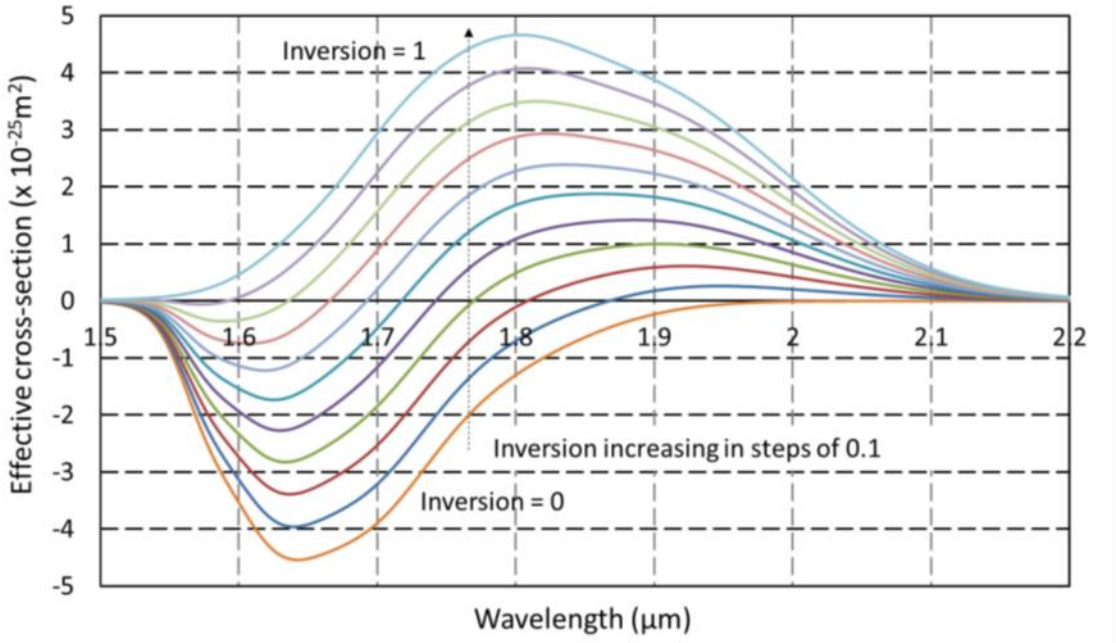

Figure 3.4 Effective cross-section of thulium ions as a function of wavelength at various inversion levels [35].

3.2.2 Laser design

The laser design is outlined in Figure 3.5. A 5.5 m, double clad thulium-doped fibre is used as the gain medium (iXblue photonics, IXF-2CF-Tm-O-6-130). The core has a 6 µm diameter and 0.22 numerical aperture (NA). The cladding is octagonal with a 125 µm flat-to-flat and an NA ≥0.46. This fibre is spliced to a 2+1→1 combiner (ITF) with matched cladding diameter and 10 µm core diameter. The pump fibres have a 105 µm core with 0.22 NA and a 125 µm diameter cladding. One of the pump fibres is spliced to a 793 nm fibre coupled laser diode (LIMO, 35-F100-DL790-EX1677). The diffraction grating at one end of the laser cavity acts as the tuning element while feedback at the other end is provided by the 4% Fresnel reflection from a flat cleave made in the active fibre. The estimated unabsorbed pump power at 793 nm is 10.5 dB below the launched power.

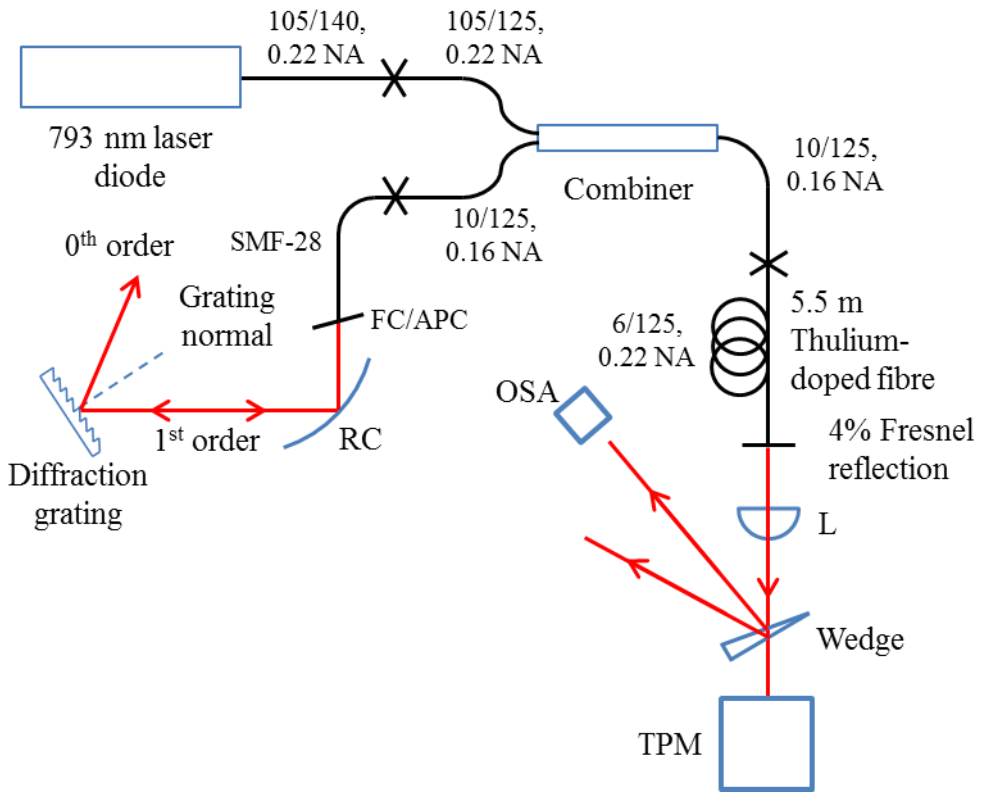

Figure 3.5 Cavity design for thulium-doped fibre laser. RC = reflective collimator, L = 11 mm uncoated aspheric lens, TPM = thermal power meter.

For characterisation of the laser, the output is collimated onto a thermal power meter (TPM, Thorlabs, S302C) using an 11 mm uncoated aspheric lens. A wedge is used to

pick off a portion of the beam for spectral measurement with an optical spectrum analyser (OSA, Yokagawa, AQ6375). Output power is reported without compensating for losses from the wedge.

3.2.3 Power and wavelength characterisation

The spectrum and power of the laser at various wavelengths is shown in Figure 3.6. The laser was tuned from 1920 – 2060 nm with 1.69 W peak power at 1980 nm. Less than 25% drop in power occurred over the entire tuning range. Parasitic lasing was observed when operating at wavelengths below 1920 nm and beyond 2060 nm.

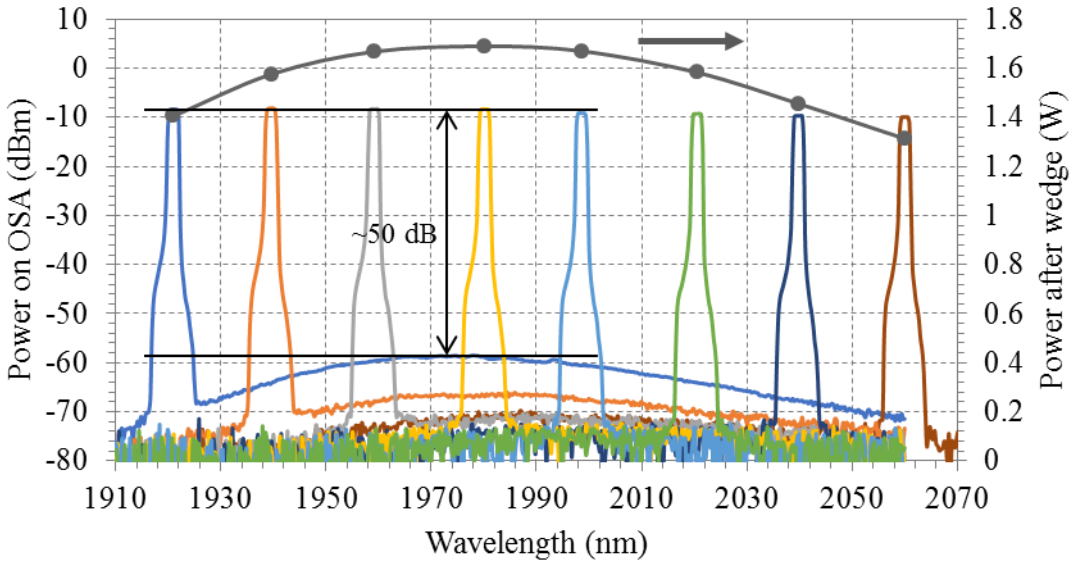

Figure 3.6 Output spectrum and power of the thulium-doped fibre laser at various operating wavelengths measured with the OSA and thermal power meter, respectively. An OSA resolution setting of 2 nm was used.

Finer resolution spectra of the laser at 1921.0 nm and 1980.1 nm are shown in Figure 3.7. The laser exhibited side-lobes and operated with linewidths <0.6 nm across the entire tuning range.

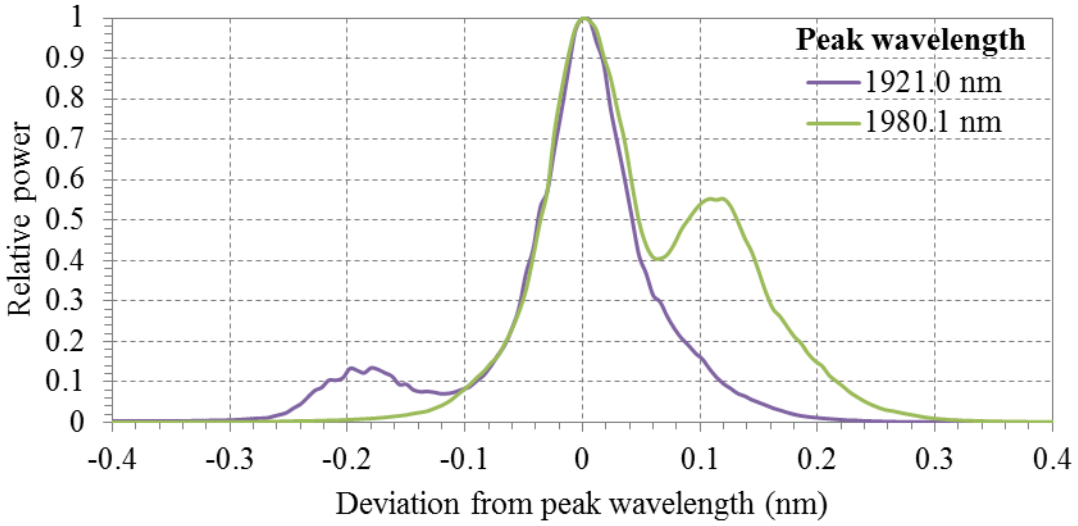

Figure 3.7 Finer resolution output spectra of thulium-doped fibre laser at 1921.0 nm and 1980.1 nm. Power is plotted relative to the peak power. An OSA resolution setting of 0.05 nm was used.

The laser slope efficiency when operating at 1980 nm is shown in Figure 3.8. Here, the efficiency was measured by the ratio of laser output power after the wedge to the 793 nm optical pump power exiting the LIMO diode. A ~24% slope efficiency was obtained with a 1.9 W pump threshold. The output power was increased up to 1.7 W with no roll over observed.

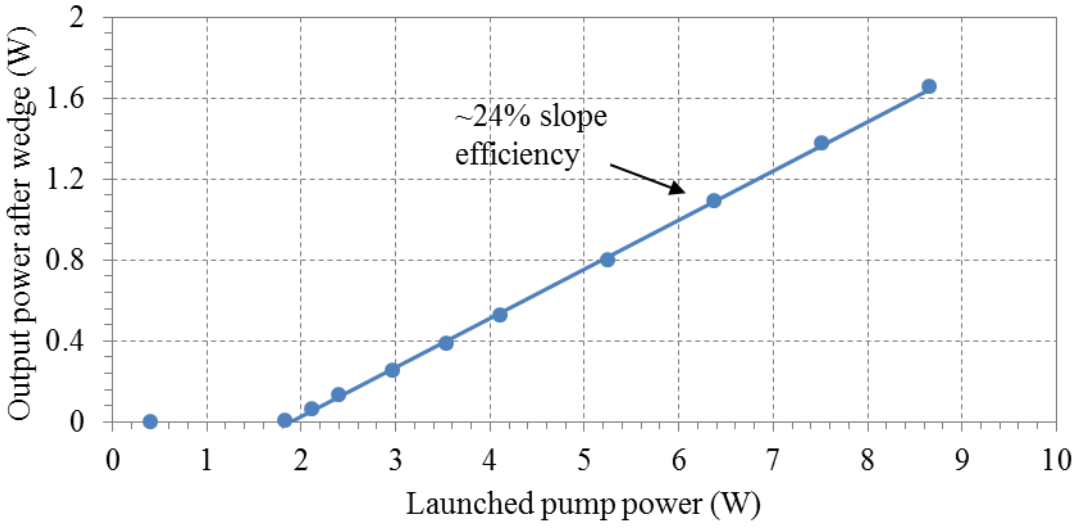

Figure 3.8 Thulium-doped fibre laser output power after wedge vs launched optical pump power.

3.2.4 Discussion

The slope efficiency of the laser built in this section was not as high as previous diffraction grating or VBG tuned thulium-doped fibre lasers [63,64]. This is attributed to the mismatch of core diameters at the active fibre splice join, and free space coupling losses. The source had a 1.69 W peak at 1980 nm and less than 25% drop in power across 1920 – 2060 nm wavelength range. Tuning beyond this wavelength region resulted in parasitic lasing. The linewidth and OSNR over the tuning range was <1 nm and ≥50 dB, respectively. At the poorest OSNR wavelength of 1920 nm, the ratio of ASE to lasing power is <0.001%, and so the ASE will have negligible effect on the required absorption measurements with the source. The laser meets the requirements as set out by OzGrav and is currently being used to take measurements.

3.3 Grating tuned superluminescent diode laser

Semiconductor gain media are attractive for building AOTF tuned lasers due to their broad spectral bandwidth. The tunability of semiconductor gain media was thus investigated using a diffraction grating.

Superluminescent diodes (SLED's) are broad-bandwidth semiconductor emitters usually configured with an anti-reflective (AR) and highly reflective (HR) facet. A wide variety of direct bandgap semiconductor materials can be produced by combining different group III-V ions, allowing access to wavelengths from 400 – 2200 nm [49]. To access the 1600 – 1800 nm region of interest here we selected an SLED that uses an InP active layer (Thorlabs, SAF1091H). The layout of this chip is shown in Figure 3.9. It contains a curved waveguide which makes a 26.5° angle to the normal of the AR coated facet, which has a coupling reflectivity back into the waveguide of $R_C < 0.01\%$, and is normal to an $R_{HR} = 90\%$ higher reflectivity (HR) facet. The 26.5° angle acts to reduce the effect of back reflections from the AR facet as most reflected light is not coupled to the waveguide and lost, L_C. The length and refractive index of the waveguide are $L = 1.5$ mm and $n_g = 3.2$, respectively [66]. R_C is comprised of both the reflectance of the AR coating, and the efficiency of the reflection coupling back into the waveguide from the angled-cleaved facet at the output of the gain chip.

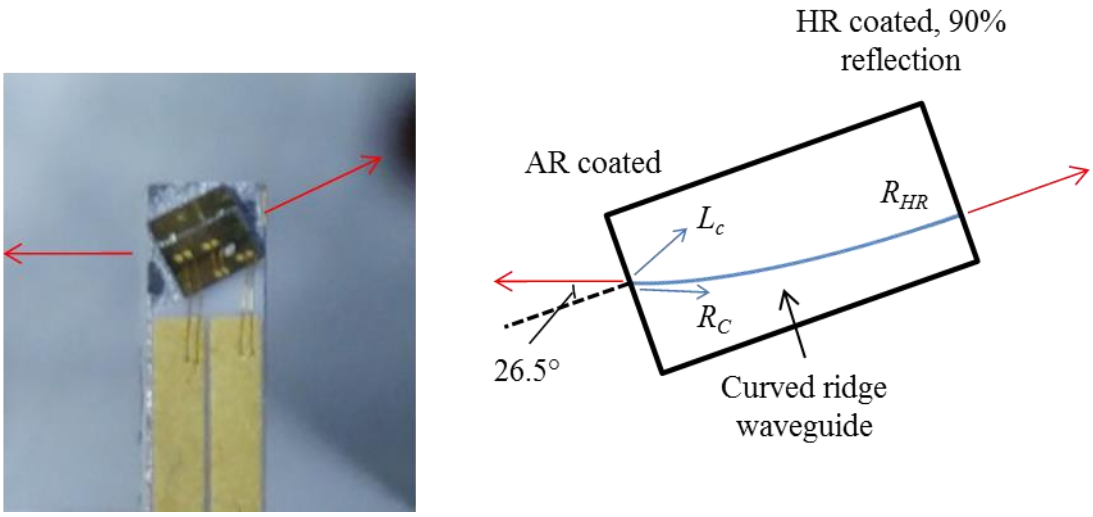

Figure 3.9 SLED chip used for building a tunable external cavity laser diode, along with its layout. R_{HR}, R_C, and L_C represent the reflectance of the HR facet, the effective reflectance of the AR facet, and the scatter losses at the AR facet, respectively.

3.3.1 Characterisation of SLED

The SLED is characterised using the setup in Figure 3.10. It was mounted on an aluminium heatsink with no active temperature control and driven at 500 mA by a diode driver (Thorlabs, LDC 240C) in constant current mode. The 3.1 mm and 8.0 mm focal length, AR coated lenses collimated the output from the AR and HR face, respectively.

For spectral measurements, optical spectrum analyser (OSA, Yokagawa AQ6375) was used. A calibrated InGaAs photodiode power meter (PPM, Thorlabs, S155C) was used to measure power exiting the AR and HR facets, (P_{AR} and P_{HR}). Beam profile measurements were made using a 40 µm pixel pitch InGaAs charge-coupled device camera (Goodrich, SU320M-1.7RT).

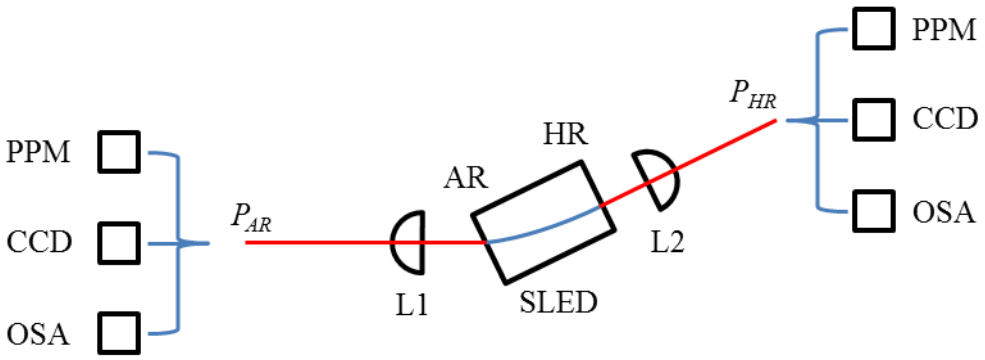

Figure 3.10 Collimation of SLED outputs from facets AR and HR for power, spectral, and beam shape measurements. AR = anti-reflective facet, HR = 90% reflective facet, L1 = 3.1 mm focal length AR-coated aspheric lens, L2 = 8.0 mm focal length AR-coated aspheric lens, PPM = photodiode power meter, CCD = InGaAs charge-coupled device camera, OSA = optical spectrum analyser.

3.3.1.1 Optical spectrum

The amplified spontaneous emission (ASE) spectrum exiting the AR facet is shown in Figure 3.11. It exhibits a broad wavelength span with a 3 dB bandwidth spanning ~140 nm from ~1610 – 1750 nm.

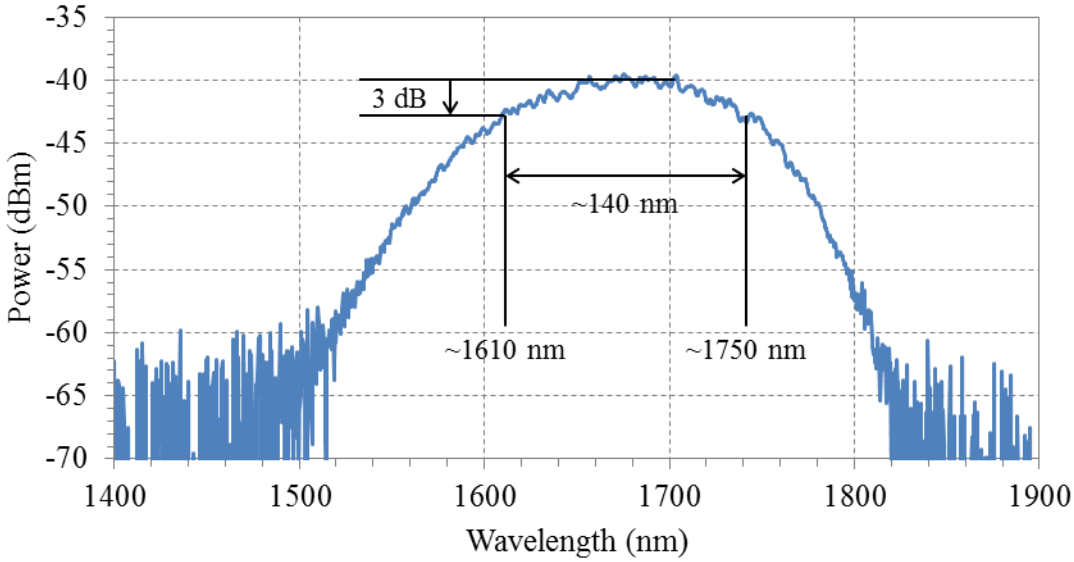

Figure 3.11 SLED ASE spectrum from AR facet measured using a multimode fibre coupled to an OSA. An OSA resolution setting of 2 nm was used.

A finer resolution spectral measurement of the ASE output from the AR facet over 4 nm is shown in Figure 3.12. A ~1.8 dB peak-to-peak sinusoidal modulation in the spectral power is observed with a ~0.3 nm period. This agrees with the 2 dB maximum peak-to-peak ripple specifications for the SLED.

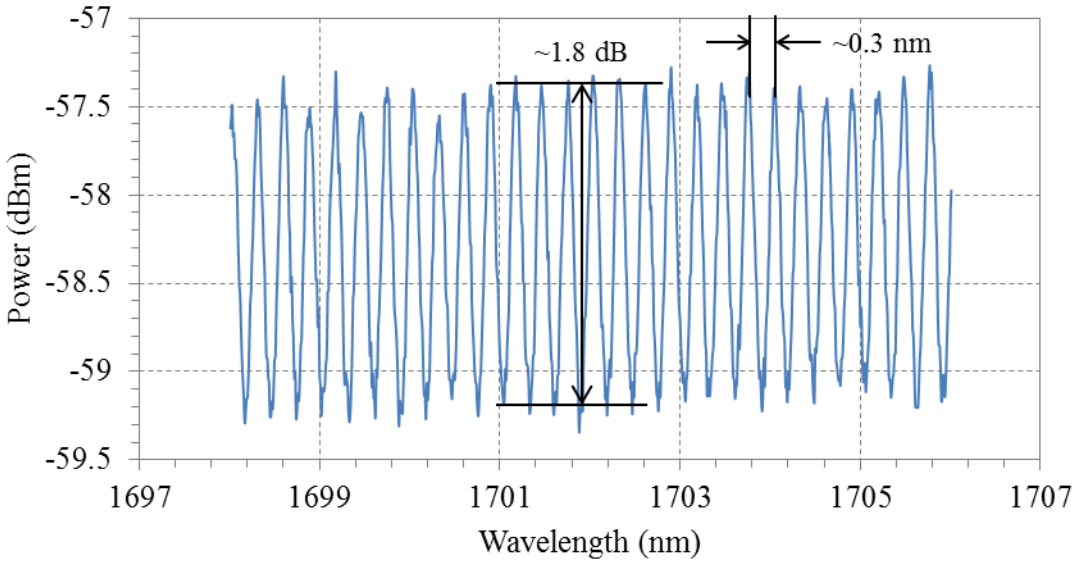

Figure 3.12 Output spectrum from AR facet of the Thorlabs SLED. An OSA resolution setting of 0.05 nm was used.

The peak-to-peak modulation at multiple injection currents is shown in Figure 3.13. Also shown is the modulation depth *M*, defined as

$$M = \frac{I_{min}}{I_{max}}, \qquad \textbf{3.1}$$

where I_{min} and I_{max} are the minimum and maximum intensities. As the current decreases from 500 mA to 200 mA, the peak-to-peak modulation reduces from ~1.8 to ~1.0 dB.

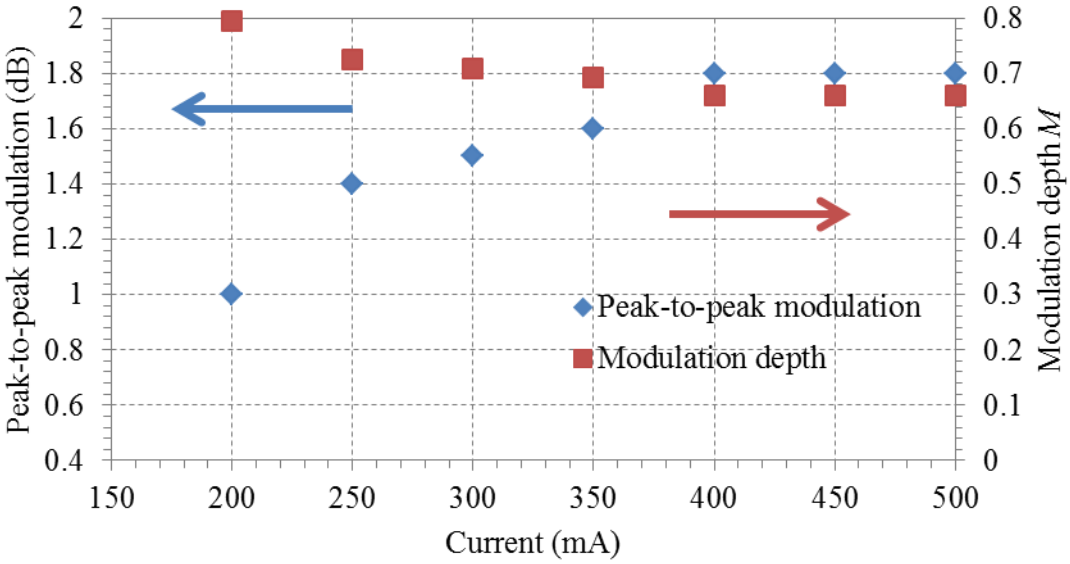

Figure 3.13 Peak-to-peak modulation and modulation depth *M* of the output spectrum at multiple injection currents.

3.3.1.2 Output powers

The powers P_{AR} and P_{HR}, at various injection currents are shown in Figure 3.14, and their ratio is shown in Figure 3.15. At 500 mA, the output powers are P_{AR} = 2.2 mW and P_{HR} = 4.2 µW, giving a ratio of P_{AR}/P_{HR} ~ 520.

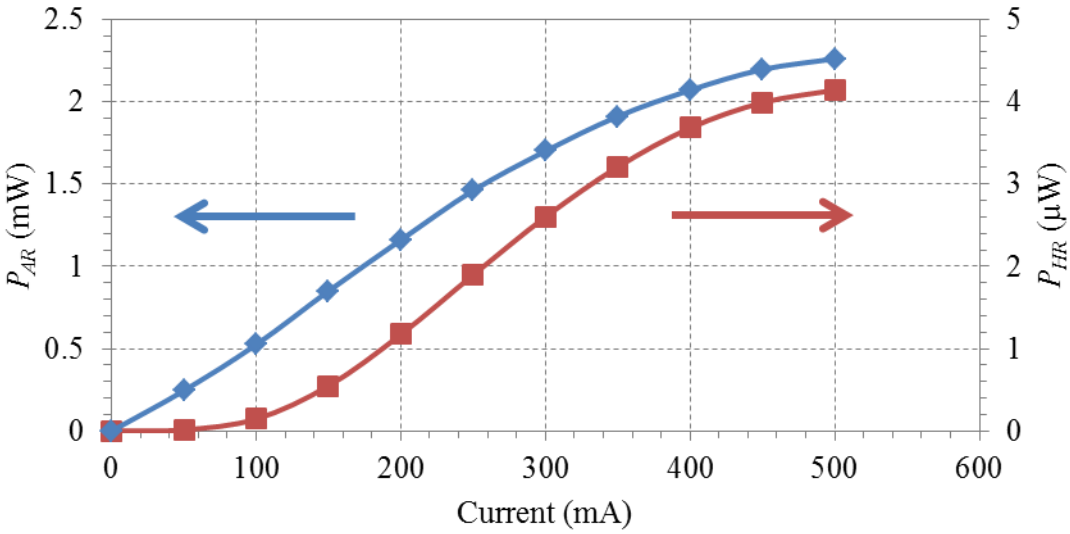

Figure 3.14 Measured output powers P_{AR} and P_{HR} from the SLED as a function of injection current.

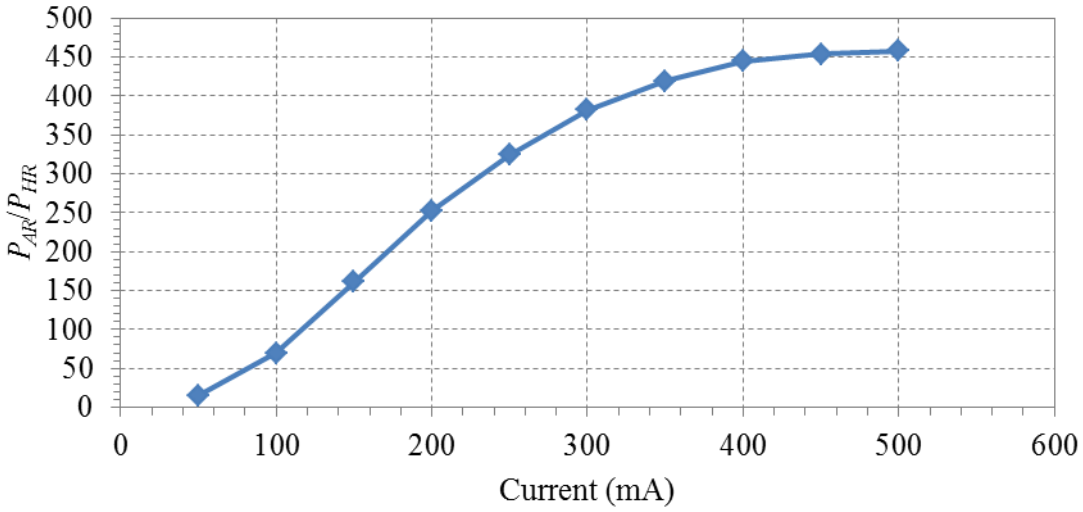

Figure 3.15 Ratio of powers P_{AR} and P_{HR} from the SLED as a function of injection current.

3.3.1.3 Beam profile

The profile of the collimated beam from the AR facet and the best-fit Gaussian are shown in Figure 3.16. The second moment ($D_{4\sigma}$) beam diameter in the *x* and *y* axes are ~1 mm and 0.7 mm, respectively.

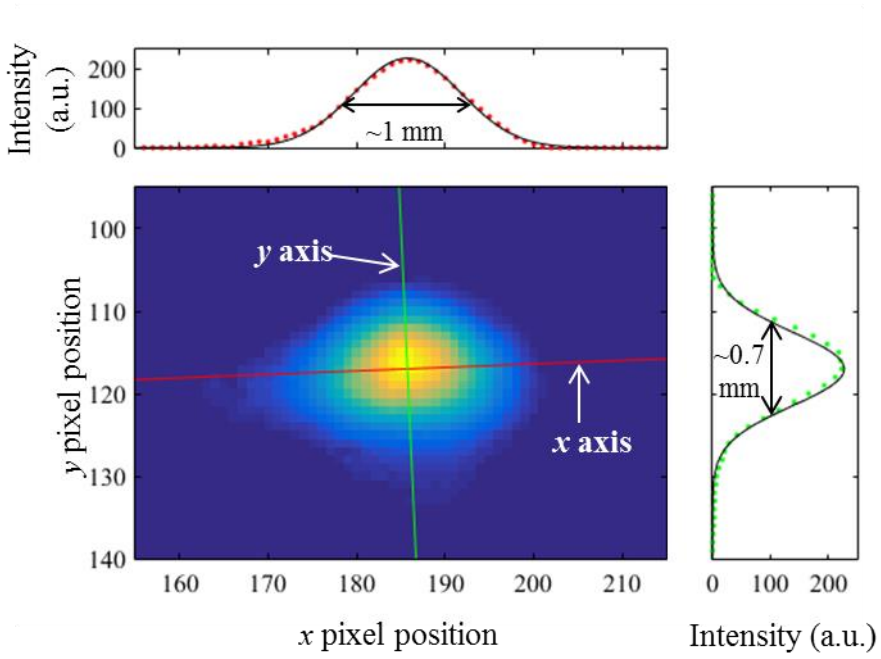

Figure 3.16 Beam profile measurement of collimated SLED output from AR facet in Figure 3.10. Also included is a best-fit Gaussian for the indicated axes.

3.3.1.4 Discussion

The 140 nm, 3 dB bandwidth of the SLED output highlights the broad emission spectrum achievable by semiconductor gain media. Using the $n_g = 3.2$ waveguide refractive index and $L = 1.5$ mm chip length, a 31.2 GHz free spectral range (FSR) can be calculated for the SLED using Equation 2.1. The 0.3 nm spacing of the spectral ripple in Figure 3.12 corresponds to a 31.6 GHz FSR using Equation 2.2, which agrees with the 31.2 GHz FSR calculated for the SLED. The spectral modulation observed in the output of the AR facet can therefore be attributed to the reflected light from this facet that couples into the waveguide, leading to an etalon effect between the two facets.

The AR facet coupling reflectivity R_C of the SLED can be estimated from the expression for the modulation depth, M in the ASE spectrum [67]:

$$M = \frac{1 - G_s\sqrt{R_C R_{HR}}}{1 + G_s\sqrt{R_C R_{HR}}}. \qquad \textbf{3.2}$$

Here, G_s is the single pass gain, R_C is the effective AR facet reflectivity, and R_{HR} is the reflectance of the HR facet. Measured values for M at various injection currents were given in Figure 3.13. The reflectance off the HR facet R_{HR} is assumed to be 90% as reported in the SLED's specifications [66].

The single pass gain G_S can be expressed in terms of P_{AR}, P_{HR}, R_C, and L_C by considering the passage of light from the HR facet to the output of the AR facet in Figure 3.17.

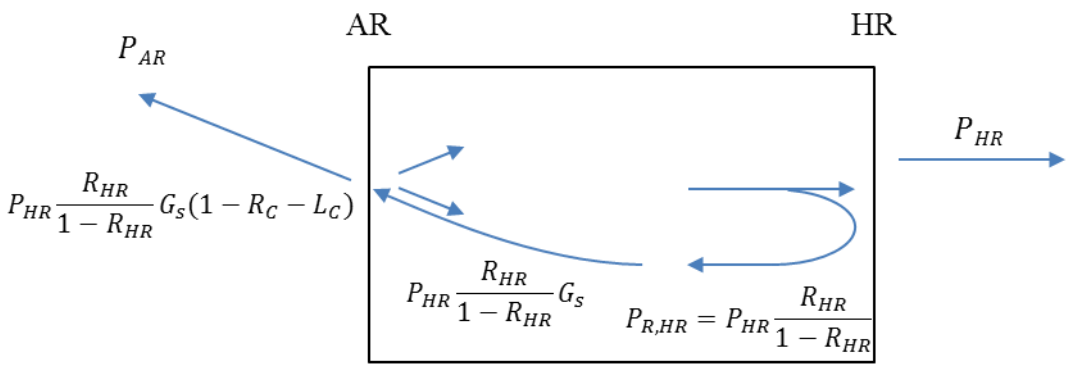

Figure 3.17 Diagram showing power levels at varying points both within and external to the SLED. AR = anti-reflection coated facet, HR = high reflection coated facet, P_{HR} = power exiting HR facet, R_{HR} = HR reflectance, $P_{R,HR}$ = power reflected off HR facet, G_S = single pass SLED gain, R_C = effective AR facet reflectance, L_C = scatter losses at the AR facet.

The amount of light that is reflected off the HR facet, $P_{R,HR}$ can be written as

$$P_{R,HR} = P_{HR}\frac{R_{HR}}{1-R_{HR}} \quad \textbf{3.3}$$

This light will increase by G_S on a single pass of the chip before reaching the AR facet. The transmitted output P_{AR} is then

$$P_{AR} = P_{HR}\frac{R_{HR}}{1-R_{HR}}G_s(1-R_C-R_L), \quad \textbf{3.4}$$

and the single pass gain G_S is thus estimated using

$$G_s = \frac{P_{AR}}{P_{HR}}\frac{1-R_{HR}}{R_{HR}(1-R_C-R_{loss})}. \quad \textbf{3.5}$$

Inserting Equation 3.5 into Equation 3.2 allows the coupling reflectivity R_C to be calculated at various injection currents using measured values of M and P_{AR}/P_{HR}. The scatter loss L_C is expected to be a few percent, and so does not significantly affect the calculations. It is therefore set to zero.

The estimated R_C values are shown in Figure 3.18. The results indicate an effective AR facet reflectivity of ~4×10^{-6} – 6×10^{-6} (0.0004 – 0.0006%).

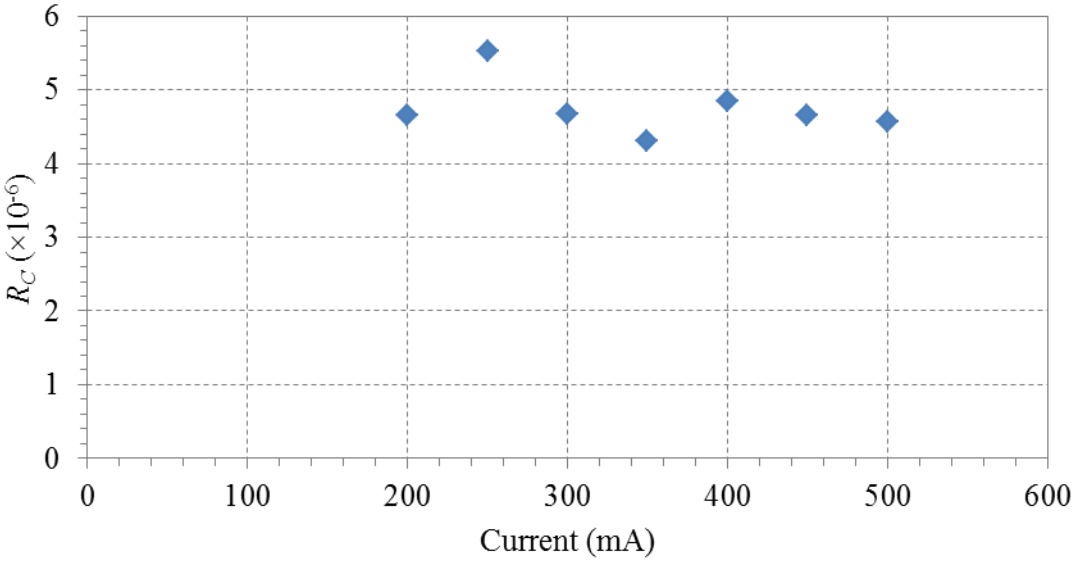

Figure 3.18 Estimated values for the effective AR reflectance R_C of the SLED at multiple injection currents.

The measured beam profile for the SLED corresponds well with its single transverse polarisation. This indicates the beam quality of a laser built with this gain medium might be high, with aberrations determined primarily by the optical elements within the cavity.

3.3.2 Grating tuned SLED laser

3.3.2.1 Laser design

The SLED gain medium was incorporated within a Littrow-configuration external-cavity laser resonator as shown in Figure 3.19. It follows the Thorlabs example configuration for SLEDs [68], and is similar to previous grating tuned lasers [69–71]. Light exiting the SLED's AR facet was collimated with a 3.1 mm focal length, AR-coated aspheric lens. A plane ruled reflective diffraction grating (Richardson Gratings, 53-*-775R) with 360 lines/mm was placed in Littrow configuration. The wavelength was controlled by diffraction grating rotation.

A 50% reflective output coupler (Thorlabs, BSW28) was placed between the lens and grating to outcouple the laser light so that it was insensitive to grating rotation. Two beams were reflected by the output coupler. One comes directly from the SLED while

the other was filtered by the grating. The output was taken from the filtered beam because of its improved optical signal to noise ratio (OSNR).

Diagnostic tools used for characterising the laser power and spectra were a photodiode power meter (Thorlabs, S155C) and an OSA (Yokagawa, AQ6375), respectively.

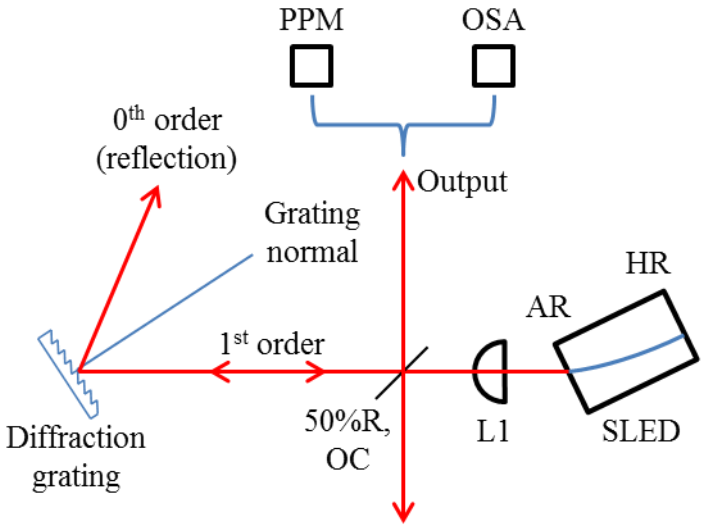

Figure 3.19 Cavity design for the grating-tuned semiconductor laser. OC = 50% reflective output coupler. AR = anti-reflective facet, HR = 90% reflective facet, L1 = 3.1 mm focal length, AR-coated aspheric lens, PPM = photodiode power meter, OSA = optical spectrum analyser.

3.3.2.2 Laser results

The output spectrum of the laser at various operating wavelengths is shown in Figure 3.20. The 3 dB tuning range was ~140 nm from 1610 – 1750 nm. The measured power levels over this range were in the order of ~5 – 10 mW.

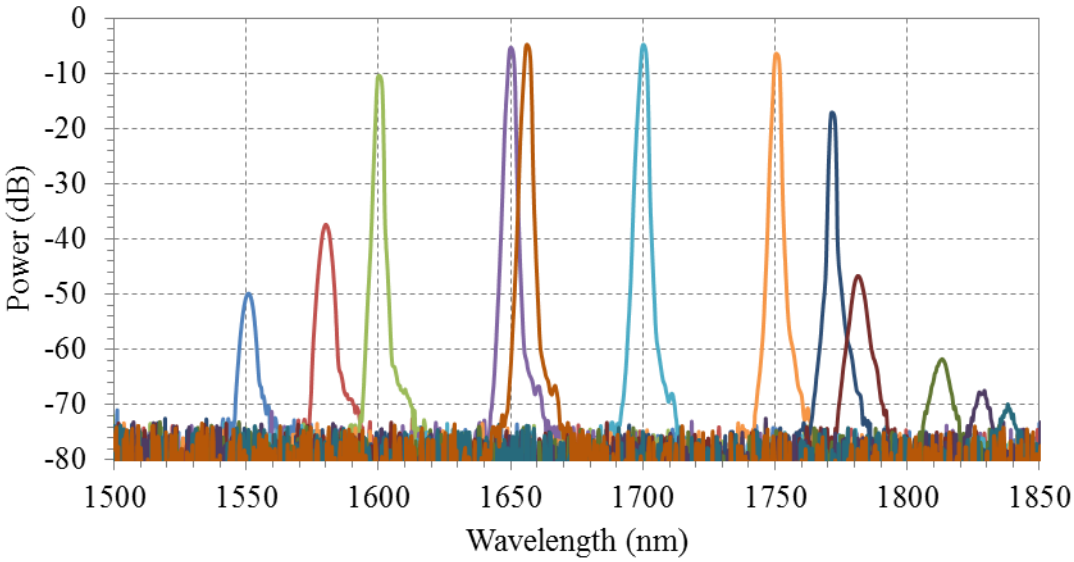

Figure 3.20 Output spectra of grating tuned semiconductor laser at various operating wavelengths. An OSA resolution setting of 2 nm was used.

A finer resolution spectral measurement of the laser tuned to around 1700 nm is shown in Figure 3.21. Side-lobes are present with a 0.3 nm separation between peaks, as expected from the ASE spectrum in Figure 3.12.

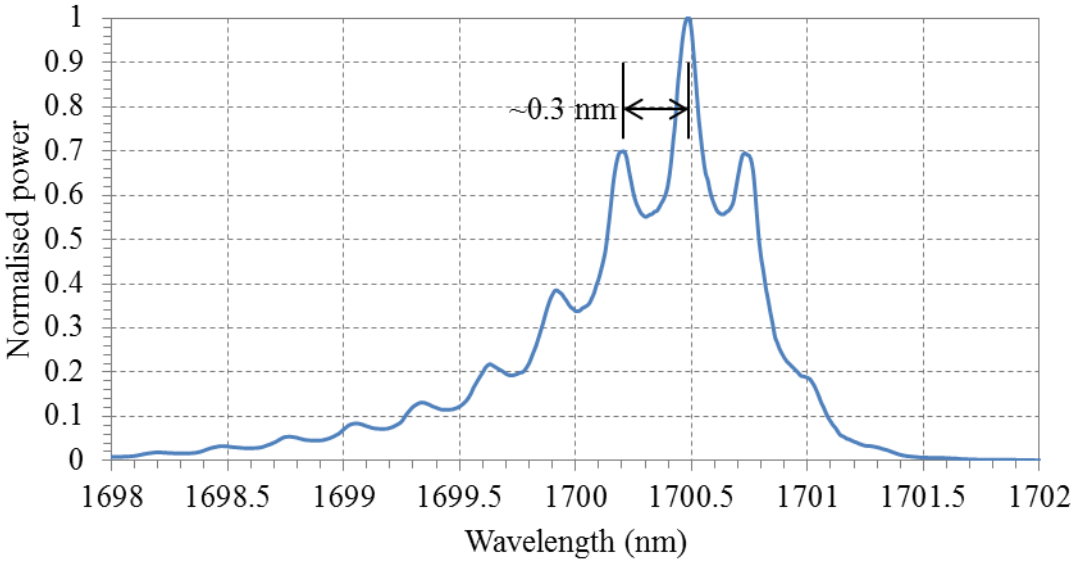

Figure 3.21 Normalised spectrum of laser around 1700.5 nm, illustrating the etalon effects present in the laser. An OSA resolution setting of 0.05 nm was used.

3.3.2.3 Discussion

The 0.3 nm sideband separation in the spectrum of the laser corresponds well with the 0.3 nm spacing of the spectral ripple observed in the SLED, which was attributed to etalon effects originating from reflections off the AR facet of the SLED. Improvements can be made to the cavity design to reduce the etalon effect by improving the spectral resolving power from the grating. This could be done by switching to a grating with more lines/mm [72], or expanding the beam incident on the grating thereby increasing the number of ruled lines interacting with the beam [73]. Alternatively, a Littman-Metcalf grating configuration could be used to double pass the grating [74].

3.4 Summary

In this chapter, two diffraction grating tuned sources were built based on rare-earth doped fibre and semiconductor gain media. The tunable fibre source utilised thulium-doped fibre to access the 1.9 – 2.1 µm region required for OzGrav to characterise SiOH and IR absorption in bulk fused silica. The source was tuned across 1920 – 2060 nm with powers ≥1.3 W.

The semiconductor laser utilised an SLED chip in a standing wave cavity. The SLED was first characterised and had a broad ASE emission with a 140 nm, 3 dB bandwidth from 1610 – 1750 nm. A ~1.5 dB spectral modulation was measured and attributed to unwanted reflections off its AR facet. Placing a diffraction grating in Littrow configuration resulted in a tunable source from 1650 – 1750 nm, with power levels in the 5 – 10 mW range. While etalon effects were observed in the laser it is still capable of characterising AOTFs. The knowledge of the SLED gain medium will be useful in following chapters when tunable sources based on AOTFs are built.

The fibre source built in this chapter supports other research activities within OzGrav, while the semiconductor source is critical for subsequent characterisation of AOTFs.

Chapter 4
Acousto-optic tunable filter operation and characterisation

4.1 Introduction

Acousto-optic tunable filters (AOTFs) are optical filters that do not rely on mechanical actuation of components. Consequently, these devices offer inertia free control of the transmission wavelength. Their agile ability to filter optical wavelengths while simultaneously adjusting the intensity of the diffracted light has made them useful in areas of confocal microscopy [75,76], wavelength division multiplexing [77–79], hyperspectral imaging [80], pulse shaping [81], and metrology [82]. Their characteristics also make them useful as intra-cavity filters within optical resonators [7].

Several AOTF types exist, with quasi-collinear AOTFs (QC-AOTFs) providing advantages over non-collinear AOTFs (NC-AOTFs) for cavity tuning due to their lower drive power requirement, greater side-lobe suppression, and potential for narrower filter bandwidths.

The aim of this chapter is to describe the fundamental principles of AOTF operation and to characterise the performance of a QC-AOTF made from TeO_2 prior to using it intra-cavity.

4.2 Overview of acousto-optic tunable filters

AOTF's use acousto-optic diffraction in anisotropic crystals to produce an optical bandpass filter with a centre frequency determined by phase or momentum matching of orthogonally polarised ordinary and extraordinary waves. These filters are of broad interest as they provide inertia free wavelength control of light. This section will describe the operation of AOTFs that use uniaxial crystals. The optical properties of these crystals will be covered before presenting the acousto-optic interaction.

4.2.1 Optical wave propagation in uniaxial crystals

The propagation of light within a material is dependent on its refractive index n. In some crystalline materials, the refractive index is dependent on the direction of propagation due to its structure. In all uniaxial crystals, the propagation of light can be determined using the index ellipsoid shown in Figure 4.1. This is an ellipsoidal surface where the length of a vector from the origin to each point on the surface defines the refractive index for light polarised in that direction. For a uniaxial crystal, light polarised along the optical axis Z propagates with the extraordinary refractive index n_e while light polarised in the X-Y plane propagates with the ordinary refractive index n_o.

For light propagating in an arbitrary direction $\boldsymbol{k}$ with angle θ to the optical axis, the ordinary polarisation is defined by the direction mutually perpendicular to both $\boldsymbol{k}$ and the optical axis Z. For $\boldsymbol{k}$ in the Z-Y plane, for example, this direction is denoted by the vector $\boldsymbol{B}$ in Figure 4.1. The extraordinary polarisation is defined by the direction mutually perpendicular to both $\boldsymbol{k}$ and $\boldsymbol{B}$, defined by the vector $\boldsymbol{A}$ in the figure.

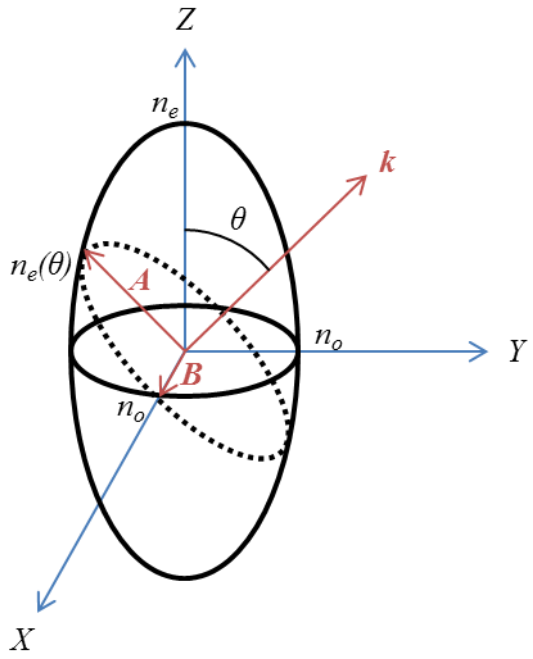

Figure 4.1 Index ellipsoid for uniaxial crystal, where *Z* = optical axis.

The refractive indices for the ordinary and extraordinary polarised components are given by the lengths of vectors ***A*** and ***B***, respectively. Ordinary polarised light will always have refractive index n_o while extraordinary light has a refractive index $n_e(\theta)$ defined by [83]

$$\frac{1}{n_e^2(\theta)} = \frac{\cos^2\theta}{n_o^2} + \frac{\sin^2\theta}{n_e^2}, \tag{4.1}$$

which can be rearranged to give

$$n_e(\theta) = \frac{n_o n_e}{\sqrt{n_o^2 \sin^2\theta + n_e^2 \cos^2\theta}}. \tag{4.2}$$

Additionally, n_o and n_e are wavelength dependent and so the ordinary and extraordinary refractive indices are given by

$$n_o = n_o(\lambda), \tag{4.3}$$

and

$$n_e(\lambda,\theta) = \frac{n_o(\lambda)n_e(\lambda)}{\sqrt{n_o^2(\lambda)\sin^2\theta + n_e^2(\lambda)\cos^2\theta}}. \quad \textbf{4.4}$$

An alternate way to represent the extraordinary and ordinary refractive indices for a uniaxial crystal is shown in Figure 4.2, where two curves for the extraordinary and ordinary polarisation components are used to determine the propagation of light propagating at an angle θ to the optical axis Z. Note that here the curves are plotted for a positive uniaxial crystal where $n_e > n_o$, which is the case for TeO_2.

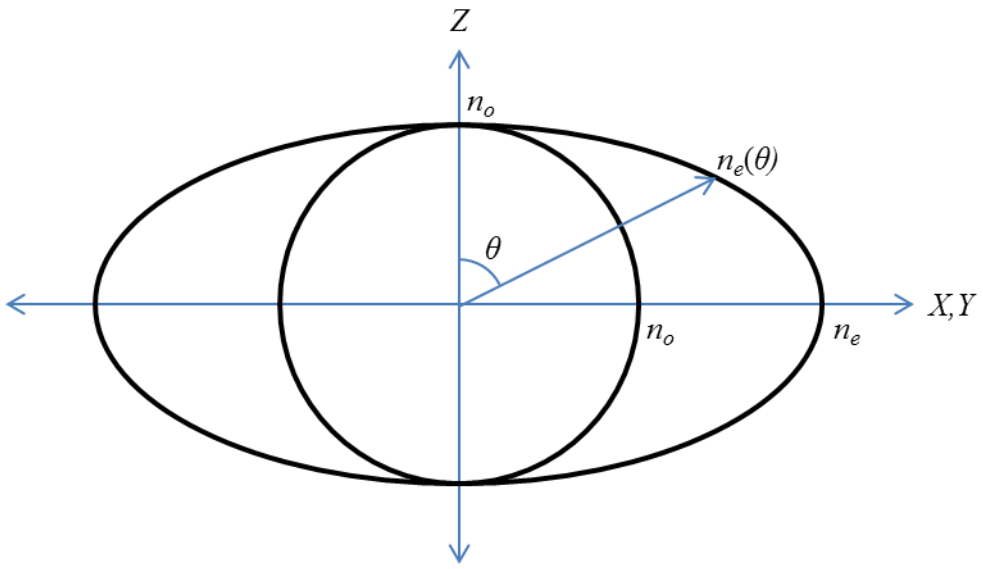

Figure 4.2 Refractive index curves of a positive uniaxial crystal, where Z = optical axis. The ordinary refractive index has a constant radius n_o.

Crystals that are non-centrosymmetric can also exhibit optical activity, where birefringence is induced for light travelling close to the optical axis. For TeO_2, experimental results from AOTF testing has shown that in practice, the effect of optical activity become negligible for propagation angles $\theta > 10°$ [84].

4.2.1.1 Optical properties of TeO_2

Numerous studies on the refractive index of TeO_2 have been reported. The model by Uchida [85] was based on data between 0.4 and 1.0 µm. Berny et al [86] extended the refractive index measurements to 3.5 µm. Georgiev et al [87] proposed the following

dispersion formula based on a two-term Sellmeier dispersion formula, using the data from Uchida and Berny et al:

$$n(\lambda) = \sqrt{1 + \frac{C_0\lambda^2}{\lambda^2 - C_2^2} + \frac{C_1\lambda^2}{\lambda^2 - C_3^2}}. \quad \textbf{4.5}$$

The values for C_0, C_1, C_2, and C_3 corresponding to both n_o and n_e are given in Table 4.1, and plots of n_e and n_o as a function of wavelength are shown in Figure 4.3.

Table 4.1 Constants for C_0, C_1, C_2, and C_3 in the Sellmeier dispersion formula from Equation 4.5 for both n_o and n_e.

	n_o	n_e
C_0	3.71789	4.33449
C_1	0.07544	0.14739
C_2	0.19619	0.20242
C_3	4.61196	4.93667

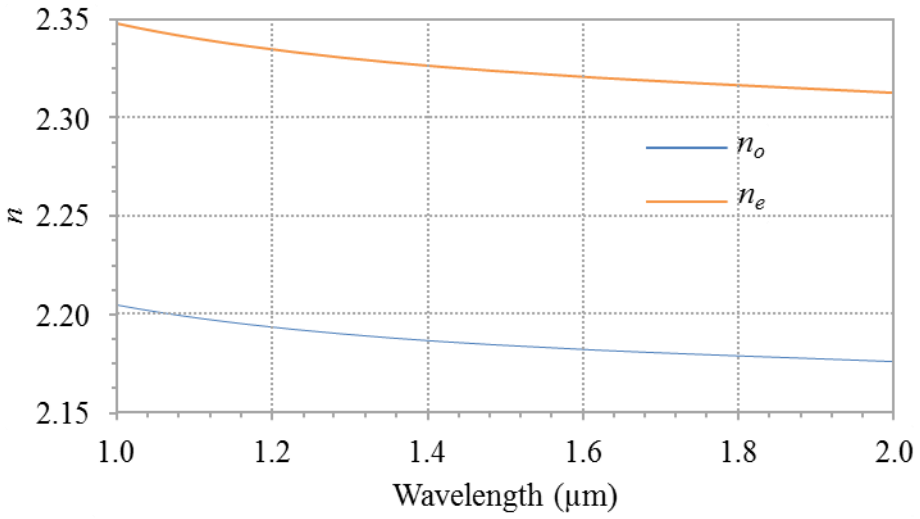

Figure 4.3 Extraordinary and ordinary refractive indices of TeO_2 as a function of wavelength.

4.2.2 Acoustic response of anisotropic crystals

The acoustic response of anisotropic crystals can be characterised using the theory of linear elasticity and the Christoffel equation [83,88]. This equation predicts three acoustic eigenmodes, each with a characteristic vibration direction (or polarisation) and phase velocity $\boldsymbol{V}_a$. Eigenmodes polarised transverse or collinear to $\boldsymbol{V}_a$, are known as pure-shear or pure-longitudinal, respectively. However, in general the polarisations are not pure and contain both transverse and longitudinal components. The mode with the largest component collinear with $\boldsymbol{V}_a$ is typically termed quasi-longitudinal while other non-pure modes are referred to as quasi-shear [88]. Additionally, since the crystal is anisotropic, the group velocity $\boldsymbol{V}_g$ of an acoustic wave is generally not collinear with its phase velocity $\boldsymbol{V}_a$, and thus the acoustic beam "walks off" from the acoustic wavefront normal.

4.2.3 Acousto-optics in uniaxial crystals

In uniaxial crystals, ordinary and extraordinary polarised light can couple to the orthogonal polarisation via acousto-optic (AO) interaction with an acoustic wave [83].

Energy conservation during the AO interaction requires:

$$E_d = E_i \pm E_a, \tag{4.6}$$

where E_i and E_d are the energies of the incident and diffracted light, and E_a is the acoustic phonon energy. Thus, the frequency of the diffracted light is

$$\nu_d = \nu_i \pm f, \tag{4.7}$$

where f is the frequency of the acoustic wave.

For efficient AO interaction, it must be phase matched to ensure constructive interference between the diffracted photons:

$$\boldsymbol{k_d}(\lambda, \theta_i, f, \theta_a) = \boldsymbol{k_i}(\lambda, \theta_i) \pm \boldsymbol{K_a}(f, \theta_a), \tag{4.8}$$

where $\boldsymbol{k}_i$ and $\boldsymbol{k}_d$ are the incident and diffracted optical wavevectors, and $\boldsymbol{K}_a$ is the acoustic wavevector. λ is the wavelength of incident light. θ_i and θ_a are the angles made

between the optical axis and the incident optical wavevector and acoustic wavevector, respectively. AOTFs operate using birefringent AO phase matching, in which the polarisation of the diffracted wave is orthogonal to that of the input wave [83]. An example of such an interaction is shown in the *K*-space diagram in Figure 4.4, assuming an extraordinary polarised input.

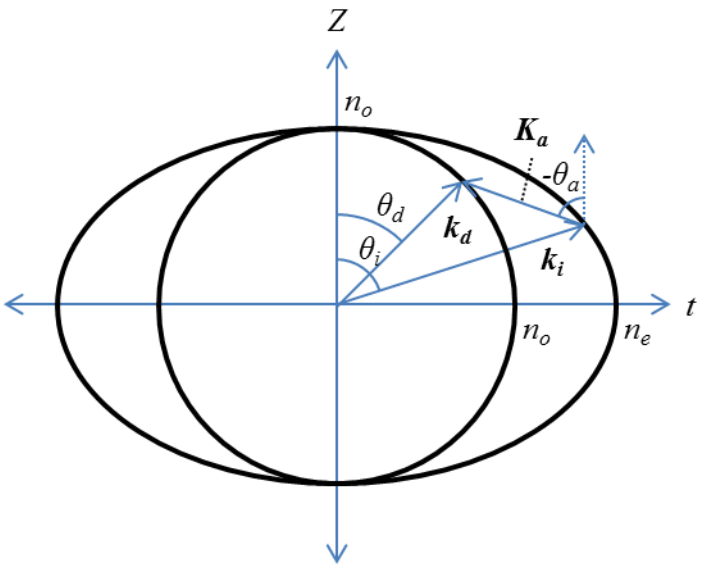

Figure 4.4 *K*-space diagram showing phase matching of incident extraordinary polarised light with acoustic wave vector to produce ordinary polarised diffracted light. Z = optical axis.

The magnitudes of the optical wavevectors $\boldsymbol{k}_i$ and $\boldsymbol{k}_d$ are given by

$$k_{i,d}(\lambda, \theta_{i,d}) = \frac{2\pi n_{i,d}(\lambda, \theta_{i,d})}{\lambda} \qquad \textbf{4.9}$$

where $n_{i,d}$ corresponds to the refractive index experienced by the incident or diffracted light. The magnitude of the acoustic wavevector is given by

$$K_a(f, \theta_a) = \frac{2\pi f}{V_a}, \qquad \textbf{4.10}$$

where f and V_a are the frequency and phase velocity of the acoustic wave respectively. It is thus apparent that a small phase velocity V_a enables operation of piezoelectric

transducers at lower frequencies where they are more efficient. Furthermore, as will later be discussed, smaller V_a are desirable for efficient AO interaction.

Equations 4.8, 4.9, and 4.10 can be combined to yield an expression for the acoustic frequency required to phase match the AO interaction [89]:

$$f = (V_a(\theta_a)/\lambda)\sqrt{n_i^2 + n_d^2 - 2n_i n_d \cos(\Delta\theta)}, \quad \textbf{4.11}$$

where $\Delta\theta = \theta_i - \theta_d$. Additionally, from Figure 4.4:

$$\tan\theta_a = \frac{n_i(\theta_i)\sin\theta_i - n_d \sin\theta_d}{n_i(\theta_i)\cos\theta_i - n_d\cos\theta_d} \quad \textbf{4.12}$$

Therefore, the acoustic frequency required for phase matching in Equation 4.11 can be calculated for a given λ, θ_i, and θ_a.

When the phase matching condition is satisfied, the diffraction efficiency η is [83]

$$\eta = \sin^2\sqrt{\frac{\pi^2}{2\lambda^2}M_2 P_d L^2}, \quad \textbf{4.13}$$

where P_d is the acoustic power density, L is the AO interaction length over which the optical and acoustic waves can interact, and M_2 is the AO figure of merit given by [83]

$$M_2 = \frac{n_i^3 n_d^3 p^2}{\rho V_a^3}. \quad \textbf{4.14}$$

Here, ρ is the material density and p is the effective photo-elastic coefficient for the propagating acoustic mode [83]. It is apparent that a small V_a greatly increases M_2 and reduces the acoustic power requirement.

When using a Gaussian optical beam and an acoustic beam excited by a transducer, the diffraction efficiency will be <1 due to divergence.

From Equation 4.13, the power required for peak diffraction efficiency P_{PDE} is

$$P_{PDE} = \frac{\lambda^2}{2M_2L^2}, \quad \textbf{4.15}$$

which demonstrates the advantage of a long interaction length L for achieving low drive powers.

4.2.4 AOTF configurations

Three AOTF configurations have been identified: collinear, non-collinear, and quasi-collinear. Typical geometries for these configurations along with phase matching diagrams are shown in Figure 4.5.

The first AOTFs developed operated in a collinear regime [90], where the incident wave $\boldsymbol{k}_i$ propagates collinear to the acoustic wave $\boldsymbol{K}_a$, resulting in the diffracted wave $\boldsymbol{k}_d$ being collinear to $\boldsymbol{k}_i$. This configuration allows long AO interaction lengths but requires a polariser to separate the undiffracted and diffracted beams exiting the AOTF. Additionally, large acceptance angles are possible since the tangents to the refractive index surfaces for $\boldsymbol{k}_i$ and $\boldsymbol{k}_d$ are parallel, making the phase matching condition less sensitive to changes in optical input angle. One of the key disadvantages of this configuration is that it is only permitted for certain crystal classes [91]. This prevents its use with crystals that are easier to manufacture and exhibit better AO properties for filtering [91].

In the non-collinear configuration the incident wave $\boldsymbol{k}_i$, acoustic wave $\boldsymbol{K}_a$, and diffracted wave $\boldsymbol{k}_d$ all propagate at different angles within the material, allowing materials with high AO figure of merit to be used [92]. Typically, these non-collinear devices are designed to maximise their acceptance angle by operating under the parallel tangents regime, where the tangents to the refractive index surfaces are parallel for $\boldsymbol{k}_i$ and $\boldsymbol{k}_d$, just as they are in the collinear configuration [93]. This makes non-collinear interaction ideal for hyperspectral imaging and confocal microscopy [75,76,80]. However, the interaction length is restricted by the physical dimensions of the transducer, resulting in limited spectral resolution compared to the collinear configuration.

The quasi-collinear configuration is a special case of the non-collinear regime where acoustic walk-off is exploited such that the acoustic group velocity $\boldsymbol{V}_g$ is parallel to the

incident wave $\boldsymbol{k_i}$ [94]. This allows the benefits of a long interaction length to be realised with crystals of good AO properties that cannot operate in a collinear regime. This combination results in the lowest drive power requirements. However, the acceptance angle for this interaction is limited since it does not operate under the parallel tangents condition, and typically requires a diffraction limited optical input [95]. This has limited its possible applications to those using collimated light such as wavelength division multiplexing (WDM) [79,96,97] and laser tuning [98].

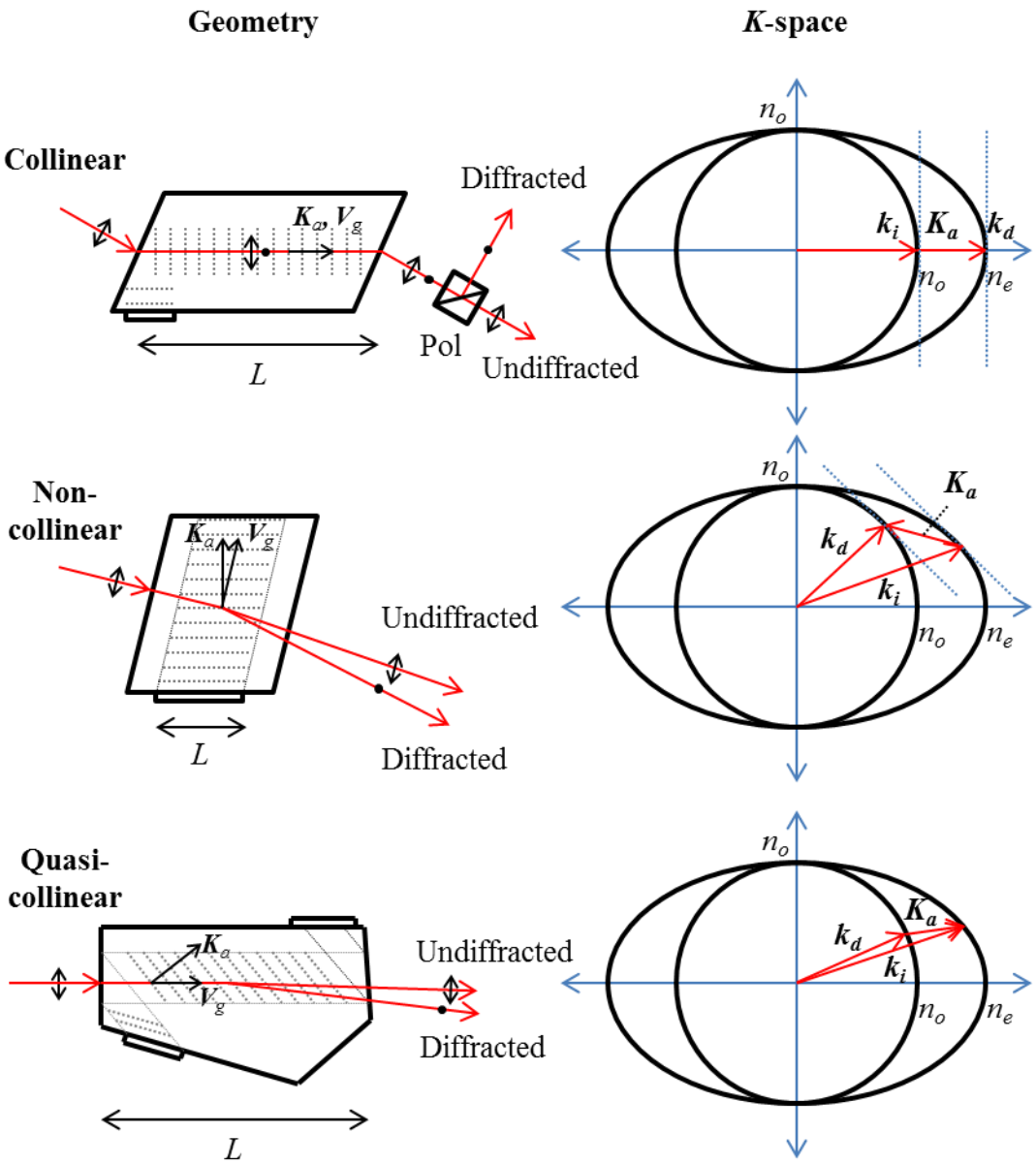

Figure 4.5 Geometry and *K*-space diagrams of collinear, non-collinear, and quasi-collinear acousto-optic interaction. L = acousto-optic interaction length, $\boldsymbol{k_i}$ and $\boldsymbol{k_d}$ = incident and diffracted optical wavevector, $\boldsymbol{K_a}$ = acoustic wavevector.

A summary of advantages and disadvantages of the three AO interaction regimes in Figure 4.5 is given in Table 4.2, along with typical applications.

Table 4.2 Comparison between collinear, non-collinear, and quasi-collinear acousto-optic interaction.

	Advantages	**Disadvantages**	**Applications**
Collinear	• Long interaction region allows narrow spectral resolution. • Large acceptance angle.	• Limited to using materials with not as high AO figure of merit, resulting in higher drive power requirements • Difficult to manufacture	• Image processing • Laser tuning
Non-collinear	• Able to use crystals with high AO figure of merit. • Large acceptance angle	• Limited spectral resolution • Higher drive power requirements due to short interaction lengths	• Image processing • Laser tuning
Quasi-collinear	• Long interaction region coupled with using good AO materials allows narrow spectral resolution and low drive power requirements	• Narrow acceptance angle typically restricts input to a diffraction limited beam	• Laser tuning • Add-drop WDM

4.2.5 Acousto-optic tunable filters using TeO_2

Tellurium dioxide (TeO_2), also known as paratellurite, is commonly used for AOTFs due to its 450 – 4500 nm transmission band, relative ease of manufacture [84], and the

low velocity of its pure-shear mode. Unfortunately, this crystal belongs to the 422 tetragonal class, which does not permit collinear diffraction of light [83]. Thus, to enable long interaction lengths a quasi-collinear configuration must be used.

The pure-shear mode that propagates in the plane defined by the [110] and [001] axes (*t*-*Z* plane) is polarised transverse to this plane and has a phase velocity V_a given by [83]

$$V_a^2(\theta_a) = V_t^2 \sin^2 \theta_a + V_z^2 \cos^2 \theta_a \,, \qquad \textbf{4.16}$$

where θ_a is the angle from the optical axis *Z* to the wavefront normal. V_t and V_z are the phase velocities along the [110] and *Z* direction respectively, given by [83]

$$\begin{aligned} V_t &= 616 \text{ m/s}, \\ V_z &= 2104 \text{ m/s}. \end{aligned} \qquad \textbf{4.17}$$

To obtain the direction of energy flow (group velocity direction) of the pure-shear wave, it is convenient to plot the curve corresponding to the inverse phase velocity $1/V_a$, also known as the acoustic slowness curve. This is shown in Figure 4.6, where a pure-shear wave propagates in the *t*-*Z* plane with angle θ_a from the optical axis *Z* to the wavefront normal (direction of the phase velocity). The direction of energy flow will be in the *t*-*Z* plane and lies along the normal to the $1/V_a$ curve [83], as shown in Figure 4.6. The resulting walk off angle Ψ between the group and phase velocities is given by [83]

$$\tan \Psi = \frac{(V_z^2 - V_t^2) \sin(2\theta_a)}{2V_a(\theta_a)}. \qquad \textbf{4.18}$$

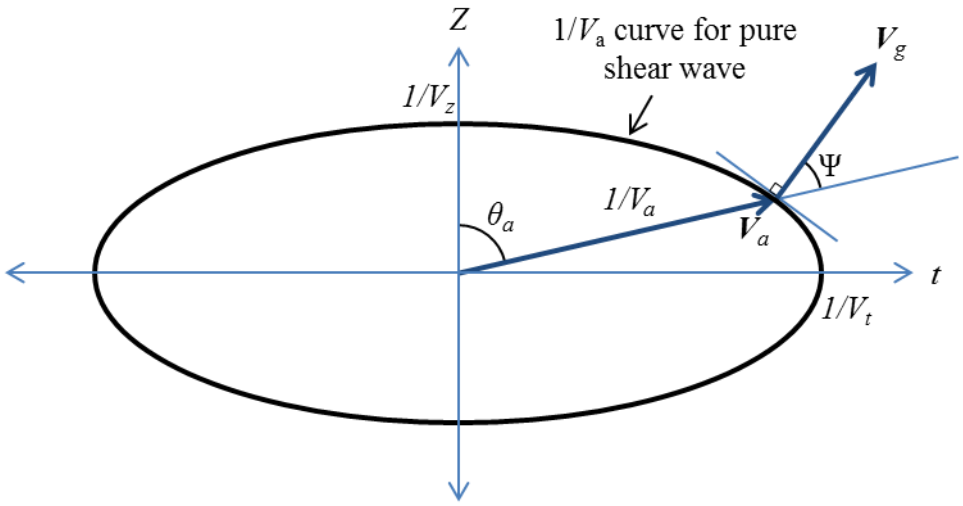

Figure 4.6 Acoustic slowness curve $1/V_a$ for the *t*-*Z* plane of TeO_2, with an acoustic wave propagating with phase velocity V_a at angle θ_a from the *Z* axis. The group velocity propagates with walk off angle Ψ from the phase velocity.

4.3 Our TeO_2 acousto-optic tunable filter

The Gooch & Housego, TF1650-1100-2-3-GH40 quasi-collinear AOTF (QC-AOTF) we used is made from single crystal TeO_2. Its configuration is shown in Figure 4.7(a), with a diagram of the phase matching shown in Figure 4.7(b). To generate the pure-shear wave desired for efficient AO diffraction, the transducer first generates a quasi-longitudinal acoustic wave. This wave propagates with a walk off to the optical input facet, where it undergoes anisotropic reflection thereby coupling it to the pure-shear wave in the *t*-*Z* plane [99]. The reflected wave propagates with walk-off angle Ψ such that the group velocity is collinear to the input optical wave. The phase matching in Figure 4.7(b) results in the frequency of the diffracted light to be downshifted.

To ensure good pointing stability of the diffracted light exiting the AOTF such that its direction is independent of wavelength, the output facet is cut at an angle to provide dispersion compensation.

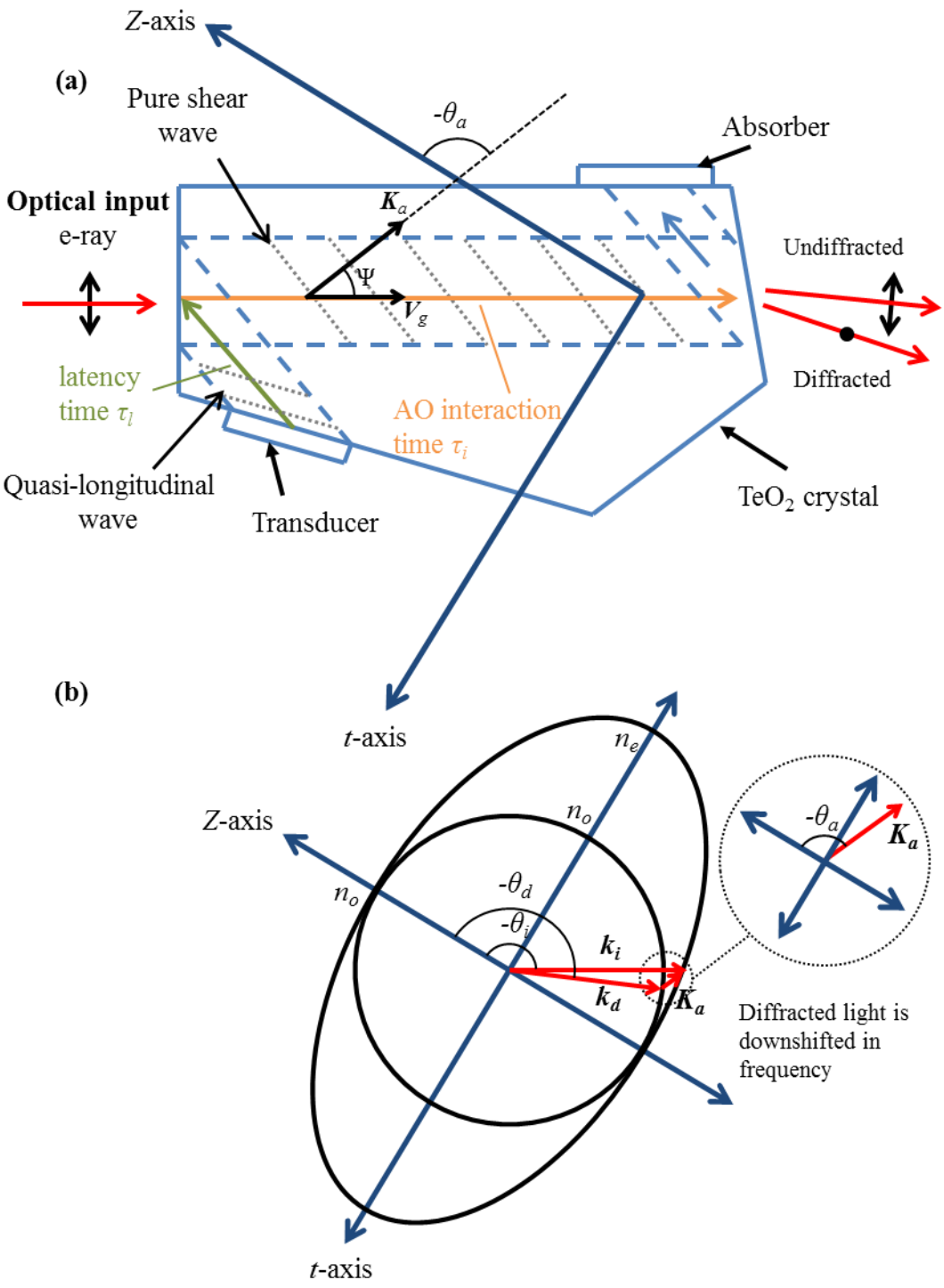

Figure 4.7 (a) Configuration of the selected AOTF. (b) Phase matching diagram of the selected AOTF. Z = optical axis, $\boldsymbol{K_a}$ = acoustic phase velocity wavevector, $\boldsymbol{V_g}$ = acoustic group velocity, $\boldsymbol{k_i}$ = incident optical wavevector, $\boldsymbol{k_d}$ = diffracted optical wavevector, Ψ = acoustic walk-off angle, θ_i = angle of incident light, θ_d = angle of diffracted light, θ_a = angle of acoustic wave

There will be a latency time τ_l from the application of the RF signal to the acoustic wave reflecting off the input optical facet, after which it can interact with the optical wave.

The AO interaction time τ_i is given by the acoustic travel time over the interaction length L:

$$\tau_i = \frac{L \cos \Psi}{V_{ph}}. \quad \textbf{4.19}$$

The specifications given for the AOTF are shown in Table 4.3. These values assume a diffraction limited input beam and a beam diameter of 1.5 mm.

Table 4.3 Specifications for the selected AOTF.

Tuning range	1100 – 2200 nm
Wavelength resolution at 1650 nm	<2 nm
Electrical drive power at 1650 nm	150 mW
Diffraction efficiency	>75%
Recommended beam diameter	1.5 mm

The characteristics of the AOTF which will be measured in the next section include the tuning relation between acoustic and optical frequencies, acoustic power for peak diffraction efficiency, and the optical and acoustic bandwidths.

The diffraction due to driving the AOTF at frequency f is shown schematically in Figure 4.8 for both extraordinary and ordinary input polarisations. The diffracted light is frequency shifted by $-f$ for an extraordinary polarised input and $+f$ for ordinary polarisation. The diffraction efficiency here is defined by the ratio of the diffracted light when driving the AOTF to the undiffracted light with no driving signal.

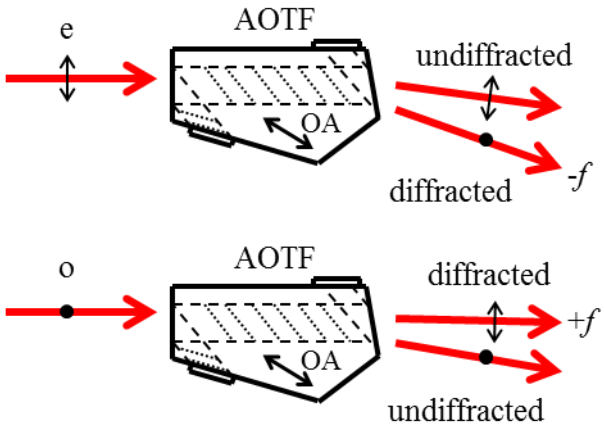

Figure 4.8 Operation of AOTF for extraordinary and ordinary polarised input. The diffracted light is frequency shifted by ±*f*, where *f* is the driving frequency of the AOTF. e = extraordinary polarised input, o = ordinary polarised input, OA = optical axis.

4.4 AOTF test system

Prior to using the AOTF for intra-cavity laser tuning in Chapter 5, it was characterised and its performance compared with the equations and specifications presented in Sections 4.2 and 4.3. First, the tuning curves for the QC-AOTF were measured for a narrowband input. The experimental layout is shown in Figure 4.9. The same test system was used for measuring the diffraction efficiency as a function of the drive power, the acoustic bandwidth, and temporal response.

The diffraction-grating tuned superluminescent diode (SLED) source described in Section 3.3.2 provided the probe beam, which was polarised either extraordinary or ordinary using a half-wave plate. A polariser was added after the wave plate to ensure high purity of the incident polarisation. The AOTF was driven by a signal generator (BK Precision, 4064), which did not need further amplification due to the low power requirement (~200 mW) of the QC-AOTF. The signal generator was set to a 50 Ω impedance to match the input impedance of the AOTF.

The tuning curve for both polarisations was measured by first rotating the AOTF until maximum diffraction efficiency was achieved for a fixed wavelength input and acoustic frequency. Then, the input wavelength was varied and the drive frequency required for maximum diffraction efficiency was recorded. The diffraction efficiency was defined as the ratio of the diffracted light when driving the AOTF to the undiffracted light with no

driving signal. The input wavelength was monitored with an optical spectrum analyser (OSA, Yokagawa, AQ6375) and the powers measured using a thermal power meter. However, for measurements of diffraction efficiency vs AOTF drive power and the AOTF's acoustic bandwidth, the sensitivity of the thermal power meter was inadequate and a calibrated photodiode power meter (Thorlabs, S155C) was used.

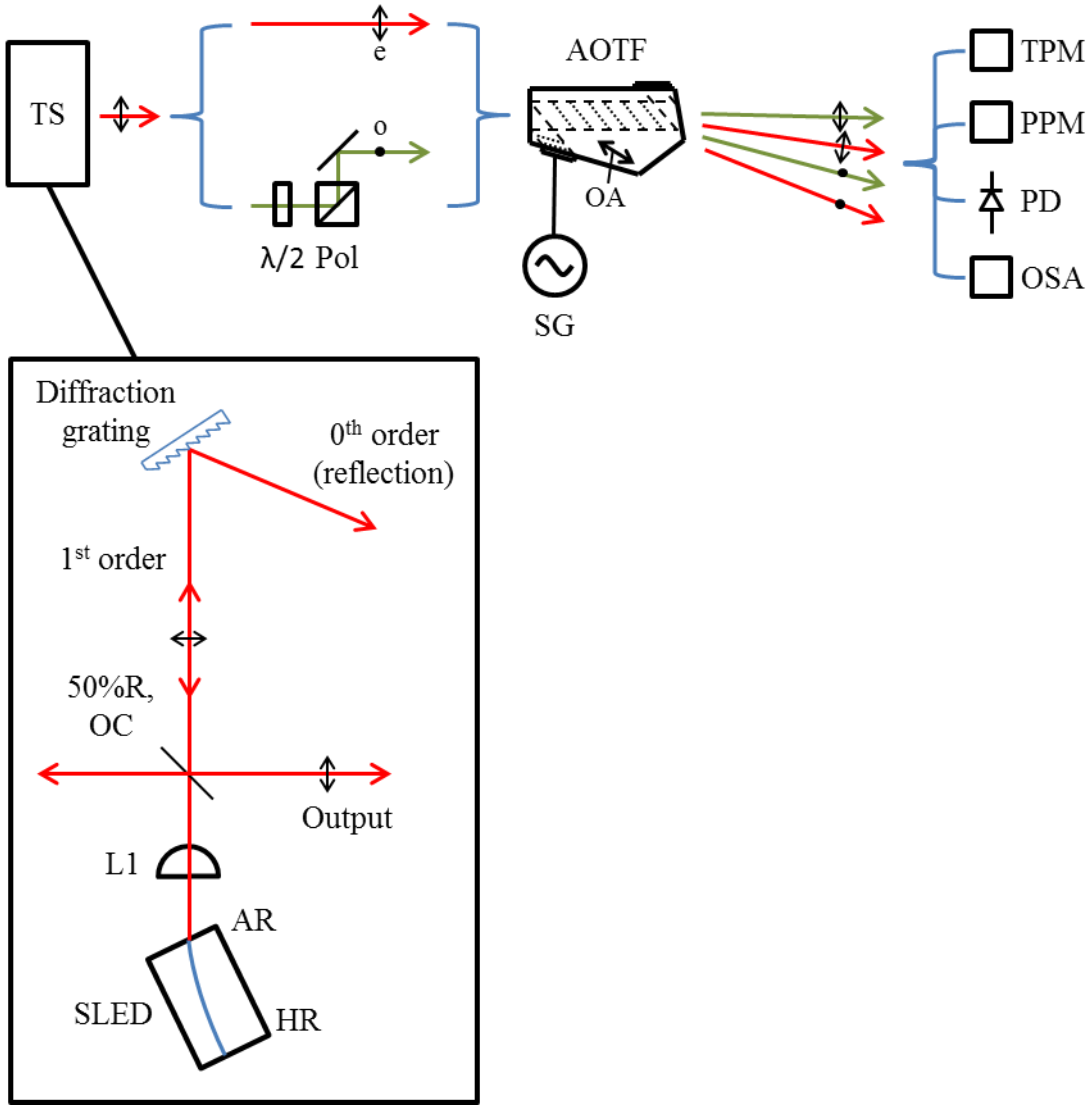

Figure 4.9 Schematic for characterisation of QC-AOTF. TS = grating tuned semiconductor source from Section 3.3.2, λ/2 = half-wave plate, Pol = polariser, SG = signal generator, TPM = thermal power meter, PPM = photodiode power meter, PD = photodiode, OSA = optical spectrum analyser, e = extraordinary polarisation, o = ordinary polarisation, OA = optical axis.

A photodiode (Thorlabs, DET10D/M, response time = 25 ns) connected to a 60 MHz oscilloscope (Tektronix, TDS 210) was used to measure the temporal response by observing the rise and fall time of the diffraction efficiency when a 100 µs acoustic RF pulse is applied.

4.5 Results

4.5.1 Tuning curve

The measured tuning curve of the AOTF for both extraordinary and ordinary input polarisations is shown in Figure 4.10. Using Equation 4.11 and 4.12, the extraordinary polarised input data gives θ_i = -137°, θ_a = -94°, and $\Delta\theta$ = 1.5°. The data for ordinary polarised input using the same acoustic angle θ_a gives θ_i = -137°, and $\Delta\theta$ = -1.5°. This is summarised in Table 4.4. The values for θ_i and $\Delta\theta$ will be used in the following sections to estimate the acoustic phase velocity V_a and walk-off angle Ψ.

An offset in acoustic and optical frequency between the curves exist of $\Delta f \sim 1$ MHz and $\Delta\lambda \sim 50$ nm at 1650 nm, respectively.

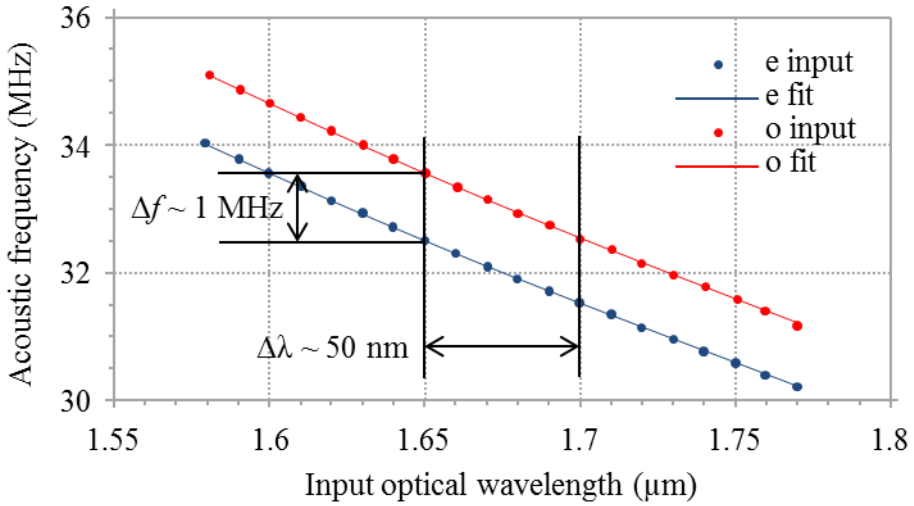

Figure 4.10 Tuning relation of acoustic and optical frequency for both extraordinary and ordinary polarised input light.

Table 4.4 Predicted values for θ_i and θ_a for extraordinary and ordinary input polarisation based on the best fit curves shown in Figure 4.10.

Input polarisation	$\boldsymbol{\theta_i}$	$\boldsymbol{\Delta\theta}$	$\boldsymbol{\theta_a}$
Extraordinary	-137°	-1.5°	-94°
Ordinary	-137°	1.5°	-94°

4.5.2 Diffraction efficiency vs drive power

The diffraction efficiency as a function of AOTF drive power for extraordinary polarised input is shown in Figure 4.11. The input wavelength and corresponding acoustic frequency for diffraction were fixed at 1650 nm and 32.51 MHz during the measurement. The diffraction efficiency increases with drive power up to ~78% at 200 mW, where it begins to roll over. At 150 mW the efficiency is ~75%, which is within the specifications of the AOTF.

The diffraction efficiency expression in Equation 4.13 predicts a curve of the form

$$\eta = a \sin^2 \sqrt{b \times P}, \qquad \textbf{4.20}$$

where a and b are constants, and P is the acoustic power. The measured data agrees with this expression as shown by the fitted curve in Figure 4.11.

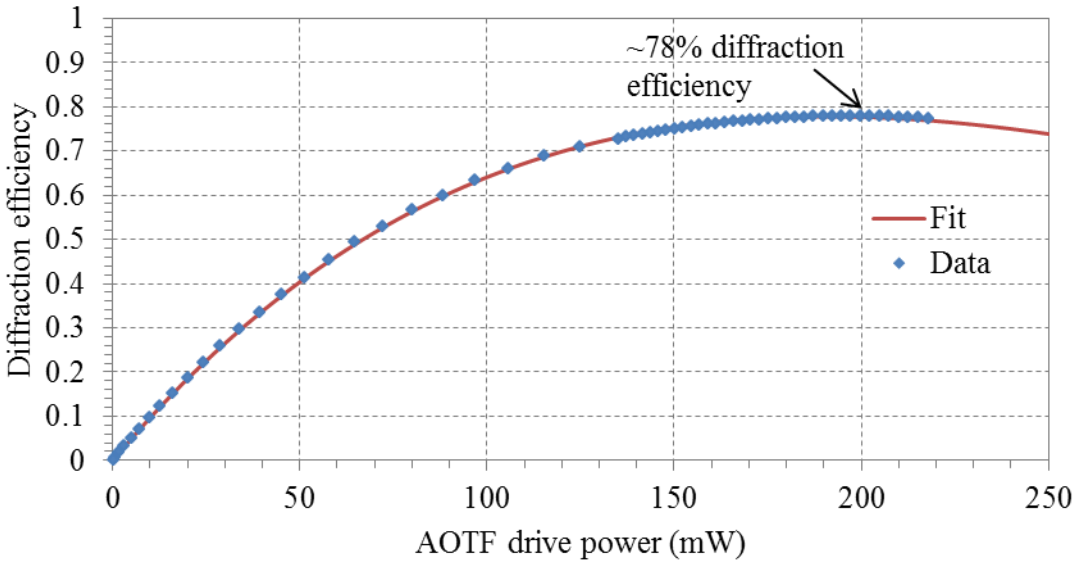

Figure 4.11 Diffraction efficiency as a function of AOTF drive power. Overlaid is a best-fit curve based on the diffraction efficiency expression in Equation 4.20.

4.5.3 Acoustic bandwidth

The acoustic bandwidth was measured by varying the AOTF drive frequency for a fixed 1650 nm input optical wavelength and 200 mW AOTF drive power. The results are shown in Figure 4.12. The curve has a peak in efficiency at 32.52 MHz as expected, with a $\delta f \sim 48$ kHz acoustic FWHM. The curve appears asymmetric, with a shallower drop in diffraction efficiencies at larger drive frequencies. At the lower drive frequencies, a side-lobe is visible ~60 kHz from the peak.

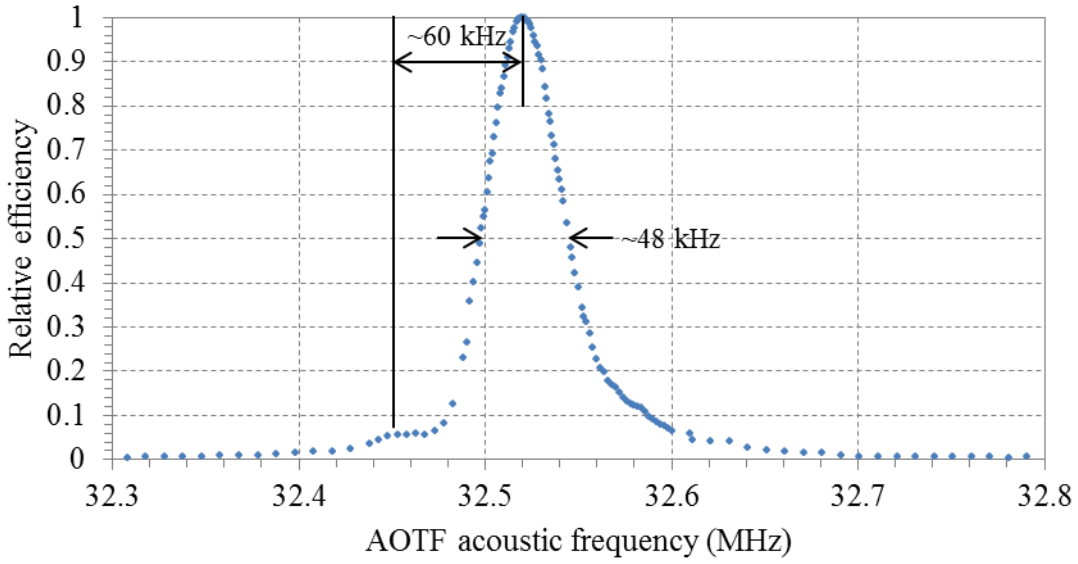

Figure 4.12 Diffraction efficiency relative to its optimum value as a function of AOTF drive frequency for a 1650 nm optical input and 200 mW AOTF drive power.

4.5.4 Temporal response

The AOTF response to a 100 µs acoustic RF pulse is shown in Figure 4.13. The diffraction efficiency is measured relative to CW operation. There is a τ_l = 8 µs latency from driving the AOTF to when the diffracted beam is first detected. From here it takes a further 21 µs for the diffracted light to reach maximum efficiency, indicating an interaction time of τ_i = 21 µs. This is mirrored at the end of the 100 µs acoustic wave, where there is an 8 µs delay before the diffracted power begins to drop, and a further 21 µs before no diffracted light is measured. This results in a 29 µs total response time for the AOTF.

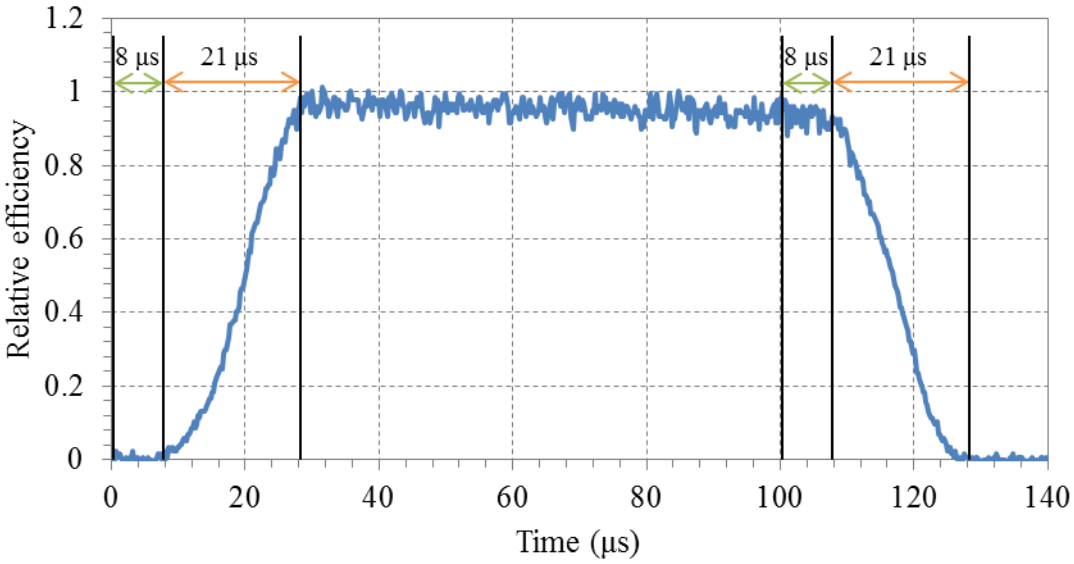

Figure 4.13 AOTF diffraction efficiency during a 100 µs acoustic RF pulse measured relative to the diffraction efficiency for a continuous acoustic wave. Time t = 0 corresponds to the beginning of the pulse.

4.6 AOTF optical bandwidth test system

The filtering by the QC-AOTF of a broadband input was measured using the configuration in Figure 4.14. The collimated broadband amplified spontaneous emission (ASE) from the SLED in Section 3.2 was directed onto the AOTF. The bandwidth is obtained by performing a relative measurement of the diffracted spectrum with a drive signal to the AOTF to the undiffracted spectrum when no drive signal is applied. This helps to reduce the etalon effects present in the ASE source on the measurement.

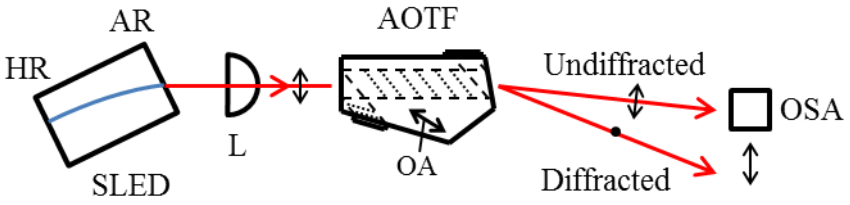

Figure 4.14 Schematic for characterisation of the optical filter bandwidth of the AOTF. SLED = superluminescent diode, HR = 90% reflective facet, AR = anti-reflection coated facet, AOTF = acousto-optic tunable filter, L = 3.1 mm, AR-coated aspheric lens, OSA = optical spectrum analyser, OA = optical axis.

4.6.1 Results

The AOTF filter response for a broadband input when driven at 31.2 MHz is shown in Figure 4.15. There is a peak in efficiency at ~1649.9 nm with 3 dB bandwidth of ~2.4 nm. A side-lobe appears 3.65 nm to the right of the peak, at 1653.55 nm.

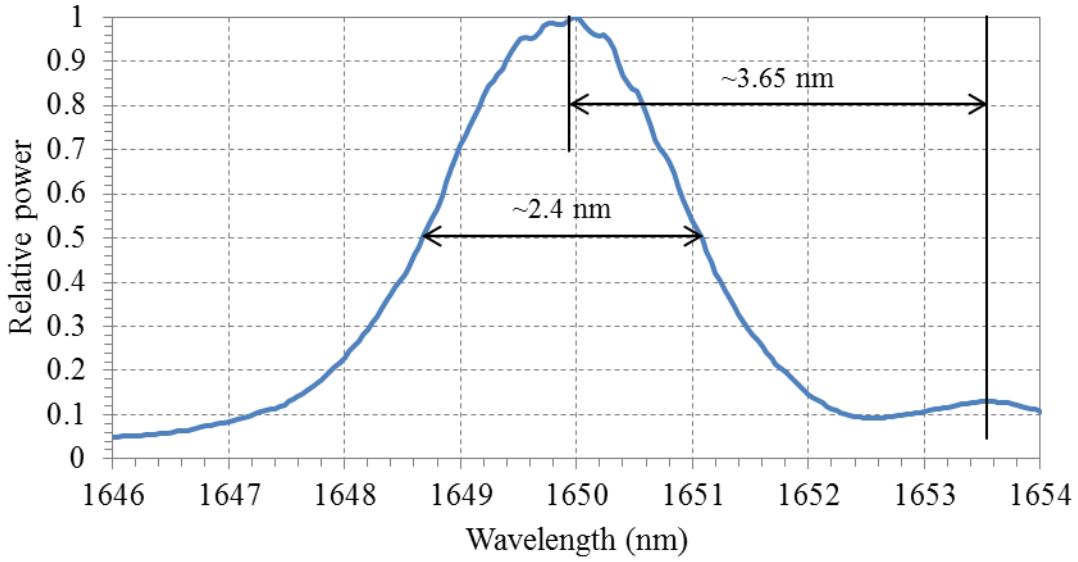

Figure 4.15 AOTF filter response for a broadband input when driven at 31.2 MHz. The filtered light is measured relative to the undiffracted light with no AOTF drive signal, then normalised to the peak value. An OSA resolution setting of 0.05 nm was used.

4.7 Discussion

The tuning curves for both extraordinary and ordinary input polarisations in Figure 4.10 resulted in an estimated acoustic angle to the optical axis of $\theta_a \sim$ -94°. Using the expressions for phase velocity V_a and walk-off angle Ψ in Equations 4.16 and 4.18 gives

$$V_a = 629 \text{ m/s}, \quad \textbf{4.21}$$

$$\Psi = 35°. \quad \textbf{4.22}$$

The ~75% diffraction efficiency at 1650 nm was within specifications for the AOTF, however the small acceptance angle of the QC-AOTF resulted in efficiencies being sensitive to alignment. The 200 mW drive power and 2.4 nm optical bandwidth at 1650 nm for the QC-AOTF differs from the 150 mW drive power and <2 nm optical

bandwidth in its specifications. This could be attributed to the specifications of the AOTF assuming a collimated, diffraction limited input beam and an optimum optical incident angle for phase matching, which may not have been satisfied for these measurements. Additionally, the 1.5 mm recommended beam diameter for the AOTF is larger than the ~1 mm waist used. Nonetheless, a 200 mW drive power is relatively low when compared to non-collinear AO devices which typically require power levels in the order of Watts.

The $\tau_l = 8$ µs latency and $\tau_i = 21$ µs AO interaction rise/fall time measured in Figure 4.13 for the AOTF are expected from the corresponding interaction length. Inserting the 21 µs interaction time in Equation 4.19 results in a crystal interaction length of $L = 16$ mm, which corresponds well with the AOTF's dimensions. The origin of τ_l and τ_i are shown in Figure 4.16. If placing the AOTF intra-cavity these response times will play a significant role in transient laser dynamics.

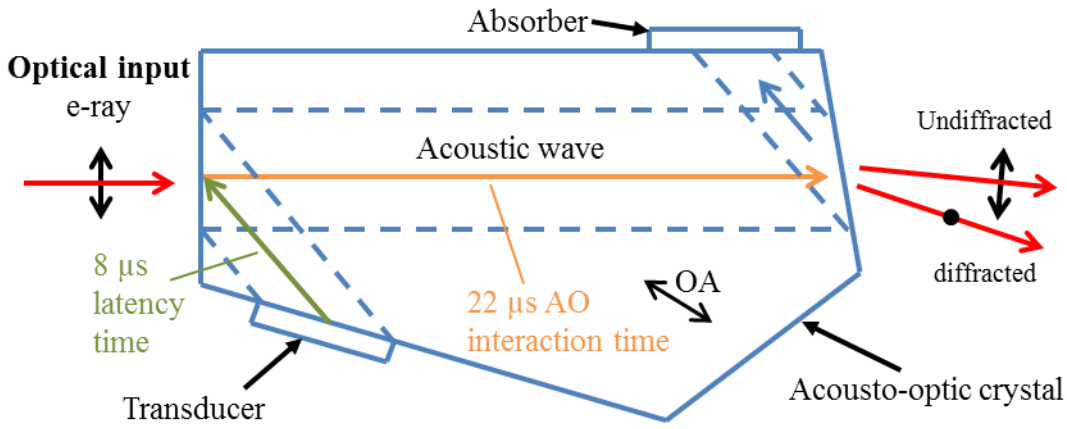

Figure 4.16 Layout of the QC-AOTF used, indicating the experimentally measured latency and interaction time. OA = optical axis.

4.8 Summary

In this chapter the operating principles of AOTFs was given, and a QC-AOTF was characterised. The AOTF was tuned across a 190 nm wavelength range from 1580 – 1770 nm which was limited by the tunable RF source. In principle, the AOTF used has an operation range spanning 1100 – 2200 nm. The optimum drive power of 200 mW corresponded to a maximum diffraction efficiency of 78%. The FWHM optical and acoustic filter bandwidths were 2.4 nm and 48 kHz, respectively. The AOTF has an

8 µs latency from when an RF signal is applied and a 21 µs AO interaction time over the quasi-collinear section of the crystal. This response will affect transient dynamics of a laser built with the device.

The results in this chapter highlight some of the advantages this QC-AOTF tuned laser has over other tuning methods. It is purely electronically controlled, has wideband tunability, relatively low power requirements, and an ability to tune to any wavelength in its tuning range within the total 29 µs travel time of the acoustic wave.

Chapter 5
Quasi-collinear acousto-optically tuned diode lasers

5.1 Introduction

The wide tuning range, small response time, and lack of movement of acousto-optic tunable filters (AOTFs) make them attractive for building tunable laser sources. Early AOTF tuned sources were based on dye lasers [6,7]. Later, sources based on Ti:Al_2O_3 [8,100], semiconductors [11,12], and fibres [10] were developed.

Initially, AOTF tuned semiconductor sources were typically investigated for use in the telecommunications industry [12,16,101]. However, more recently they have gained interest for use in swept-source optical coherence tomography (SS-OCT) [13,15,98,102–107], with some being commercialised [108]. These sources are based around the 800 – 1200 nm region for OCT applications. The critical parameters for sources used in this application are sweep rates, tuning bandwidth, and instantaneous linewidths, as these influence OCT scan rates and axial resolution. Typical values for these are ~10^4 nm/s sweep rates, ~100 nm bandwidths across the 700 – 1200 nm spectral region, and ~0.05 – 0.001 nm instantaneous linewidths.

The aim of this chapter is to describe the results of a detailed investigation into the performance and limitations of AOTF tuned semiconductor lasers operating between

~1600 nm – 1800 nm in steady state, wavelength swept, and wavelength agile operating regimes. Two tunable sources are constructed using the QC-AOTF from Chapter 4. In Section 5.2, the superluminescent diode (SLED) from Section 3.2 is used as the gain media. A semiconductor optical amplifier (SOA) gain medium laser is reported in Section 5.3.

5.2 AOTF-tuned superluminescent diode cavity

5.2.1 Cavity designs

The aim of the investigation reported here was to determine the optimum cavity configuration for the AOTF tuned SLED laser. The SLED from Section 3.2 was used as the gain medium. The cavity configurations tested are shown in Figure 5.1. In all of them, the SLED was collimated using a 3.2 mm focal length, anti-reflection (AR) coated aspheric lens. The collimated beam was propagated through the AOTF and the diffracted beam fed back to the SLED by either a highly reflective (HR) mirror for Figure 5.1(a),(b) and (d), or an R = 50% output coupler in Figure 5.1(c). In Figure 5.1(a) and (b), output coupling was provided by a 50% reflective beam-splitter placed between the AOTF and either the collimating lens or the HR mirror, respectively. For Figure 5.1(d), the output was the residual undiffracted beam exiting the AOTF, or the output from the HR facet of the SLED.

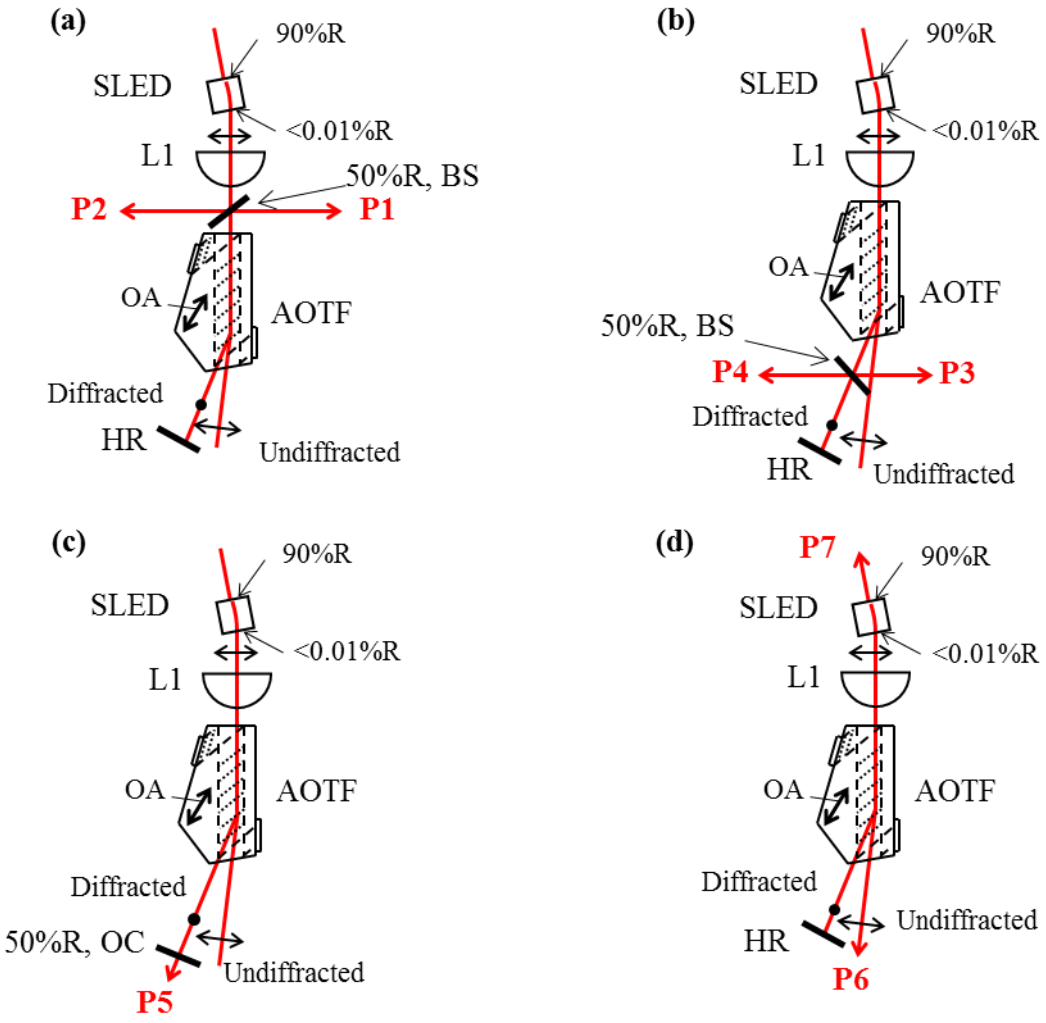

Figure 5.1 Cavity configurations tested for AOTF tuned semiconductor laser. L1 = 3.2 mm AR coated aspheric lens, BS = ~50% beamsplitter, OC = ~50% output coupler, HR = highly reflective mirror, SLED = superluminescent diode, AOTF = acousto-optic tunable filter, OA = optical axis.

The double pass of the AOTF in each cavity configuration results in two downshifts in optical frequency due to acousto-optic (AO) interaction. This is shown in Figure 5.2, which is an expansion of the phase matching diagram in Figure 4.7(b) to include both forward and reverse passes of the AOTF. In the forward pass, the incident and diffracted wave vectors $\boldsymbol{k}_i$ and $\boldsymbol{k}_d$ have extraordinary and ordinary polarisations respectively, and the diffracted light is downshifted in frequency. On the reverse pass, the polarisations of the incident and diffracted wave vectors are swapped, however the acoustic wave vector is unchanged. This results in the diffracted light being downshifted again in frequency. The total roundtrip frequency shift is therefore $2f$, where f is the AOTF drive frequency.

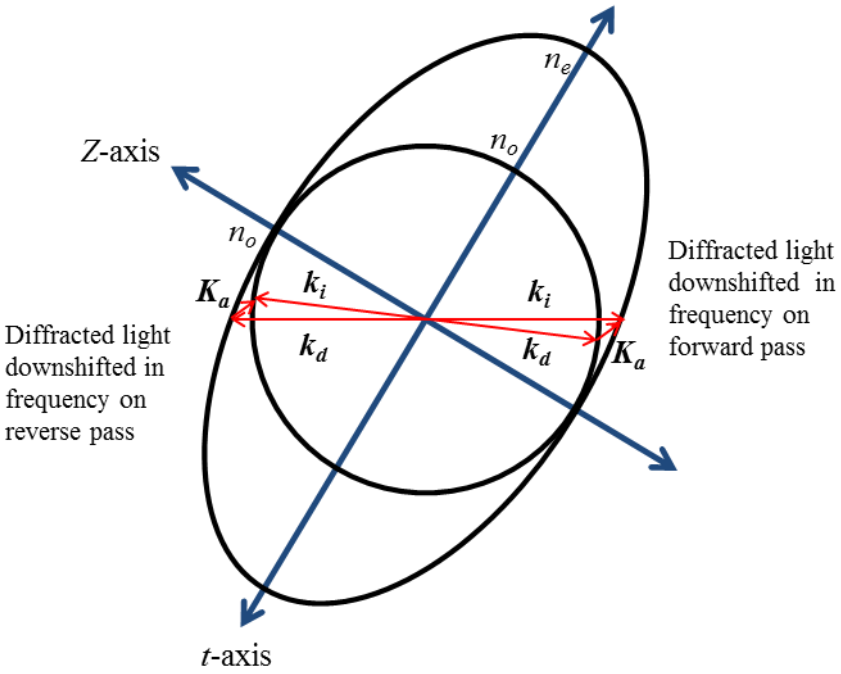

Figure 5.2 Phase matching diagram of the AOTF for both forward and reverse passes. Z = optical axis, $\boldsymbol{K_a}$ = acoustic phase velocity wavevector, $\boldsymbol{k_i}$ = incident optical wavevector, $\boldsymbol{k_d}$ = diffracted optical wavevector.

The output spectra of the cavities in Figure 5.1 were measured using an optical spectrum analyser (OSA, Yokagawa, AQ6375) and powers measured using a thermal power meter (Thorlabs, S302C). The SLED was operated with a 500 mA injection current, and the AOTF was driven using 200 mW of power at 32.4 MHz. This corresponded to an operating wavelength of ~1650 nm. The results for the different configurations are shown in Table 5.1 [109].

Table 5.1 Power, optical signal to noise ratio (OSNR), and linewidth measurements for the outputs from the various configurations in Figure 5.1.

	P1	**P2**	**P3**	**P4**	**P5**	**P6**	**P7**
Power (mW)	9.3	24	13.1	4.7	17.0	42	0.3
OSNR (dB)	>65	42	>67	>65	>69	36	35

From Table 5.1, the optical signal to noise ratio (OSNR) for outputs P1, P3, P4, and P5 are superior to the rest, due to amplified spontaneous emission (ASE) from the SLED being filtered by the AOTF before out-coupling.

Output P5 was selected for further characterisation due to its larger output power and more compact cavity.

5.2.2 Characterisation of SLED/AOTF cavity

The setup used for characterising steady state and wavelength agile operation for the selected cavity is shown in Figure 5.3. The average power was measured with a thermal power meter (Thorlabs, S302C). Spectral properties of the laser were measured using an OSA (Yokagawa, AQ6375). The temporal response was measured with a DC-coupled, extended InGaAs photodiode (Thorlabs, DET10D/M, response time = 25 ns) connected to a 60 MHz bandwidth oscilloscope (Tektronix, TDS 210).

Wavelength agile operation was achieved by changing the frequency of the AOTF drive signal. Two switching methods to transition from wavelength λ_1 to λ_2 were investigated. The first applied a square wave to provide discrete switching between operating wavelengths of the laser. The second used a linear ramp to sweep the wavelength from λ_1 to λ_2.

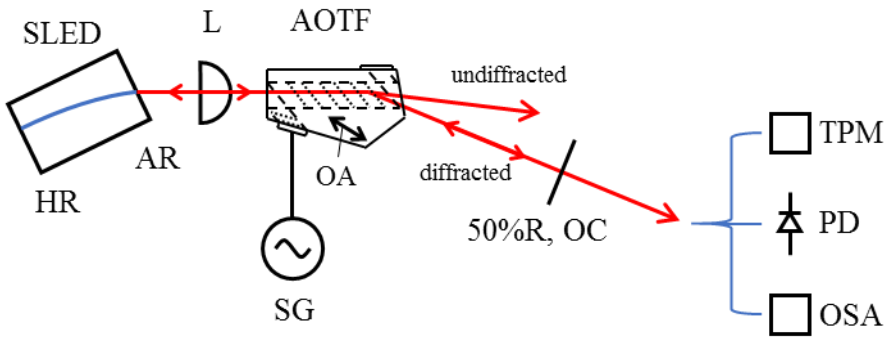

Figure 5.3 Schematic for characterisation of the QC-AOTF tuned semiconductor laser. SLED = superluminescent diode, L = 3.1 mm focal length AR-coated aspheric lens, SG = signal generator, OC = ~50% reflective output coupler, AOTF = acousto-optic tunable filter, TPM = thermal power meter, PD = photodiode, OSA = optical spectrum analyser.

Instantaneous linewidth measurements of swept sources can be made using a variety of techniques. These include temporal analysis of the reflection or transmission by a narrowband fibre Bragg grating [10], a Fabry-Perot etalon/interferometer [102,106], or a Fourier transform of the interference fringe visibility [110,111].

An alternative technique used here is to sample short pulses at the same temporal position during a wavelength sweep, and measure the average spectrum of each set of pulses [112]. Provided the pulse-to-pulse jitter is sufficiently low, these pulses should have the same wavelength.

The setup used for measuring the instantaneous emission linewidth is shown in Figure 5.4. The pulses were sliced from the swept laser output using a polygon rotating mirror (PRM, Precision Laser Scanning Gecko-33-OTS). This was achieved by using a SMF-28 fibre circulator (Thorlabs, 6015-3-APC), to direct a collimated beam onto the PRM. The retro reflection from the PRM exited port 3 of the circulator and were sent to the OSA, where spectra were recorded with a 100 ms integration time over each spectral bin at an OSA resolution setting of 0.05 nm. The PRM was driven by a signal generator resulting in a 3.66 kHz pulse train with 230 ns full width at half-maximum (FWHM) pulse lengths.

To minimize the effect of mechanical jitter in the PRM, the AOTF driving signal was synchronised with the rotating mirror to pick out the same wavelength component on each sweep. The photodiode (PD) in Figure 5.4 was used to synchronise the modulation of the AOTF driving signal with the rotation of the PRM. This photodiode detected a 3.66 kHz pulse train from the mirror, and each pulse was used to trigger a triangular waveform from signal generator 1. The triangular pulse was used to sweep the RF output of signal generator 2 which drives the AOTF.

Linewidth measurements were performed at different sweep rates by fixing the sweep duration, defined by the length of the triangular pulses, at 125 µs and adjusting the wavelength span of the sweep by changing the start and stop RF frequency of the sweep. The starting phase of the triangular pulse was adjusted for each sweep rate so that all measurements were taken at the same wavelength.

For sweep rates of 10^6 nm/s and 10^5 nm/s, the central wavelength of a sample was expected to change by ~0.2 nm and ~0.02 nm during the 230 ns FWHM of the pulses sent to the OSA, respectively. Since the resolution setting of the OSA was 0.05 nm, this change was not expected to significantly affect the linewidth measurement at 10^5 nm/s, but could play a role for sweep rates approaching 10^6 nm/s.

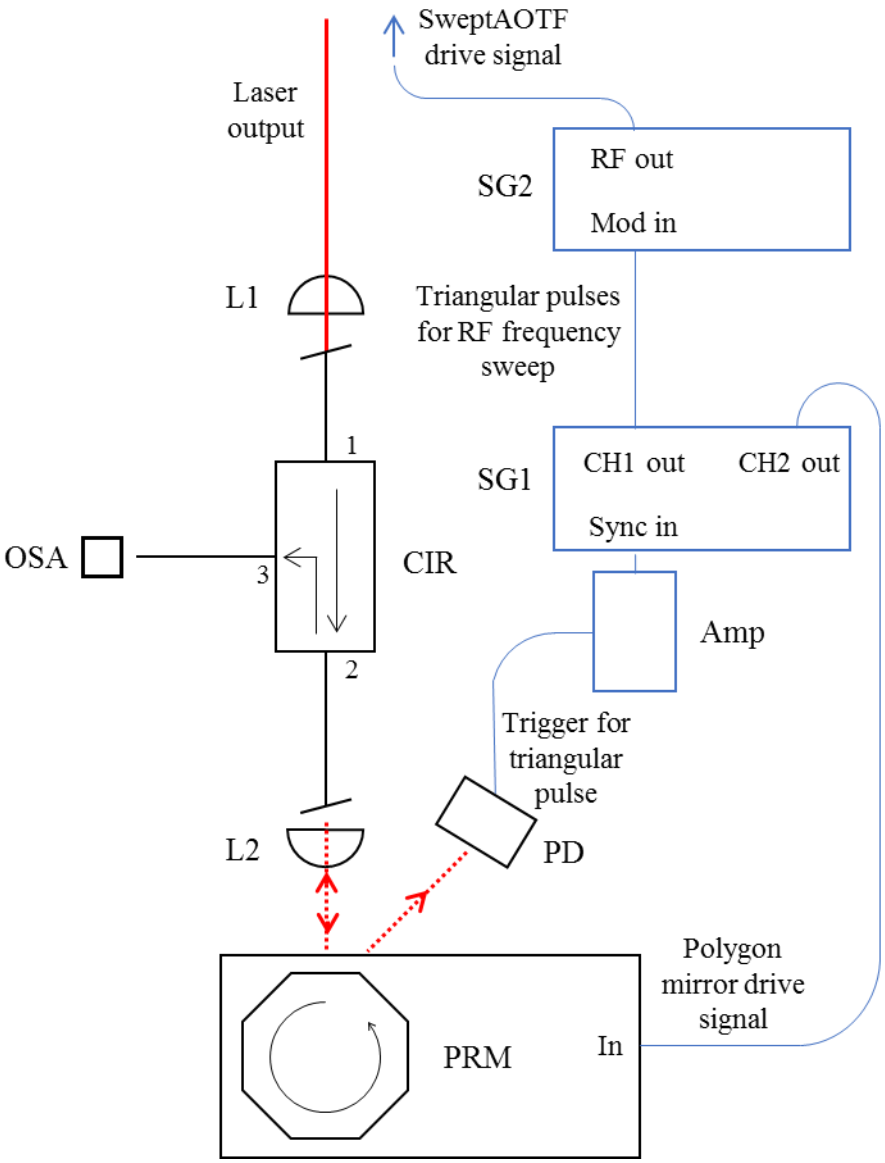

Figure 5.4 Schematic for characterisation of instantaneous linewidth during swept operation of the AOTF tuned SLED standing wave cavity. L1 = 11 mm focal length AR-coated aspheric lens, L2 = 8 mm focal length AR-coated aspheric lens, CIR = optical circulator, SG1 and SG2 = signal generator, Amp = electrical amplifier, PD = photodiode, PRM = polygon rotating mirror, OSA = optical spectrum analyser. Blue = electronics, black = optics, red = laser light.

A typical trace of the PD trigger pulses, the resulting triangular pulses, and the optical pulses sent to the OSA are shown in Figure 5.5 for a 1.28 kHz pulse train and a 714 µs triangular pulse length.

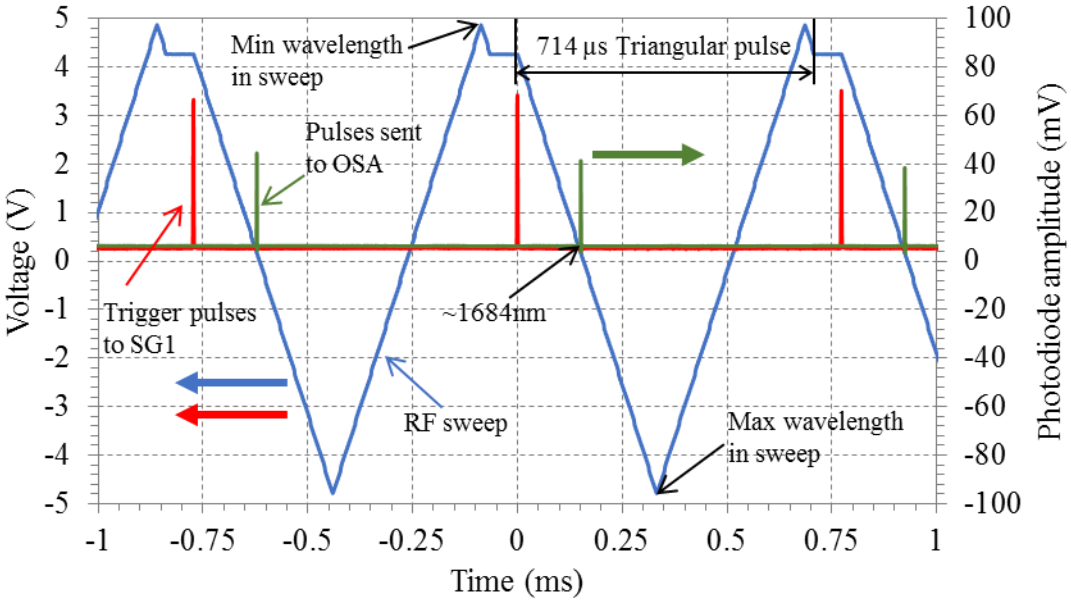

Figure 5.5 Oscilloscope trace of trigger pulses, sweep waveform, and pulses to sent to the OSA.

5.2.3 Results

5.2.3.1 Steady-state operation

The laser tuning curve and output power for 500 mA drive current is shown in Figure 5.6. The AOTF's tuning curve from Figure 4.10 is also overlaid for comparison; the discrepancy between the two curves is attributed to a difference in the angular alignment of the incoming beams.

The laser operated with a maximum power of ~25 mW at ~1720 nm and a 3 dB tuning bandwidth of ~160 nm. This tuning range is consistent with the measured SLED 3 dB bandwidth of ~140 nm shown in Figure 3.11.

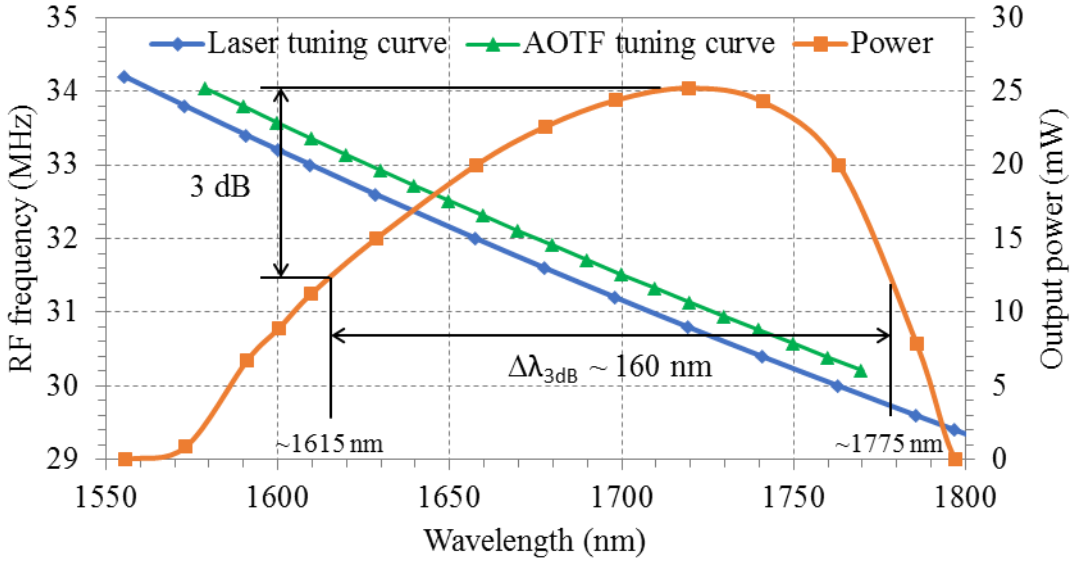

Figure 5.6 Steady-state laser tuning curve and output power.

The output laser power vs SLED injection current at 1720 nm and 1610 nm is shown in Figure 5.7. At 1720 nm and 1610 nm, the laser operated with efficiencies of 0.066 mW/mA and 0.052 mW/mA and threshold currents of 100 mA and 275 mA, respectively.

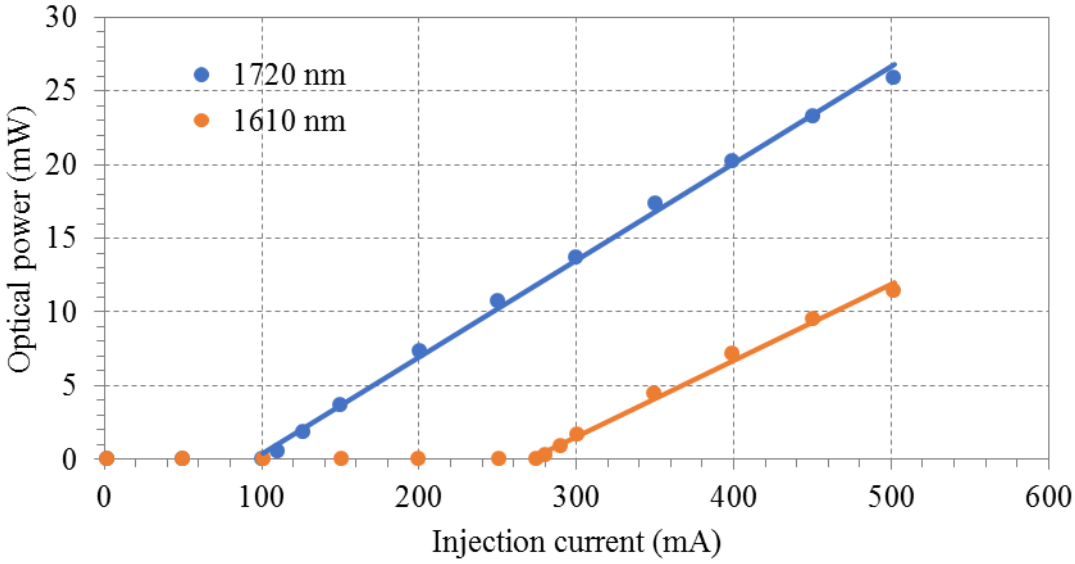

Figure 5.7 Measurement of laser operating powers at 1720 nm and 1610 nm.

The laser spectrum for various wavelengths at 500 mA drive current is shown in Figure 5.8. OSNR ≥70 dB were measured from ~1660 – 1720 nm.

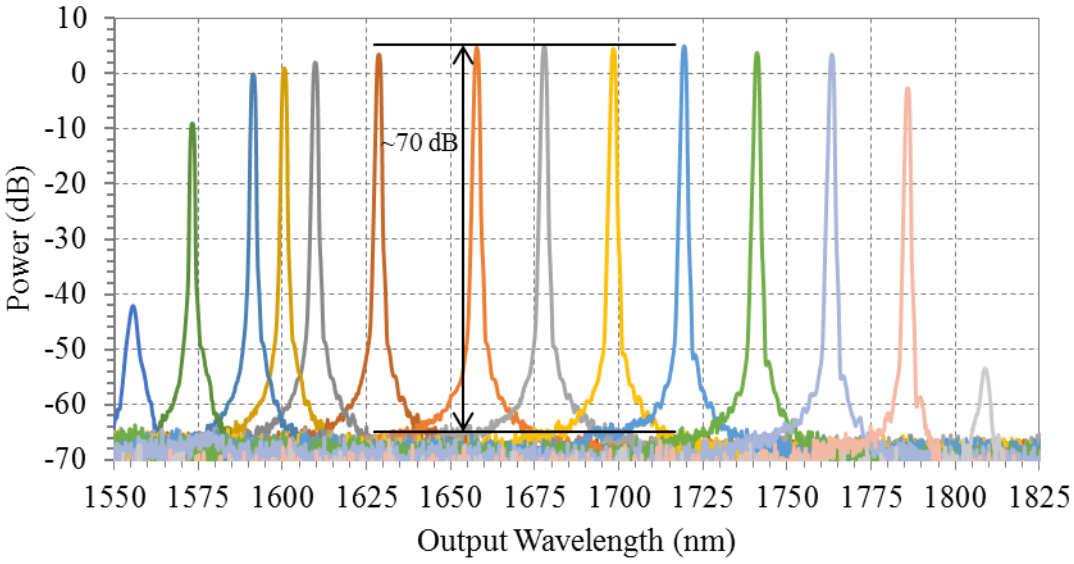

Figure 5.8 Laser spectra at various operating wavelengths. An OSA resolution setting of 2 nm was used.

A higher resolution measurement of the laser spectrum is shown in Figure 5.9. A side-lobe is present ~0.2 nm from the peak wavelength. When tuning to shorter wavelengths the main peak would reduce while the side-lobe increased, until the side-lobe had more power than the longer wavelength peak.

This spectral structure was present across the entire laser spectrum. Tuning to optimise power in each mode revealed a ~0.3 nm separation between adjacent modes, corresponding to the 31.6 GHz FSR of the SLED described in Section 3.3.1.1.

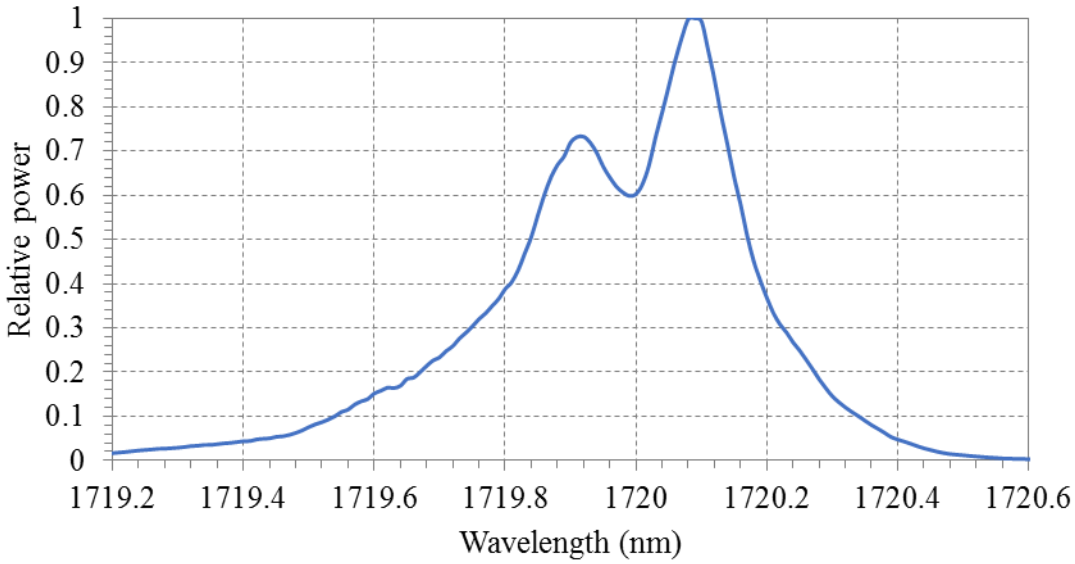

Figure 5.9 Laser spectra measured relative to the peak power. An OSA resolution setting of 0.05 nm was used.

5.2.3.2 Wavelength swept operation

Instantaneous linewidth results for up-sweeping and down-sweeping at sweep rates from 8.00×10^4 nm/s to 8.08×10^5 nm/s are shown in Figure 5.10(a) and (b), respectively. Significant broadening was observed at sweep rates exceeding 8.00×10^4 nm/s for up-sweeping in wavelength and 2.36×10^5 nm/s for down-sweeping. Multiple side-lobes were also apparent above these sweep rates, with a ~0.3 nm separation between side-lobes for the fastest sweep rates. Significant decrease in laser power occurred for sweep rates above 10^5 nm/s.

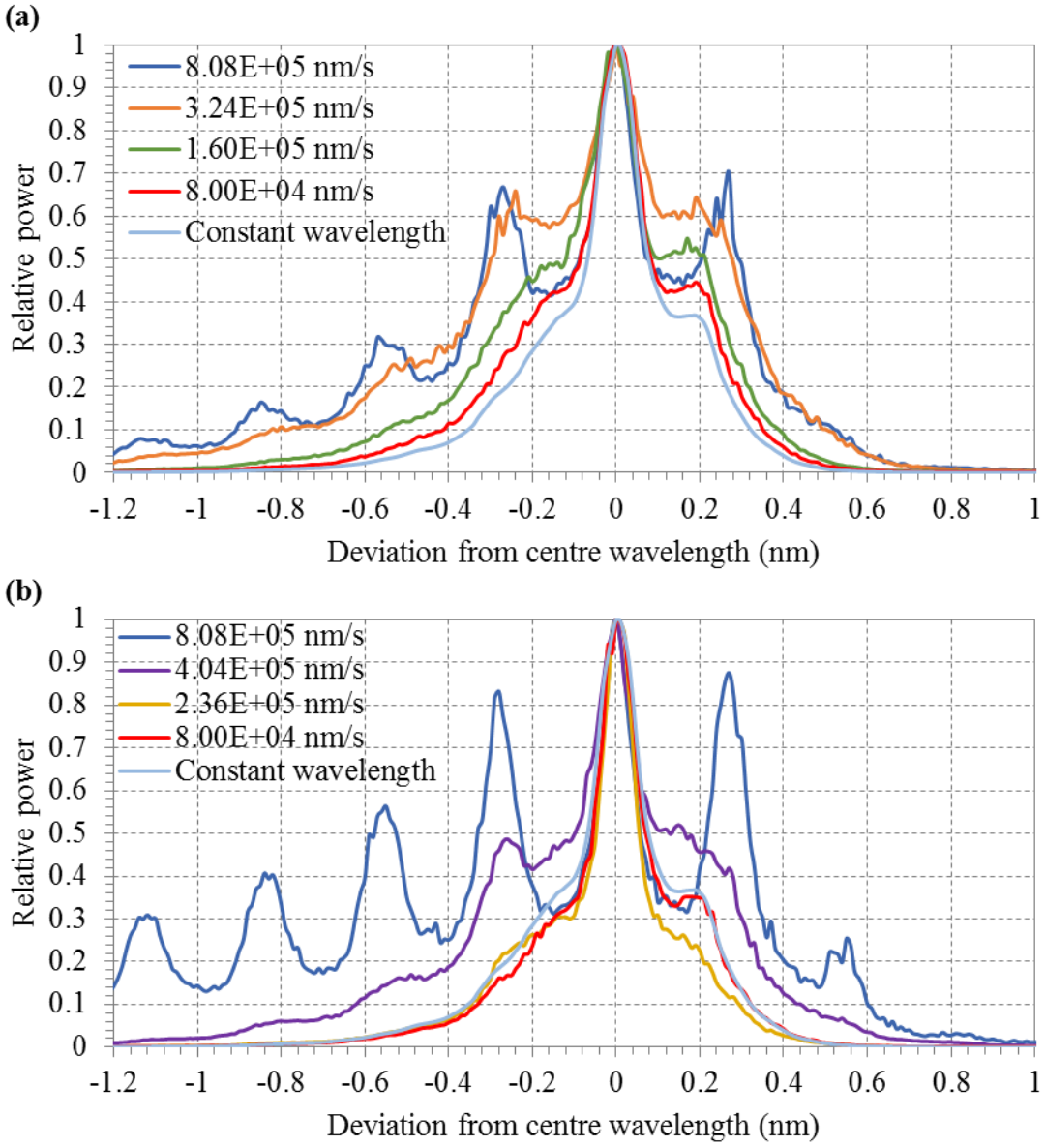

Figure 5.10 Instantaneous linewidth measurements when (a) up-sweeping in wavelength and (b) down-sweeping in wavelength at various sweep rates. The peak wavelength is centred at ~1684 nm. A 100 ms integration time over each spectral bin was used at an OSA resolution setting of 0.05 nm.

5.2.3.3 Wavelength agile operation

The temporal output for discretely switching between two wavelengths is shown in Figure 5.11. The laser was initially operated at an AOTF drive frequency of 32.32 MHz before switching to 31.32 MHz. This corresponded to the laser wavelength switching from 1658 nm to 1709 nm.

No change in laser output power was observed within the first 8 µs after applying the switch. Over the next 21 µs, power decreased for ~13 µs down to ~15% of the initial power before increasing for ~8 µs to reach steady state operation at 1709 nm.

The temporal signal in Figure 5.11 also shows that no self-pulsing was observed during laser operation.

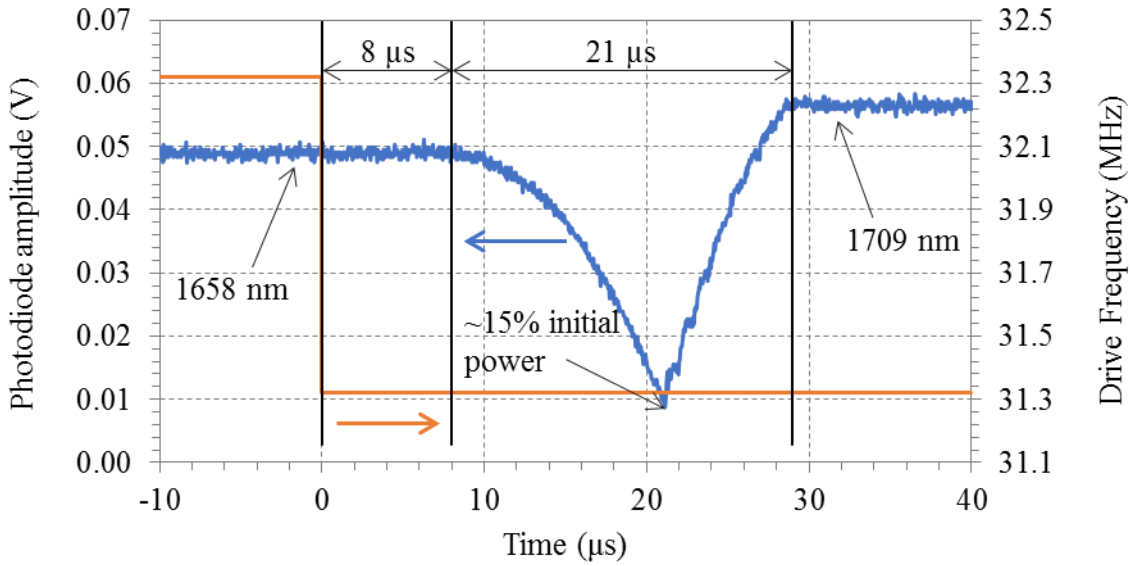

Figure 5.11 Transient output when discretely switching from 1658 nm to 1709 nm. Time t = 0 corresponds to a change in the AOTF drive frequency.

The laser output when sweeping between these two wavelengths is shown in Figure 5.12. Here, the AOTF frequency was ramped over a 125 µs period from 32.32 MHz to 31.32 MHz. The measured total response time was ~150 µs.

For comparison, the laser response to the discrete switch in Figure 5.11 is overlaid in Figure 5.12. There was less power modulation with the slower, swept switching

method, with power dropping to only ~65% of the initial power compared to ~15% for discrete switching.

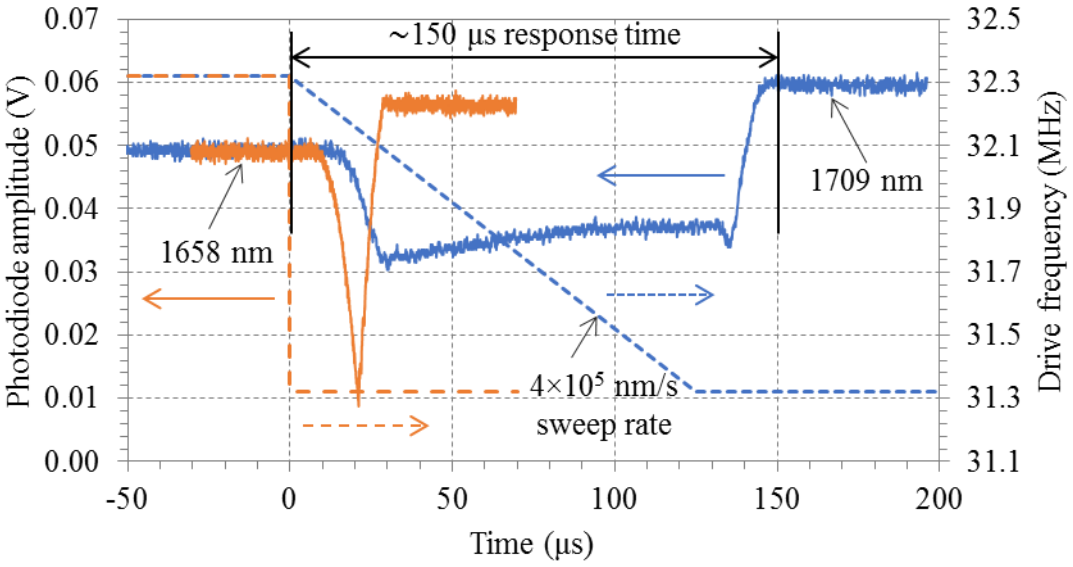

Figure 5.12 Comparison of laser power when switching between two wavelengths by ramping in the AOTF drive frequency, and discretely switching drive frequencies as in Figure 5.11. Blue = ramp switching, orange = discrete switching.

5.2.4 Discussion

A QC-AOTF tuned SLED source was characterised during steady state, wavelength swept, and wavelength agile operation. During steady state operation, the laser demonstrated ≥10 mW between 1615 nm and 1775 nm, in agreement with the SLED's 3 dB bandwidth. The OSNR of ≥70 dB is a consequence of the high out-of-band rejection of the AOTF. The large OSNR is useful for further amplification with fibres where noise from the source needs to be kept at a minimum.

The laser showed a tendency to operate on modes separated by ~0.3 nm. This separation matches that from the SLED's spectral ripple in Figure 3.12, which was attributed to the free spectral range (FSR) of the SLED gain chip. This suggests that the residual feedback between the facets of the chip for this external cavity is too large in comparison to the discrimination offered by the AOTF used in these experiments, which is consistent with the AOTF optical bandwidth of 2.4 nm reported in Section 4.6. Similar effects have been observed in other AOTF tuned semiconductor lasers, where

laser oscillation was restricted to wavelengths corresponding to diode longitudinal modes [12].

The ability to sweep the operating wavelength at rates of 10^4 nm/s for up-sweeping and 2.36×10^5 nm/s for down-sweeping without significant spectral broadening or drop in power is comparable to that in other single QC-AOTF tuned semiconductor lasers. Previously, sweep rates up to 10^4 nm/s were reported for lasers in a fibre coupled QC-AOTF configuration with instantaneous linewidths <0.05 nm across the 800 – 1100 nm region [13,98,102,107]. For faster sweep rates, non-collinear AOTFs can be used due to their faster switching times at the expense of lower spectral resolution. Rates of 10^6 nm/s have been demonstrated with 0.45 nm instantaneous linewidths [103].

The wavelength agile performance was investigated with two wavelength switching methods, using discrete and linear transition waveforms. For discrete switching, the 8 µs latency and 21 µs transition time corresponds to the 8 µs delay and 21 µs acousto-optic (AO) interaction time measured in the temporal characterisation of the AOTF in Section 4.5.4. During this transition period, the power at the initial wavelength drops due to the decreasing interaction time with acoustic wave at the initial frequency. Eventually a threshold point is reached where the interaction time is insufficient to provide the required diffraction efficiency for lasing. Lasing at the final wavelength will occur at a threshold interaction time for the acoustic wave at that frequency. Power at this wavelength will then increase until the quasi-collinear interaction region of the AOTF consists only of the latter acoustic frequency. Together this results in the modulation in output power observed when switching, where transitioning from 1658 nm to 1709 nm resulted in the power dropping to 15% of the initial power.

For the linear transition ramp method of switching from λ_1 to λ_2, smaller modulations in power are achievable while still maintaining fast switching times of ~150 µs. Avoiding significant power modulation is desirable when the wavelength agile source is to be used as a master oscillator for further amplification.

While the source developed in this section can sweep at rates up to 10^5 nm/s for down-sweeping, and switch between any two wavelengths in the tuning range within

29 µs, the effect of residual feedback between the facets of the chip on the output spectrum is unwanted, and therefore an alternate cavity design is desirable.

5.3 AOTF tuned semiconductor optical amplifier ring-cavity

The etalon effect in the SLED based, AOTF tuned, standing wave laser spectrum might be reduced by using alternate semiconductor designs that exhibit smaller spectral modulation in their ASE. In this section, the SLED is replaced by a semiconductor optical amplifier (SOA), which exhibit smaller spectral modulation due to AR coatings on both semiconductor facets. The SOA is first characterised before being incorporated in an AOTF tuned ring-cavity laser. The laser is then characterised in a similar manner to the SLED cavity in Section 5.2.2.

5.3.1 Semiconductor optical amplifier selection

A schematic of the selected SOA (Thorlabs, BOA1082P) is shown in Figure 5.13. It consists of a fibre-coupled SOA housed within in a butterfly package, and is controlled using a Thorlabs CLD1015 butterfly LD/TEC controller.

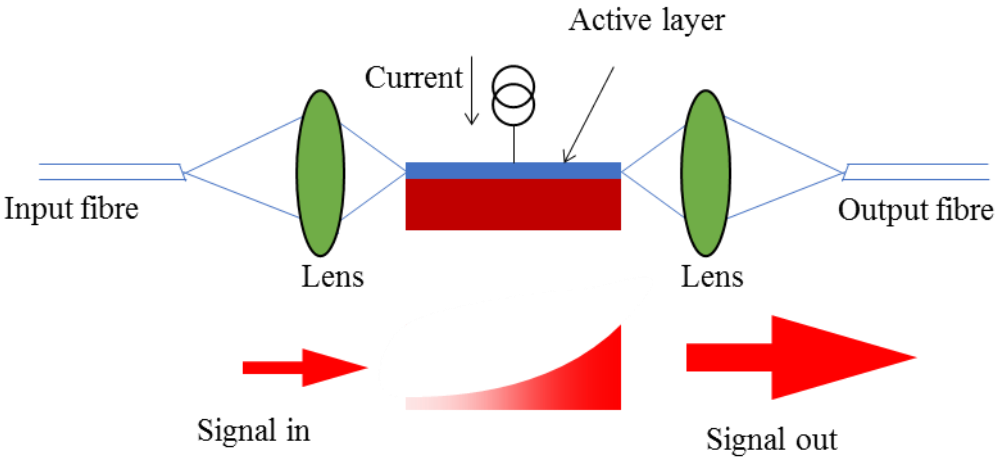

Figure 5.13 Layout of the semiconductor optical amplifier [113].

5.3.2 Semiconductor optical amplifier characterisation

The setup used for characterising the SOA is shown in Figure 5.14. The power and spectrum of the light exiting the input and output ports were measured using a

calibrated photodiode power meter (Thorlabs, S155C) and an OSA (Yokagawa, AQ6375).

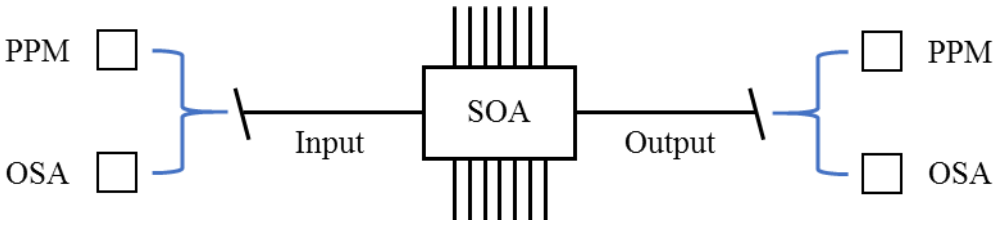

Figure 5.14 Setup for characterising SOA gain medium. PPM = photodiode power meter, OSA = optical spectrum analyser.

The power exiting the input and output ports for drive currents up to 600 mA is shown in Figure 5.15. The power exiting both ports was similar, as expected, differing only by ~10 µW at 600 mA.

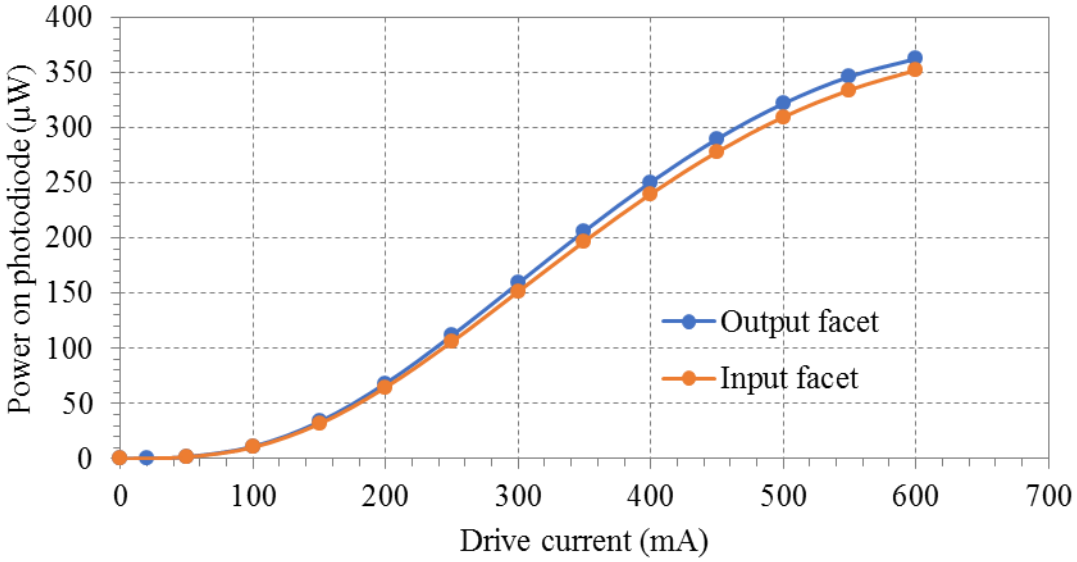

Figure 5.15 Power exiting the output and input port of the SOA at various drive currents.

The ASE spectra of the outputs for various drive currents are shown in Figure 5.16. There was no significant difference between the spectra for the input and output ports. At 600 mA, the spectrum peaks around ~1663 nm with a 3 dB bandwidth of ~137 nm. As the current was decreased from 600 mA the gain peak shifted to longer wavelengths, reaching ~1730 nm at 50 mA with a 3 dB bandwidth of ~65 nm.

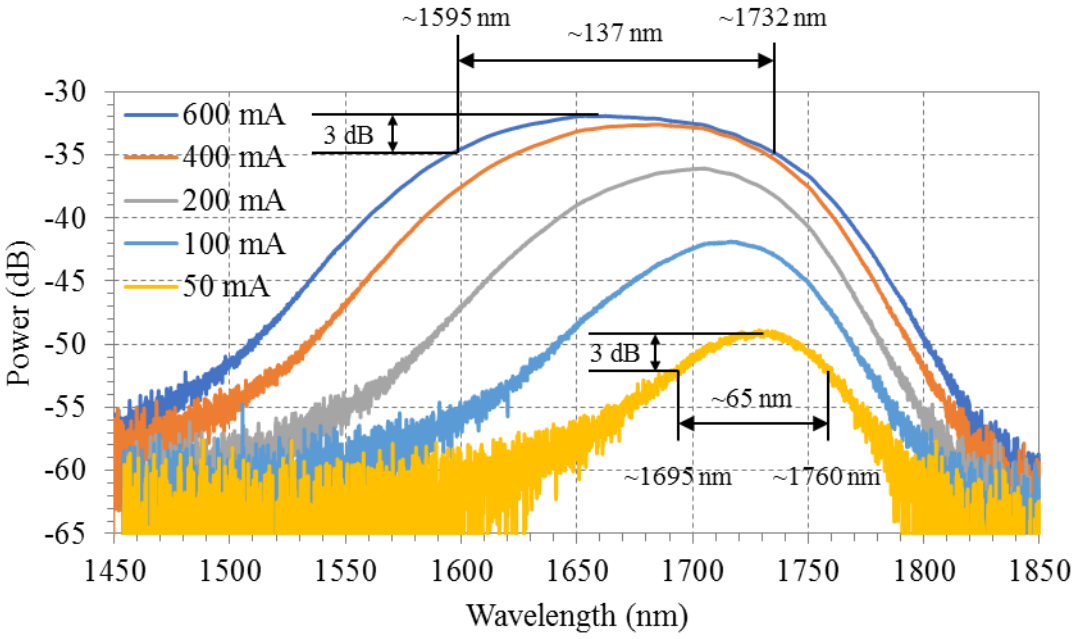

Figure 5.16 ASE spectra of the SOA outputs for various drive currents. An OSA resolution setting of 2 nm was used.

A high resolution spectrum of the ASE at 600 mA, centred around 1653 nm, is shown in Figure 5.17. Both slowly and rapidly varying modulations in the spectrum were observed. The rapidly varying component has a ~0.01 dB modulation with a ~0.3 nm separation between peaks.

The 0.3 nm separation between peaks matches what was observed in the SLED, and can be attributed to the free spectral range (FSR) of the semiconductor chip. The 0.01 dB modulation, however, is much smaller than the 1.5 dB observed in the SLED. This indicates the etalon effects observed in the SLED tunable laser cavity should be greatly reduced by using a SOA gain medium. The SOA should also have a broad tuning range, given that its 137 nm, 3 dB bandwidth at 600 mA is similar to the 140 nm bandwidth of the SLED at 500 mA.

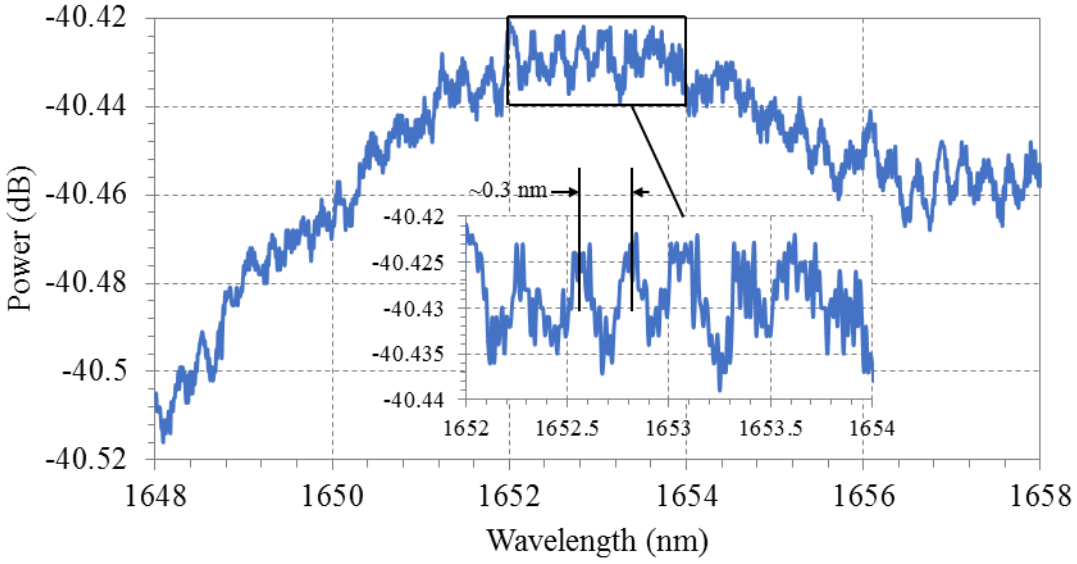

Figure 5.17 High resolution spectrum of ASE exiting the output port of the SOA at 600 mA drive current. A resolution setting of 0.05 nm was used.

5.3.3 Cavity design

The cavity design for the AOTF tuned SOA laser is shown in Figure 5.18. A ring-cavity was formed using a polarisation maintaining (PM) circulator (Thorlabs, CIR 1550PM-APC) and a 50/50 PM output coupler (Thorlabs, PN1550R5A2). Light from the output port of the SOA was launched into port 1 of the circulator and exited port 2, where it was collimated with an 8 mm focal length, AR-coated aspheric lens (Thorlabs C240TME-C). The collimated beam was directed onto the AOTF and had an ordinary incident polarisation. The diffracted light was retro-reflected back to port 2 of the circulator by a HR mirror, where it then exited port 3. This light was then coupled to a 50/50 PM coupler, where 50% of the light was outcoupled and the other 50% fed back to the OSA input port to complete the cavity. The double pass of the AOTF per round trip in the ring cavity matched that in the SLED cavity. The ordinary incident polarisation resulted in an upshift in frequency of the diffracted light, as opposed to the downshift for the extraordinary input polarisation used in the SLED standing wave cavity.

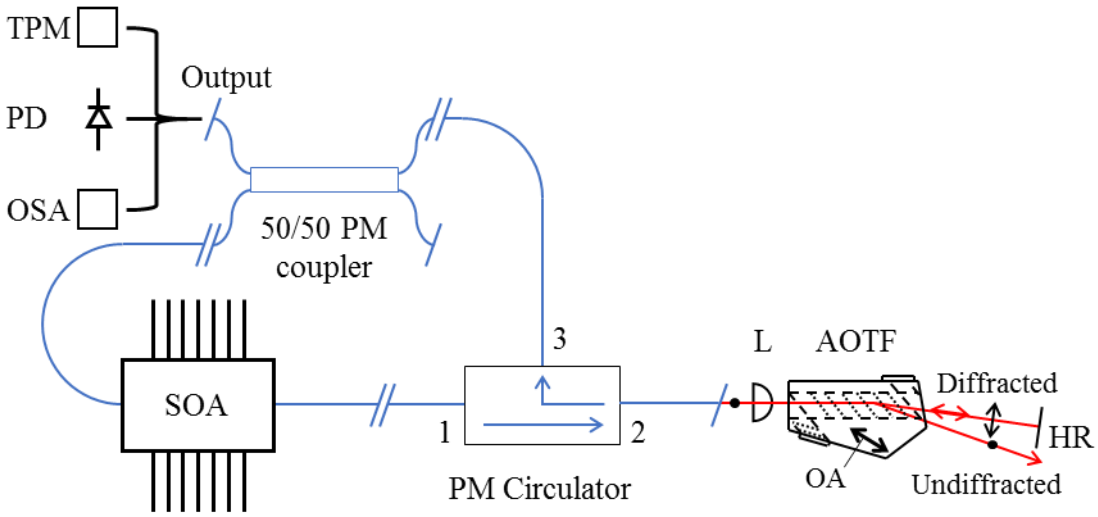

Figure 5.18 AOTF tuned SOA ring-cavity design. TPM = thermal power meter, PD = photodiode, OSA = optical spectrum analyser, PM = polarisation maintaining, SOA = semiconductor optical amplifier, L = 8 mm focal length AR coated aspheric lens, AOTF = acousto-optic tunable filter, HR = highly reflective mirror.

Characterisation of the SOA cavity was performed in a similar manner to the SLED standing wave cavity, with the same thermal power meter, photodiode, and OSA used as diagnostic tools. The current was fixed at 600 mA and the AOTF driven at the same power levels as the SLED cavity. Wavelength agile and wavelength swept operation were achieved with the methods detailed in Section 5.2.2.

The method for measuring instantaneous linewidth when sweeping was slightly altered from that shown in Figure 5.4, and is shown in Figure 5.19. The triggering and synchronisation of the laser were kept the same, however additional optics and photodiodes were added for improved monitoring. This enabled a simultaneous measurement of the relative power at a particular wavelength during the sweep.

The laser output was split before entering an isolator with a 90/10 coupler (Thorlabs, TW1550R2A2), with 90% of the light sent to the PRM for linewidth measurement and the other 10% sent to a photodiode for monitoring the power. The pulses sent to the OSA were from a fibre-coupled off-axis parabolic mirror (Thorlabs, RC04FC-P01), which collected light from the PRM and sent 50% to the OSA for instantaneous linewidth measurement and the other 50% to a photodiode via a 50/50 coupler (AFW, FOBC-2-15-50-L-1-S-2). The pulses detected on this photodiode were used as a

reference so the timing of the pulses to the OSA could be monitored relative to the trigger pulses. The duration of the pulses sliced from the output and sent to the OSA were observed to be ~160 ns, which differed from the ~230 ns pulses from instantaneous wavelength measurements in Section 5.2.2 for the SLED cavity.

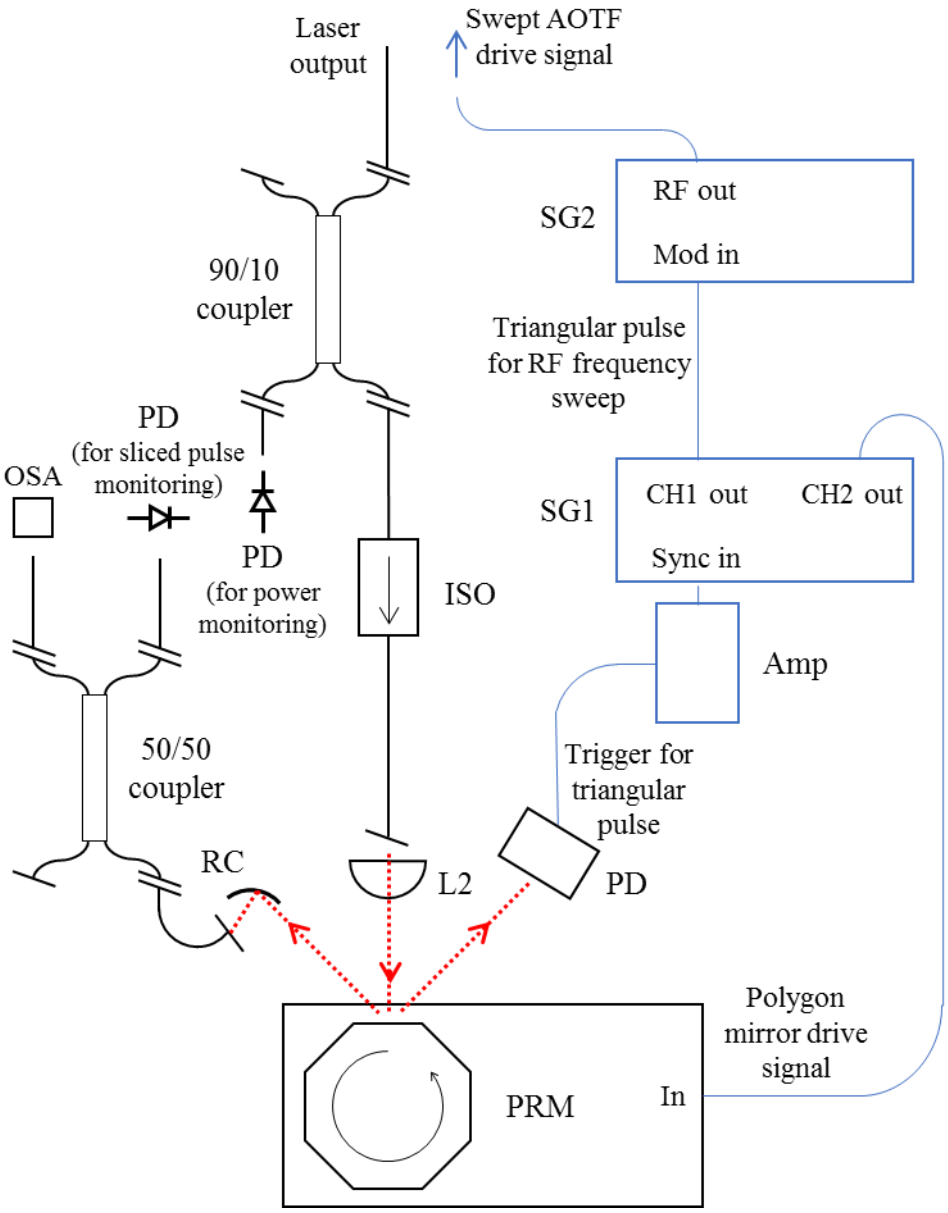

Figure 5.19 Schematic for characterisation of instantaneous linewidth during swept operation of the AOTF tuned SOA ring-cavity. L1 = 11 mm focal length AR-coated aspheric lens, L2 = 8 mm focal length AR-coated aspheric lens, CIR = optical circulator, SG1 and SG2 = signal generator, Amp = electrical amplifier, PD = photodiode, PRM = polygon rotating mirror, Blue = electronics, black = optics, red = laser light.

5.3.4 Results

5.3.4.1 Steady-state operation

The laser power and spectrum as a function of wavelength are shown in Figure 5.20 and Figure 5.21, respectively. The AOTF was driven at an optimum level of 180 mW to maximise the output power. The laser power peaks at ~10 mW from 1665 – 1685 nm and has a 50 nm, 3 dB tuning range from 1600 – 1750 nm. Figure 5.21 shows there is high OSNR of >75 dB across the 3 dB tuning range.

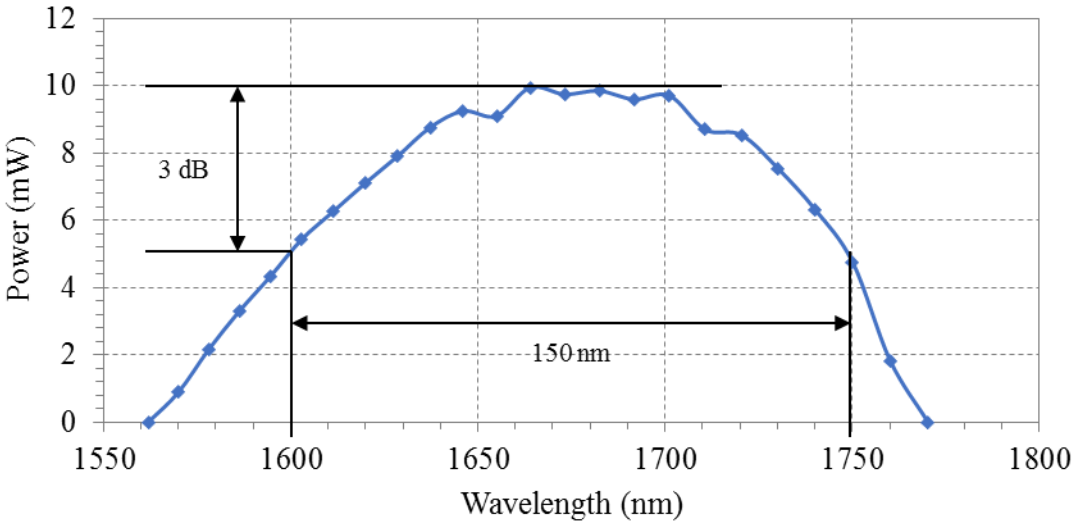

Figure 5.20 Output power across wavelength operating region of the laser.

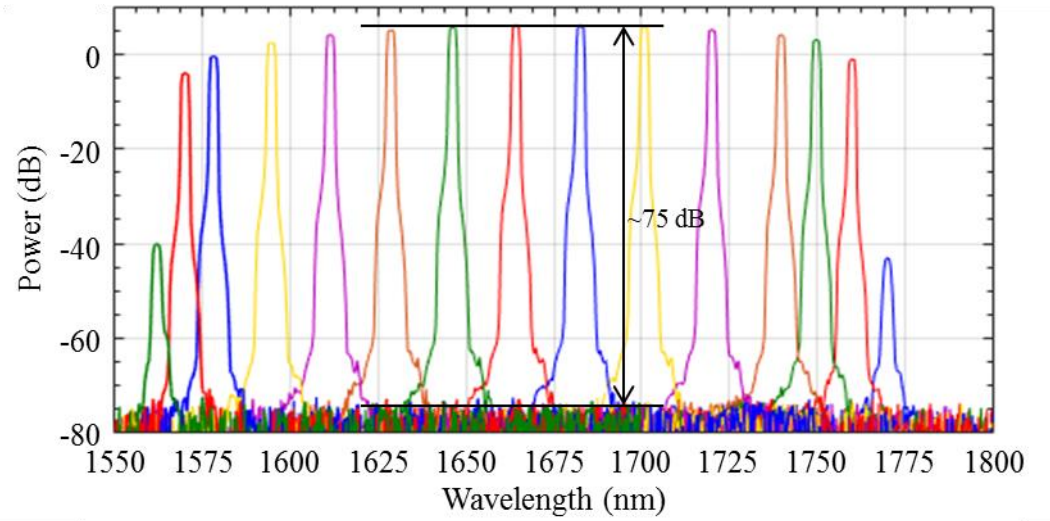

Figure 5.21 Broad output spectra on OSA at various wavelengths. An OSA resolution setting of 2 nm was used.

OSA scans of the laser at 600 mA and 200 mA injection currents when slowly swept in wavelength are shown in Figure 5.22. Also included for comparison are the ASE spectra at 600 mA and 200 mA from Figure 5.16, vertically shifted to align with the corresponding laser spectra at the same currents.

At 600 mA and 200 mA, lasing occurred from ~1565 – 1765 nm and 1640 – 1745 nm, respectively, and the laser spectra corresponded well with the shifted ASE spectra.

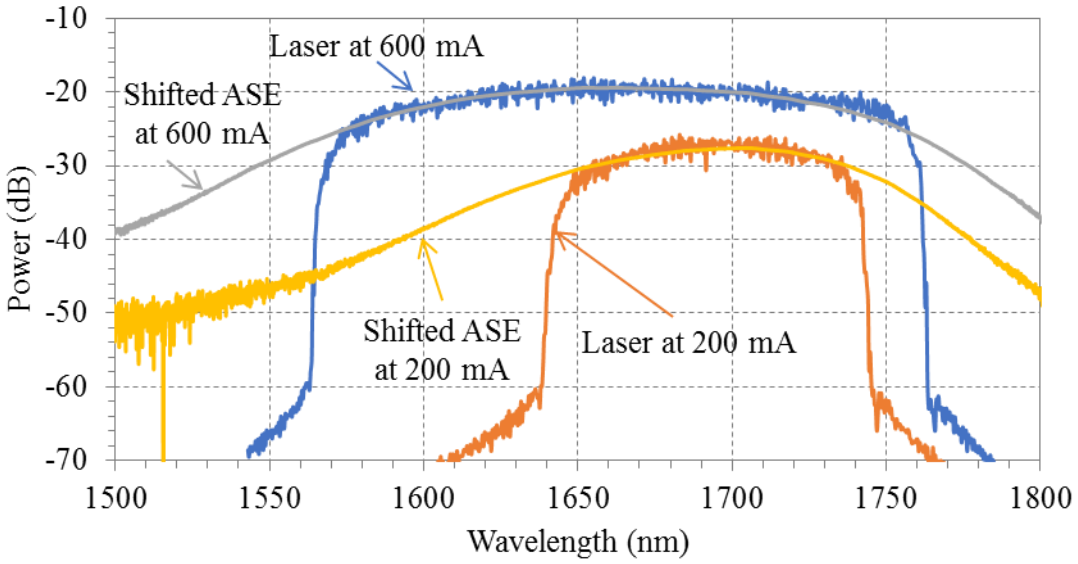

Figure 5.22 OSA long hold scans of laser when slowly swept at 600 mA and 200 mA. An OSA resolution setting of 0.5 nm was used. Also included are vertically shifted ASE spectra at the same injection currents.

The laser power as a function of SOA injection current at 1637, 1668, 1720, and 1751 nm is shown in Figure 5.23. The efficiencies at 1637 nm and 1668 nm were larger than at 1720 nm and 1751 nm, with the highest powers achievable at 1668 nm. The lowest threshold was 120 mA for 1720 nm, which agrees with the results from Figure 5.16 which showed more ASE occurring at longer wavelengths for small injection currents

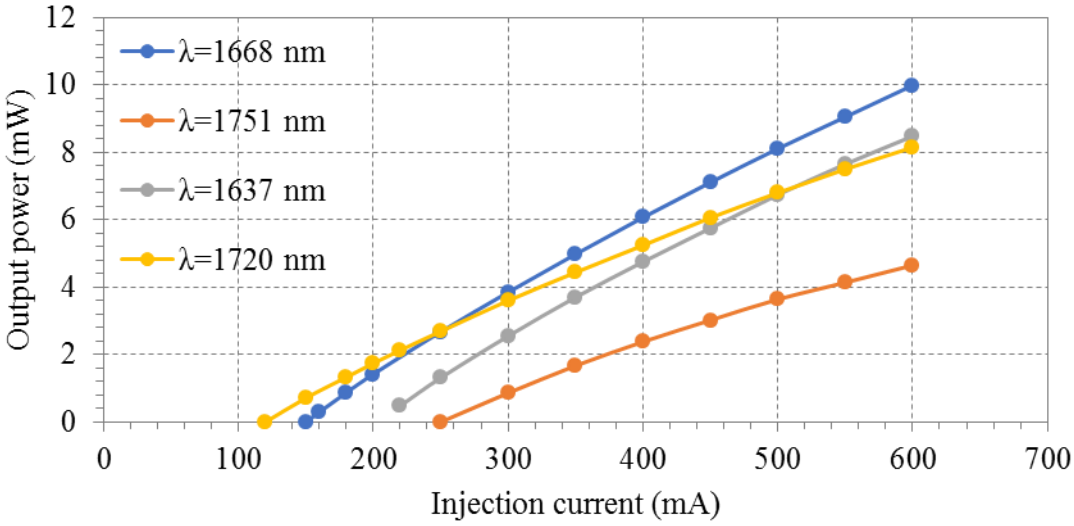

Figure 5.23 Laser power for different SOA injection currents at various operating wavelengths. AOTF driven at 3.0 V_{rms} corresponding to 180 mW average power.

High resolution spectra of the laser operating at ~1668 nm for various injection currents are shown in Figure 5.24. No side-lobes were measured across the full range of injection currents. ~0.3 nm linewidths were observed at currents from 300 – 600 mA. Below this, there was a noticeable decrease in linewidth, reaching ~0.2 nm at currents ≤200 mA.

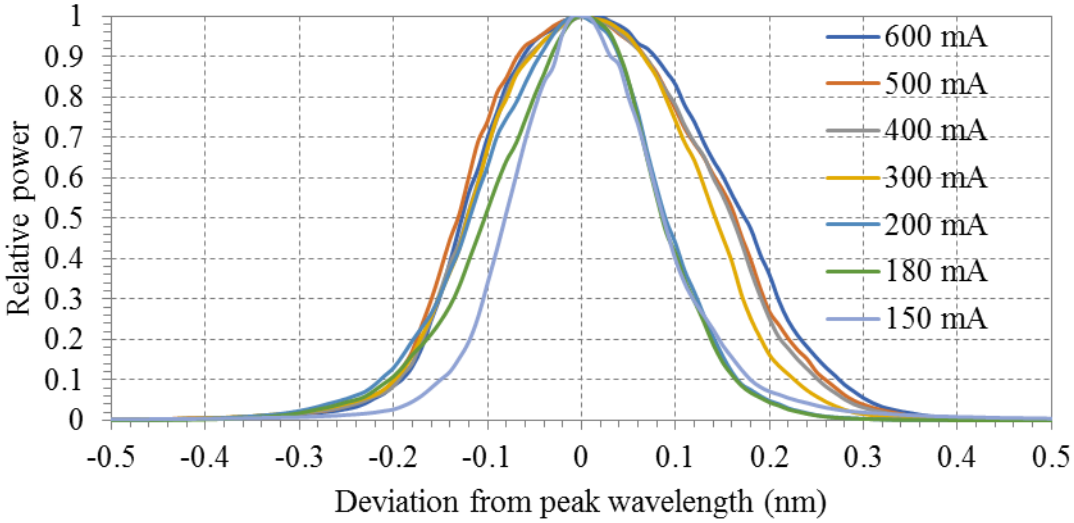

Figure 5.24 High resolution OSA scans of laser spectra at various injection currents for a central wavelength of 1668 nm. Power is measured relative to the peak power of each scan. An OSA resolution setting of 0.05 nm was used.

The output spectra at closely spaced operating wavelengths around 1637 nm are shown in Figure 5.25. There was minimal change in both spectral shape and power across all wavelengths, and no side-lobes were observed.

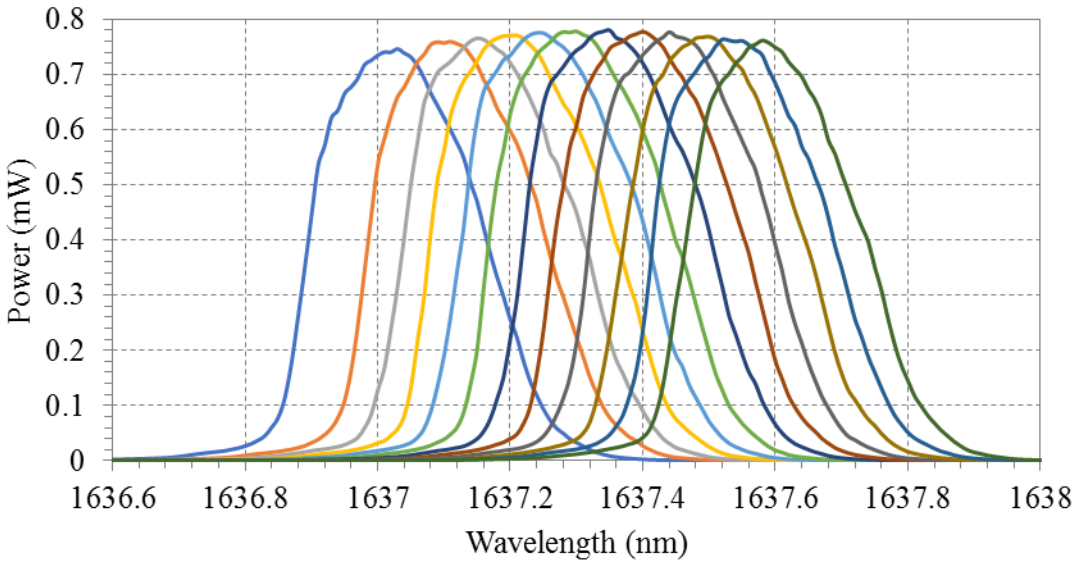

Figure 5.25 Laser spectra at closely spaced wavelengths. An OSA resolution setting of 0.05 nm was used.

5.3.4.2 Wavelength swept operation

The instantaneous linewidth results for both up-sweeping and down-sweeping in wavelength are shown in Figure 5.26(a) and (b) respectively. The laser significantly broadened for both up and down-sweeping at 3.5×10^5 nm/s, and skewed towards shorter wavelengths.

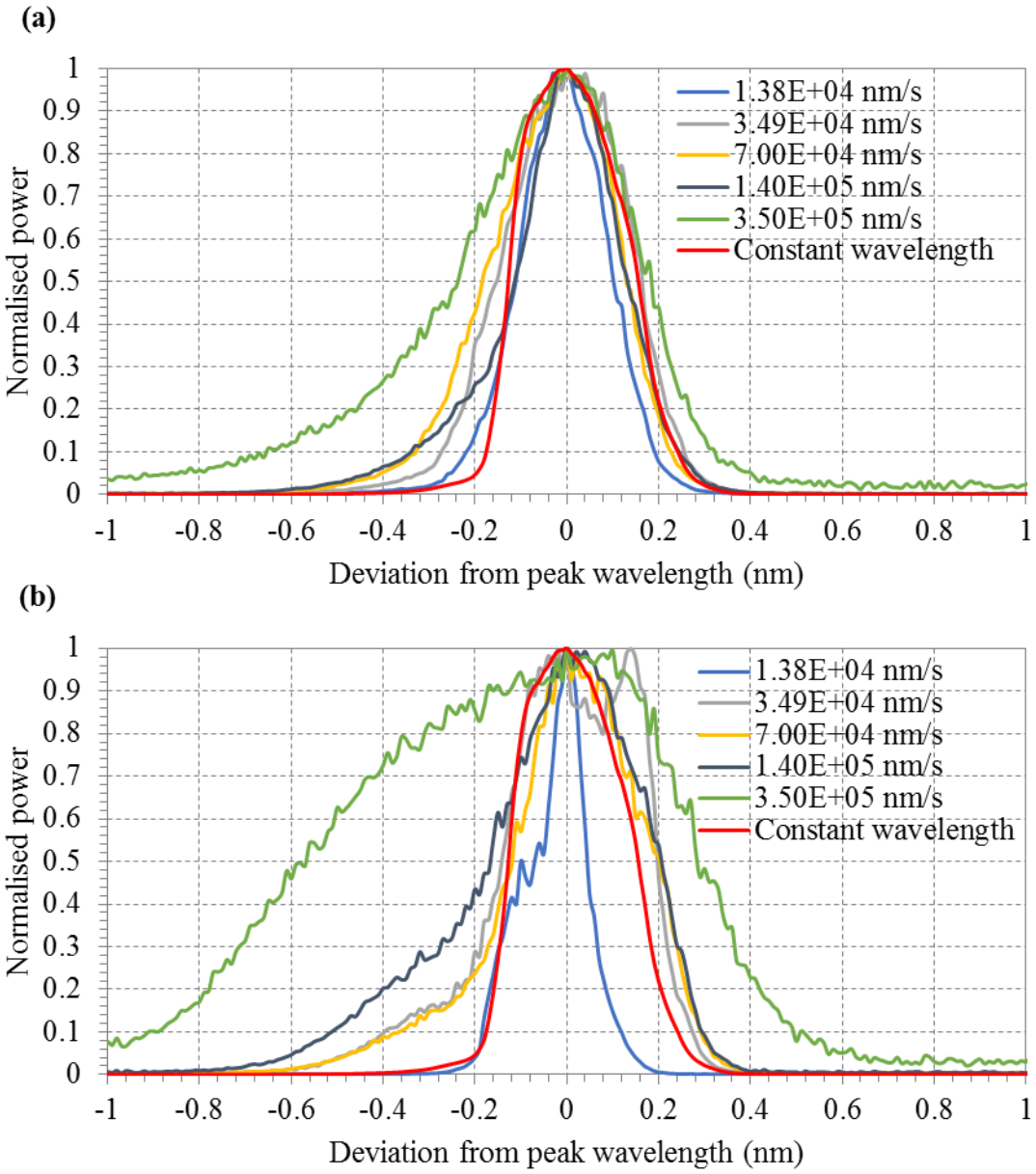

Figure 5.26 Instantaneous linewidth measurements when (a) up-sweeping in wavelength and (b) down-sweeping in wavelength, at various sweep rates. Power is measured relative to the peak power of each scan. The peak wavelength is centred at 1637 nm. A 20 ms integration time over each spectral bin was used at an OSA resolution setting of 0.05 nm.

The 3 dB linewidth vs sweep rate for both up and down-sweeping is shown in Figure 5.27. There is a distinct reduction in linewidth for down-sweeping at rates of 1.38×10^4 nm/s, reaching ~0.1 nm. As the sweep rate, there is more broadening for down-sweeping, and up-sweeping eventually yields the narrower linewidth.

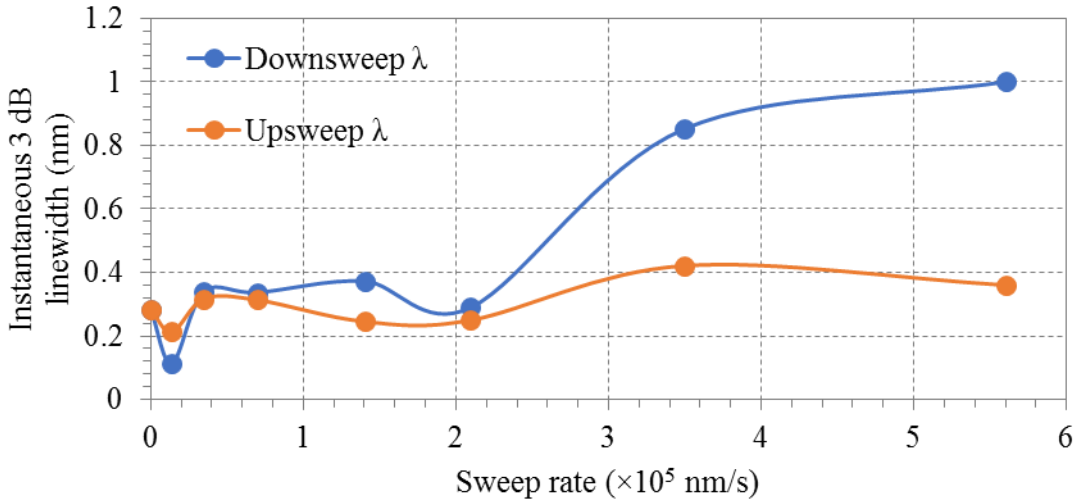

Figure 5.27 Instantaneous 3 dB linewidth vs sweep rate for both down and up-sweeping, centred over ~1637 nm with a 600 mA injection current.

The relative power at each sweep rate is shown in Figure 5.28. Up-sweeping provides more laser power than down-sweeping at sweep rates up to 1.4×10^5 nm/s. There is more power when up-sweeping at these rates than when the laser is in a CW, un-swept regime. Beyond these sweep rates, the power begins to drop significantly, and by the time it reaches 3.5×10^5 nm/s the power is comparable to that of down-sweeping.

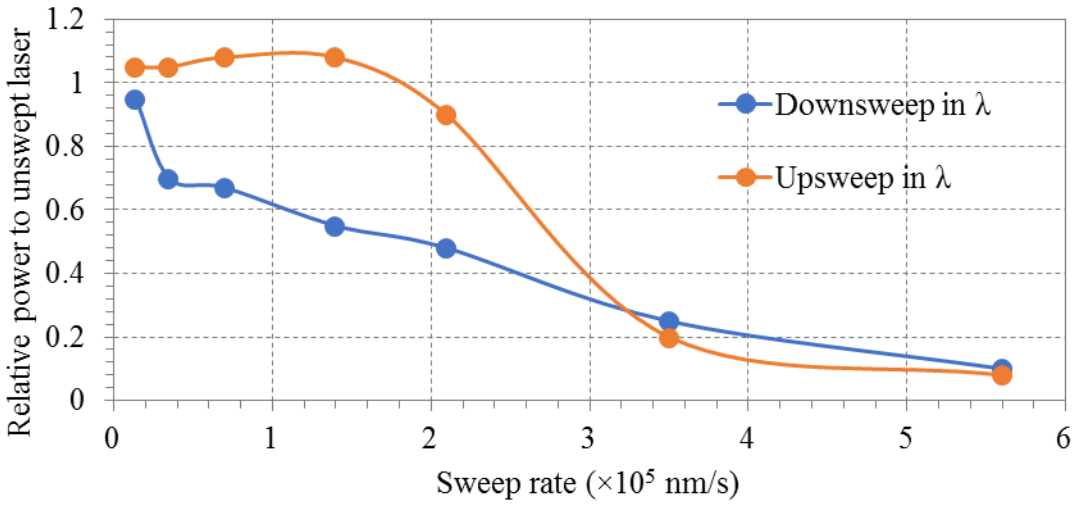

Figure 5.28 Swept laser power relative to CW un-swept laser operation vs sweep rate for both down and up-sweeping, centred over ~1637 nm with a 600 mA injection current.

5.3.4.3 Wavelength agile operation

The temporal response of the laser was investigated for a discrete wavelength switch, and gave the same latency and interaction times as the SLED cavity, resulting in a 29 µs total switch time between wavelengths.

5.3.5 Discussion

A QC-AOTF tuned SOA ring-cavity was characterised in steady state, wavelength swept, and wavelength agile operation. During steady state operation, the laser operated with 10 mW of maximum power at ~1665 – 1685 nm, with a 155 nm 3 dB tuning bandwidth from 1595 – 1750 nm, as expected from the 137 nm ASE bandwidth of the SOA. The OSNR across this tuning range was >75 dB, as expected from the high OSNR observed in the SLED standing wave cavity. The laser linewidth was ~0.3 nm for injection currents of 300 – 600 mA, and ~0.2 nm for currents <200 mA. Side-lobes were not observed across the tuning range and there was no evidence of etalon effects leading to preferred operating wavelengths. This is attributed to the small spectral modulation of the SOA.

For wavelength agile operation, the 29 µs switch time when discretely switching between wavelengths was the same as that for the standing wave SLED cavity. This is because the switch time is determined by the acoustic travel time within the AOTF, which was the same for both cavities.

During wavelength swept operation, no side-lobes were present, and instantaneous linewidths of ~0.2 – 0.4 nm were observed up to sweep rates of 2×10^5 nm/s, after which significant broadening occurred. At the slower sweep rate of 1.38×10^4 nm/s for down-sweeping, the linewidth was significantly smaller than that for the un-swept laser. This could be explained by considering the change in frequency of the AOTF filter peak per cavity round trip to the shift in wavelength of light per round trip due to AO interaction with the AOTF. In the example shown in Figure 5.29, light is initially centred over the AOTF filter peak, and after a cavity round trip the change in frequency of the peak closely matches the shift in the frequency of light per round trip. When this occurs, the shifted light will remain under the filter peak, and the laser experiences spectral narrowing [10].

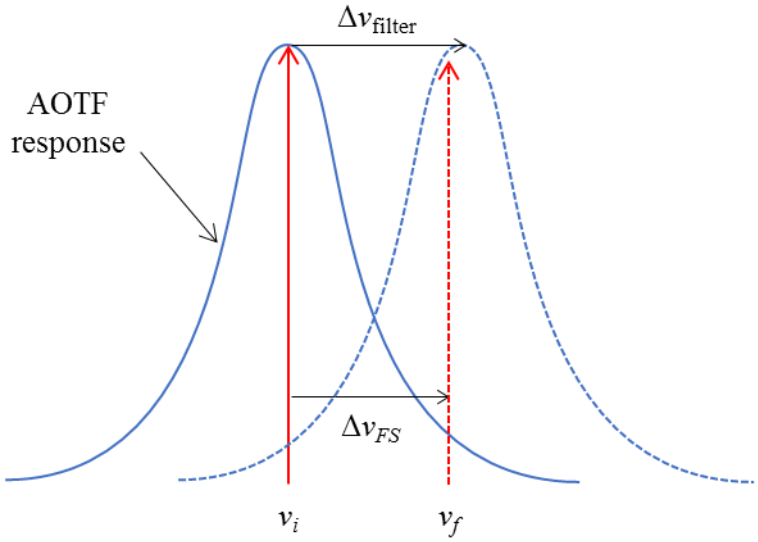

Figure 5.29 Change in filter position per cavity round trip $\Delta\nu_{\text{filter}}$ when closely matching the change in optical frequency per round trip $\Delta\nu_{FS}$, for light initially centred over the AOTF filter peak. ν_i = initial optical frequency, ν_f = final optical frequency.

Recalling the positive frequency shift due to AO interaction in our ring-cavity, the net frequency shift after one cavity round trip of is

$$\Delta\nu_{\text{FS}} = +2 \times f, \tag{5.1}$$

where f is the driving frequency of the AOTF. During swept operation, the instantaneous linewidths were measured at ~1637 nm, which corresponded to a ~35.5 MHz drive frequency. This gives a net shift of

$$\Delta\nu_{\text{FS}} = +71 \text{ MHz}. \tag{5.2}$$

During swept operation, the change in filter position after one cavity round trip $\Delta\lambda_{\text{filter}}$ is

$$\Delta\lambda_{\text{filter}} = \frac{d\lambda}{dt} \times \tau_{rt}, \tag{5.3}$$

where $d\lambda/dt$ is the sweep rate and τ_{rt} is the cavity round trip time, given by

$$\tau_{rt} = \frac{L_{eff}}{c}, \tag{5.4}$$

where L_{eff} is the effective vacuum cavity length and c is the vacuum speed of light. The ring-cavity consisted of 8.6 m of fibre and ~10 cm of free space, giving

$$L_{eff} = 13 \text{ m}, \quad \textbf{5.5}$$

and

$$\tau_{rt} = 43 \text{ ns}. \quad \textbf{5.6}$$

The sweep rate that corresponded to significant linewidth reduction was

$$\frac{d\lambda}{dt} = -1.38 \times 10^4 \text{ nm/s}. \quad \textbf{5.7}$$

Therefore the change in filter position is

$$\Delta\lambda_{\text{filter}} = -590 \text{ fm}. \quad \textbf{5.8}$$

Using Equation 2.2, this change in wavelength corresponds to a change in optical frequency per cavity round trip $\Delta\nu_{\text{filter}}$ of

$$\Delta\nu_{\text{filter}} = +66 \text{ MHz}. \quad \textbf{5.9}$$

This is close to the $\Delta\nu_{\text{FS}}$ = +71 MHz shift per round trip from AO interaction in Equation 5.2. Therefore, over multiple cavity round trips, the shifted light may remain within the moving filter passband longer than for the un-swept scenario, allowing spectral narrowing of the output.

5.3.6 Comparison

Both the AOTF tuned SOA ring-cavity and SLED standing wave cavity had similar tuning bandwidths during steady state operation. The power in the standing wave cavity was larger and could be attributed to the double pass of the gain medium per cavity round trip. The etalon effects present in the SLED cavity output spectrum were not observed in the SOA ring-cavity. This is attributed to a reduced etalon effect in the SOA output, with the ~0.01 dB modulation associated with the SOA shown in Figure 5.17

being much smaller than the ~1.5 dB present in the SLED output spectrum shown in Figure 3.12.

When sweeping, the SLED cavity could operate at faster sweep rates than the SOA cavity before significant drops in power occurred. There was minimal drop in power for the SLED standing wave cavity at sweep rates up to 2.02×10^5 nm/s in either sweep direction, whereas when the SOA ring-cavity operated at sweep rates of 2.10×10^5 nm/s, the power had dropped by ~5% for up-sweeping and ~50% for down-sweeping. This could be attributed to the SOA ring cavity round trip time being at least an order of magnitude larger than the SLED standing wave cavity. For light initially centred over the AOTF passband, after one round trip the movement of the filter means it will no longer be positioned over the peak and experiences increased loss. For long round trip times the light will no longer be within the transmission region of the filter and consequently output power is reduced.

5.4 Summary

In this chapter multiple QC-AOTF tuned sources were built based on semiconductor gain media. The first used the SLED from Section 3.2 and had a 3 dB tuning range of 160 nm from 1615 – 1775 nm, with 25 mW peak power at 1720 nm. The high rejection ratio of the AOTF allowed OSNRs of ≥65 dB across this tuning range. Discrete switching between any two wavelengths within ~29 µs was possible at the expense of power modulation during the switch. The modulation could be reduced by sweeping the laser when switching wavelengths. Side-lobes were present in the laser spectrum which was attributed to an etalon effect from reflections within the gain medium. To reduce the etalon effect, an SOA gain medium was investigated. It exhibited a significantly reduced spectral modulation than the SLED, due to having AR coatings on both facets. An AOTF tuned ring-cavity was built with the SOA as the gain element. No etalon effects were observed in this source for any mode of operation. The laser had a similar 3 dB tuning range to the SLED standing wave cavity of 150 nm from 1600 – 1750 nm. When down-sweeping in wavelength the laser was able to operate at sweep rates of 10^5 nm/s with 0.2 – 0.4 nm estimated instantaneous linewidths and no drop in power from CW operation. These sweep rates are similar to those reported in previous semiconductor based, QC-AOTF tuned sources.

Chapter 6
Frequency compensating acousto-optic tunable filter pair

6.1 Introduction

The frequency shift associated with acousto-optic tunable filters (AOTFs) acts to broaden the output spectrum of lasers built with this device [16,114,115]. By constructing a compound device with two sequential AOTFs, the frequency shift of one can be made to compensate the other, resulting in a net frequency shift equal to the difference in driving frequencies of the AOTF pair. This allows a significant reduction in the net shift: from 10 – 100's of MHz to <100's of kHz. In the case where both AOTFs are driven at the same frequency there is no net frequency shift. Such a device is referred to here as a frequency compensating AOTF (FC-AOTF) pair.

Multiple lasers have been demonstrated using FC-AOTF pairs [11,16]. Previously, a Ti:Al_2O_3 laser was tuned with both a single AOTF and a FC-AOTF pair [115]. The single AOTF led to 0.14 nm linewidths while the FC-AOTF pair resulted in 0.01 nm linewidths. This suggests that utilising an FC-AOTF can lead to an improved linewidth while potentially retaining some of the advantages of the acousto-optic filter.

The aim of this chapter is to investigate the influence of a FC-AOTF pair on laser performance and compare it with the single quasi-collinear AOTF (QC-AOTF) from Chapter 5. The FC-AOTF pair was provided by the University of Southampton and Gooch & Housego, and is not a commercially available product. This device is first characterised when driven with no net frequency shift. It is then placed within the ring-cavity from Chapter 5, replacing the frequency shifting QC-AOTF previously used. This way, significant change in output behaviour can be attributed to the alternate tuning element. The cavity is characterised with the FC-AOTF pair driven to produce a variety of net frequency shifts to investigate the laser performance as a function of the shift.

6.2 FC-AOTF pair configuration

The configuration of the FC-AOTF pair used is shown in Figure 6.1. It consists of two sequential non-collinear AOTFs, operating in the parallel tangents regime discussed in Section 4.2.4. The input polarisation for the first AOTF is orthogonal to that of the second AOTF. Since the acousto-optic (AO) tuning relation is polarisation dependent, if the two AOTFs were to be identical then the second AOTF would need to be driven at a different frequency to make their filter bandwidths align, as can be seen in Figure 4.10. The unique feature of the FC-AOTF pair provided by Gooch and Housego is that the [001] and [110] crystal axes of the second AOTF are reversed. Thus, when driving the two AOTFs with the same frequency, the corresponding filter wavelengths can be identical [116].

Restricting the input to the FC-AOTF pair to a single polarisation as shown in Figure 6.1 leads to four possible output beams. Light that diffracts off only a single AOTF will have a frequency shift of $+f_1$ or $-f_2$, and has an orthogonal polarisation to the input. Light that diffracts off both AOTFs will have a net shift of $f_1 - f_2$, and both polarisation rotations result in identical input and outgoing polarisations. Undiffracted light that does not undergo AO interaction with either AOTF has no net shift and undergoes no change in polarisation. Additionally, this undiffracted light exits the 2nd AOTF parallel to light that has diffracted off both AOTFs.

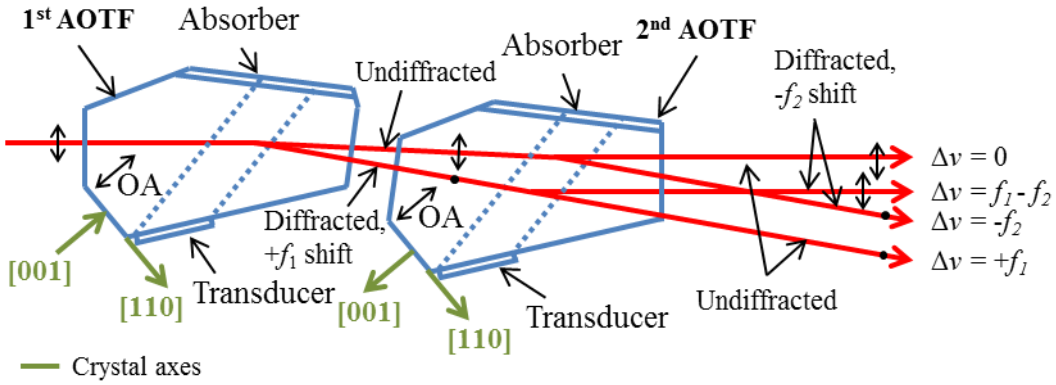

Figure 6.1 Non-collinear operation of the FC-AOTF pair for extraordinary polarised input light. OA = optical axis. f_1 = drive frequency of 1st AOTF, f_2 = drive frequency of 2nd AOTF, Δv = net frequency shift of light after exiting 2nd AOTF.

6.3 FC-AOTF pair characterisation

The setup for characterising the FC-AOTF pair when driving both AOTFs at the same frequency is shown in Figure 6.2. Only light diffracting off both AOTFs in Figure 6.1 is drawn, however in practice multiple beams may be present.

The QC-AOTF tuned superluminescent diode (SLED) source from Section 5.2 was used as the probe beam. A half-wave plate and polariser were used to rotate the input polarisation. The tuning curves for both input polarisations were measured using the method described in Chapter 4 for the single QC-AOTF. Diffraction efficiencies, optical bandwidths, and acoustic bandwidths were only measured for ordinary polarised input light. The finite apertures of the FC-AOTF pair resulted in clipping of the undiffracted light when passing through the second AOTF. The diffraction efficiency was thus defined by the ratio of the power in the diffracted light in Figure 6.2 to the input optical power to the FC-AOTF pair.

The non-collinear AOTF configuration for the FC-AOTF pair requires ~1 W of RF power per AOTF, and the acoustic frequency required for phase matching is ~60 MHz. To drive the AOTF pair, the signal from a waveform generator (BK Precision, 4064) was amplified with an RF amplifier (Minicircuits, ZHL-03-5WF+) before being sent to both AOTFs via a 50/50 RF splitter (Minicircuits, ZFSCJ-2-1+) and matched length coaxial cables.

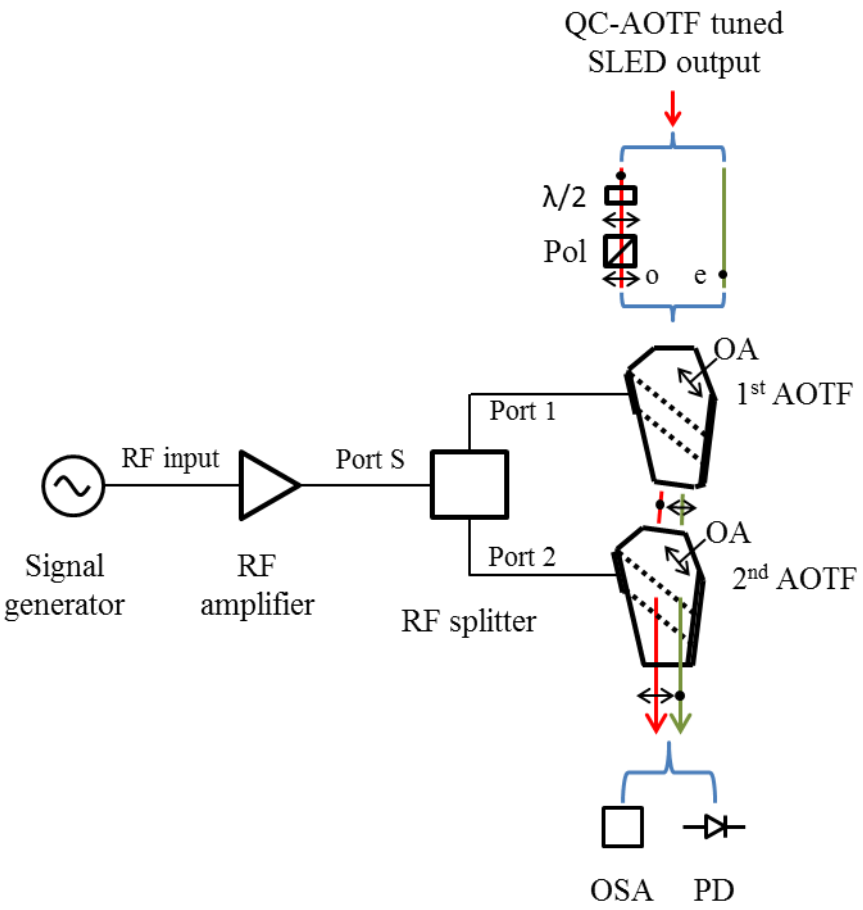

Figure 6.2 Schematic for characterisation of the FC-AOTF pair. Pol = polariser, λ/2 = half wave plate, o = ordinary input polarisation, e = extraordinary input polarisation, OSA = optical spectrum analyser, PD = photodiode.

The acoustic bandwidth of the FC-AOTF pair was measured by slowly sweeping the frequency for a fixed optical input and synchronously recording the output power using a photodiode.

The optical bandwidth of the FC-AOTF pair was measured as shown in Figure 6.3. The semiconductor optical amplifier (SOA) from Section 5.3 was used as a broadband source with its output collimated using an 8 mm focal length AR-coated aspheric lens. The spectrum of the light diffracted by both AOTFs was measured using an optical spectrum analyser (OSA, Yokagawa, AQ6375).

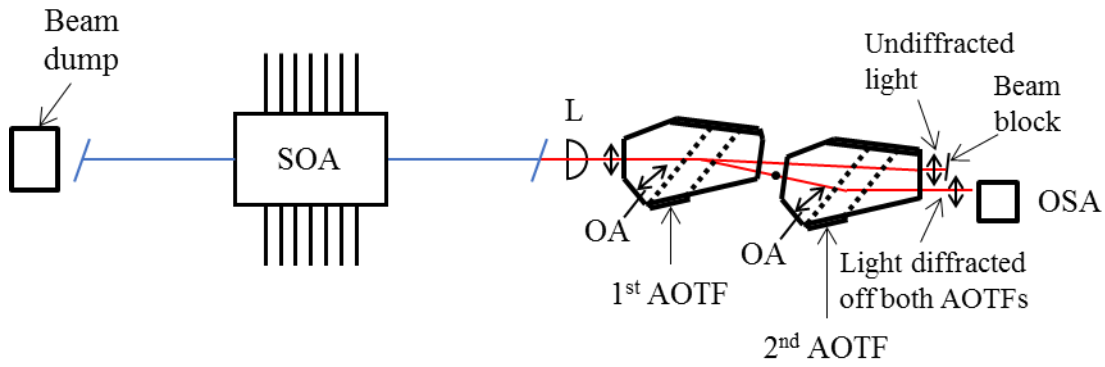

Figure 6.3 Schematic for characterisation of the optical filter bandwidth of the FC-AOTF pair. SOA = semiconductor optical amplifier, L = 8 mm focal length AR coated aspheric lens, OA = optical axis, OSA = optical spectrum analyser.

6.3.1 Results

The relation between interacting acoustic and optical frequencies for both extraordinary and ordinary input polarisations is shown Figure 6.4. The acoustic frequency separation between the two curves at a fixed optical wavelength is Δf ~400 kHz. The optical frequency separation for a fixed acoustic frequency is $\Delta\nu \sim 1$ THz ($\Delta\lambda \sim 9$ nm at 1650 nm).

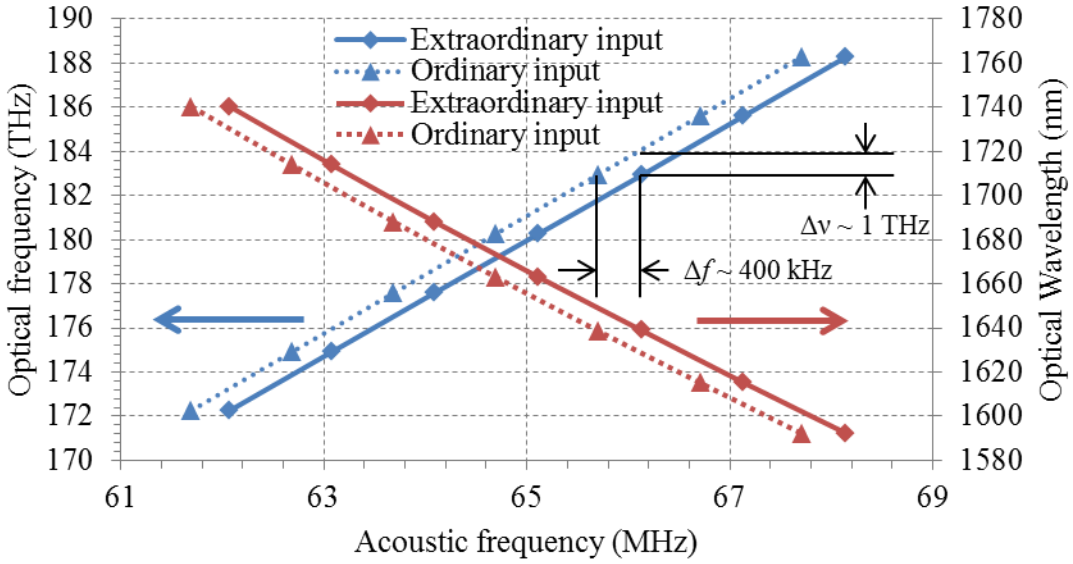

Figure 6.4 Tuning curve of FC-AOTF pair for both extraordinary and ordinary input polarisations.

The efficiency of the FC-AOTF pair relative to the input power for input wavelengths of 1592 nm to 1740 nm is shown in Figure 6.5. The efficiency decreased from ~85% at 1592 nm to ~75% at 1740 nm.

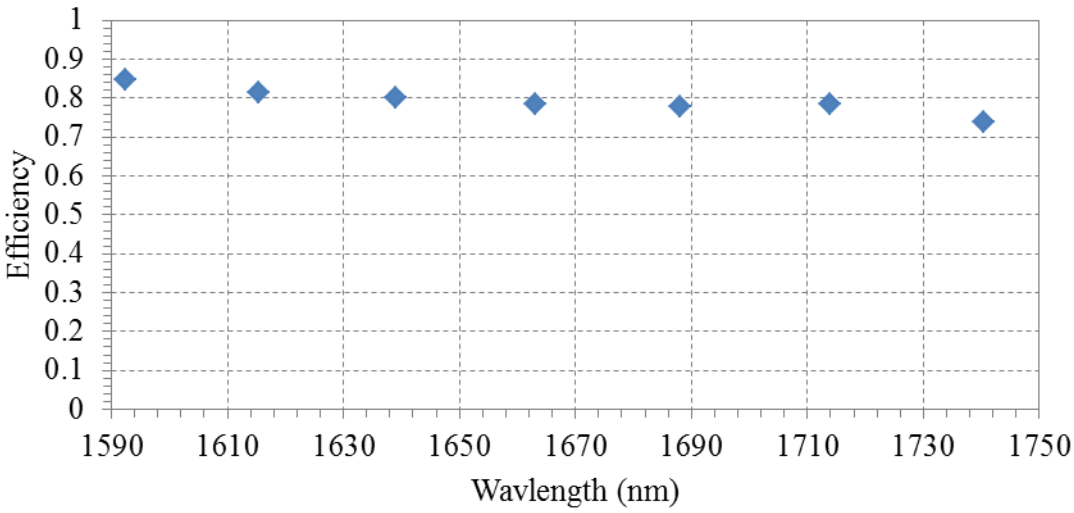

Figure 6.5 Diffraction efficiency of FC-AOTF pair for various input wavelengths.

The FC-AOTF acoustic frequency response for a fixed 1688 nm optical input is shown in Figure 6.6. The frequency response is symmetric about 64.1 MHz with a ~160 kHz full width at half maximum (FWHM).

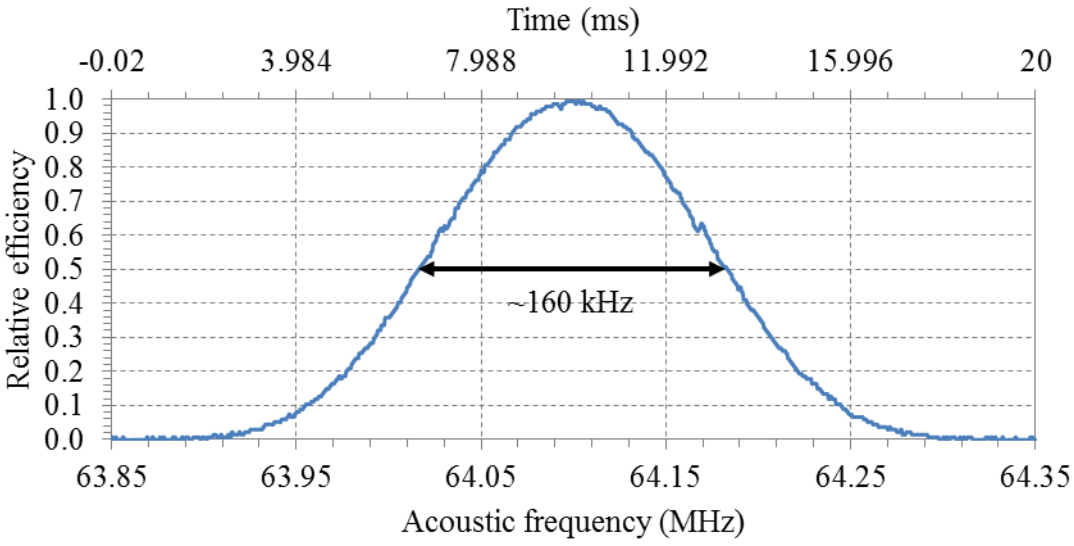

Figure 6.6 Acoustic filter bandwidth measurement of the FC-AOTF pair for an input wavelength of 1688 nm.

High and low resolution spectra of the FC-AOTF filter response to the broadband SOA is shown in Figure 6.7 and Figure 6.8. The high resolution spectrum shows a 3.7 nm FWHM optical bandwidth while the low resolution spectrum reveals side-lobes in the filter response ~9 nm away from the central peak with a ~28 dB side-lobe suppression.

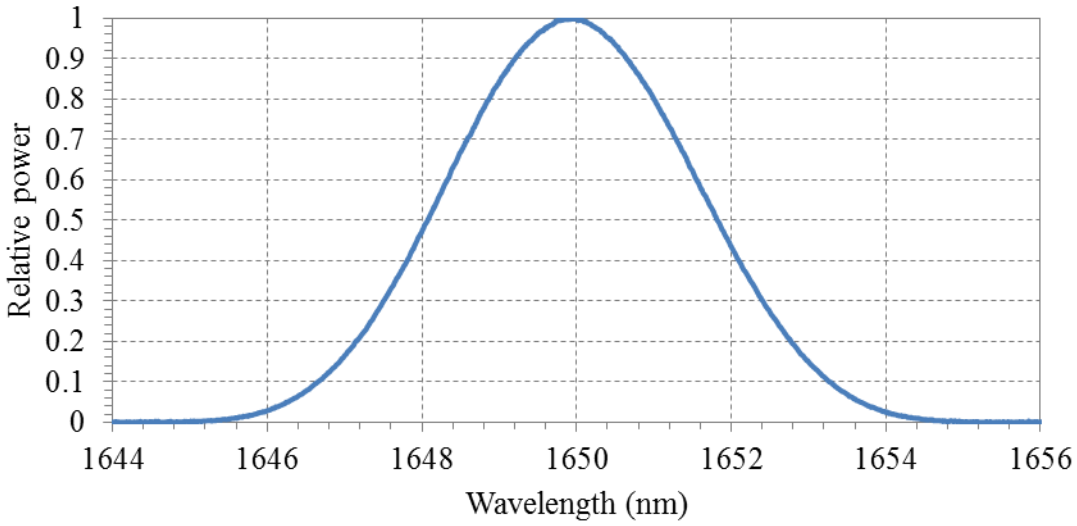

Figure 6.7 High resolution optical filter response of the FC-AOTF pair to the broadband output of the SOA. An OSA resolution setting of 0.05 nm was used.

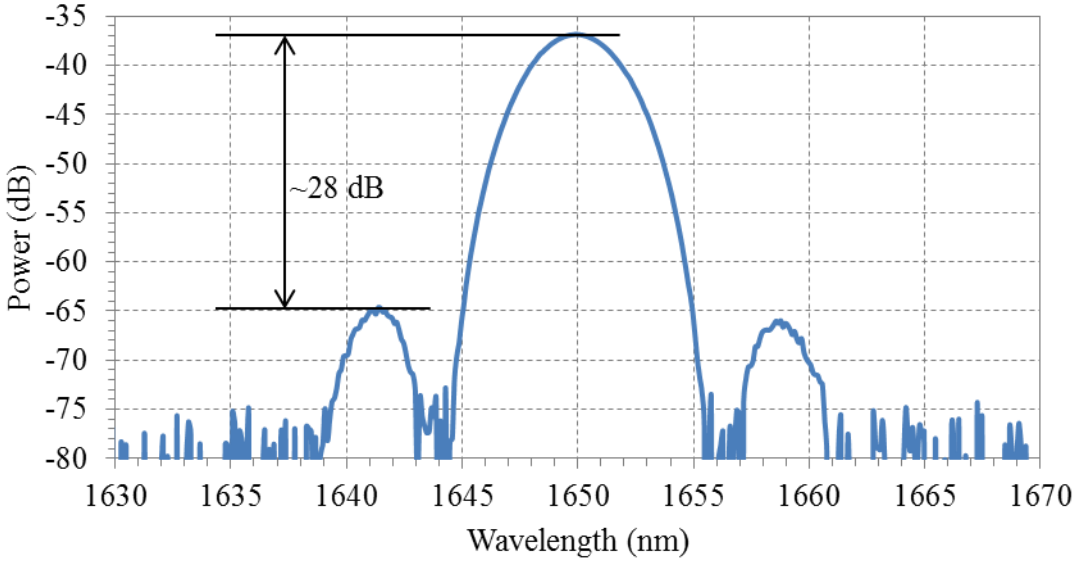

Figure 6.8 Low resolution optical filter response of the FC-AOTF pair to the broadband output of the SOA. An OSA resolution setting of 0.5 nm was used.

The temporal response of the FC-AOTF pair to a 8 µs RF pulse is shown in Figure 6.9. There is a ~7.2 µs latency before AO interaction occurs and a rise/fall time of ~4 µs, indicating a 4 µs AO interaction time.

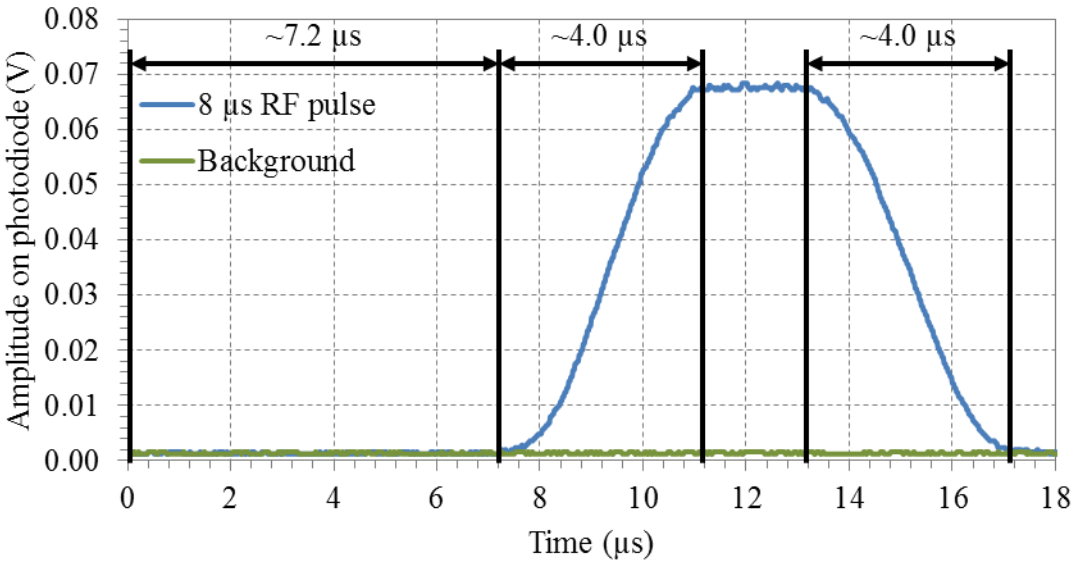

Figure 6.9 Oscilloscope trace of FC-AOTF response to 8 µs RF pulse. Time t = 0 corresponds to beginning of applied pulse.

6.3.2 Discussion

In the temporal measurement, the 8 µs RF pulse width applied would suggest that after the 4 µs rise time there is a further 4 µs operation at maximum efficiency before the trailing edge of the pulse enters the AO interaction region and efficiency decreases. However, maximum efficiency is only observed over a 2 µs period. This is attributed to a latency offset between the two AOTFs such that the acoustic wave of one AOTF reaches the AO interaction region before the other.

A comparison between the performance of the FC-AOTF pair and the single QC-AOTF used in Chapter 4 and 5 is shown in Table 6.1. The 60 – 70 MHz drive frequencies required to diffract light from 1580 – 1780 nm is larger than the ~30 MHz required for the single QC-AOTF, due to the different angles of acoustic and optical waves within the crystal. The larger drive power and broader acoustic and optical filter bandwidth of the FC-AOTF pair is understandable due to the shorter interaction time of non-collinear AOTFs compared with QC-AOTFs.

Table 6.1 Comparison between the single QC-AOTF used in Chapter 4 and 5 with the FC-AOTF pair.

	Single QC-AOTF	**FC-AOTF pair**
Drive power	~200 mW	~2 W total
Diffraction efficiency	~78%	~80%
Interacting drive frequency	~30 – 35 MHz	~60 – 70 MHz
Acoustic filter bandwidth	48 kHz at 1650 nm	160 kHz at 1688 nm
Optical filter bandwidth	2.4 nm at 1650 nm	3.7 nm at 1650 nm
Interaction time	21 μs	4 μs
Magnitude of net frequency shift	~30 – 35 MHz	<100 kHz

6.4 FC-AOTF tuned semiconductor optical amplifier ring cavity

The effect the FC-AOTF pair has on laser operation when used as an intra-cavity filter was tested with the ring-cavity from Section 5.3. The laser design is shown in Figure 6.10, and is similar to the QC-AOTF tuned ring-cavity. The FC-AOTF pair replaced the single QC-AOTF, and the input polarisation to the AOTF pair was extraordinary. Each AOTF was driven by a separate signal and amplifier to allow user control of the net frequency shift. The drive power to each AOTF was ~1 W, and the injection current to the SOA was 600 mA.

The laser was first characterised by measuring the output power as a function of wavelength when the FC-AOTF pair was driven to produce no net frequency shift. The power was measured with a thermal power meter (Thorlabs, S302C). The laser spectrum was then characterised as a function of net frequency shift using an optical spectrum analyser (OSA, Yokogawa, AQ6375).

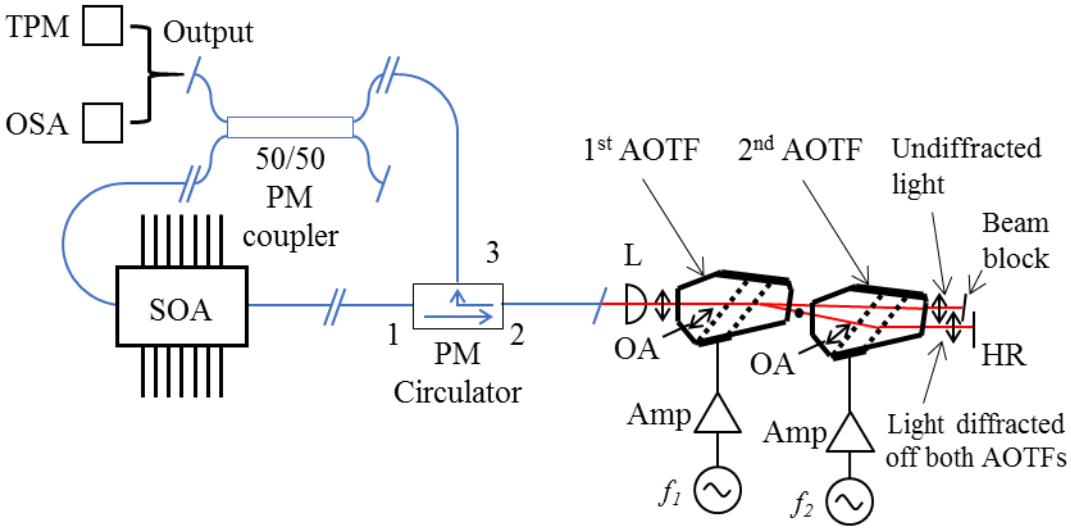

Figure 6.10 Cavity design for FC-AOTF tuned SOA cavity. SOA = semiconductor optical amplifier, L = 8 mm focal length AR-coated aspheric lens, OA = optical axis, Amp = RF amplifier, HR = highly reflective mirror, PM = polarisation maintaining, TPM = thermal power meter, OSA = optical spectrum analyser.

6.4.1 Results

The laser power as a function of wavelength is shown in Figure 6.11. Results from the equivalent QC-AOTF tuned ring-cavity from Figure 5.20 are overlaid for comparison. The laser had a ~6.8 mW peak power at ~1650 nm with a ~140 nm, 3 dB tuning range from 1590 – 1730 nm.

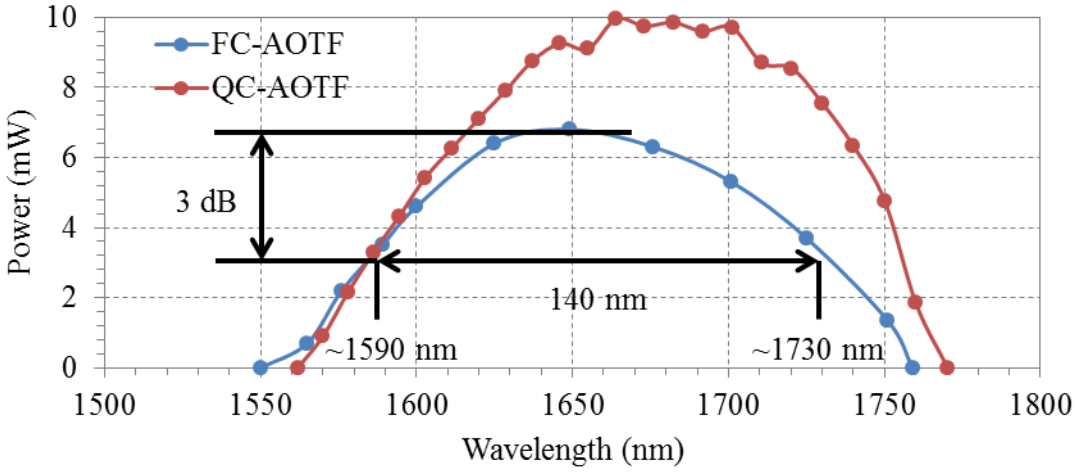

Figure 6.11 Laser powers at various wavelengths of the SOA ring cavities tuned with the FC-AOTF pair, and the single QC-AOTF.

The laser's spectral response at various closely spaced wavelengths for net frequency shifts of 0, +10, -10, +30, -30, +100, and -100 kHz are shown in Figure 6.12(a),(b),(c),(d),(e),(f) and (g) respectively. At 0 kHz, the spectral shape at the output varied as a function of operating wavelength, with the laser often running with multiple side-lobes. At certain drive frequencies, the side-lobes could be eliminated, resulting in narrow linewidths of ~0.07 nm FWHM, which were resolution limited by the OSA. However, the spectra were unstable and would transition between having none or multiple side-lobes.

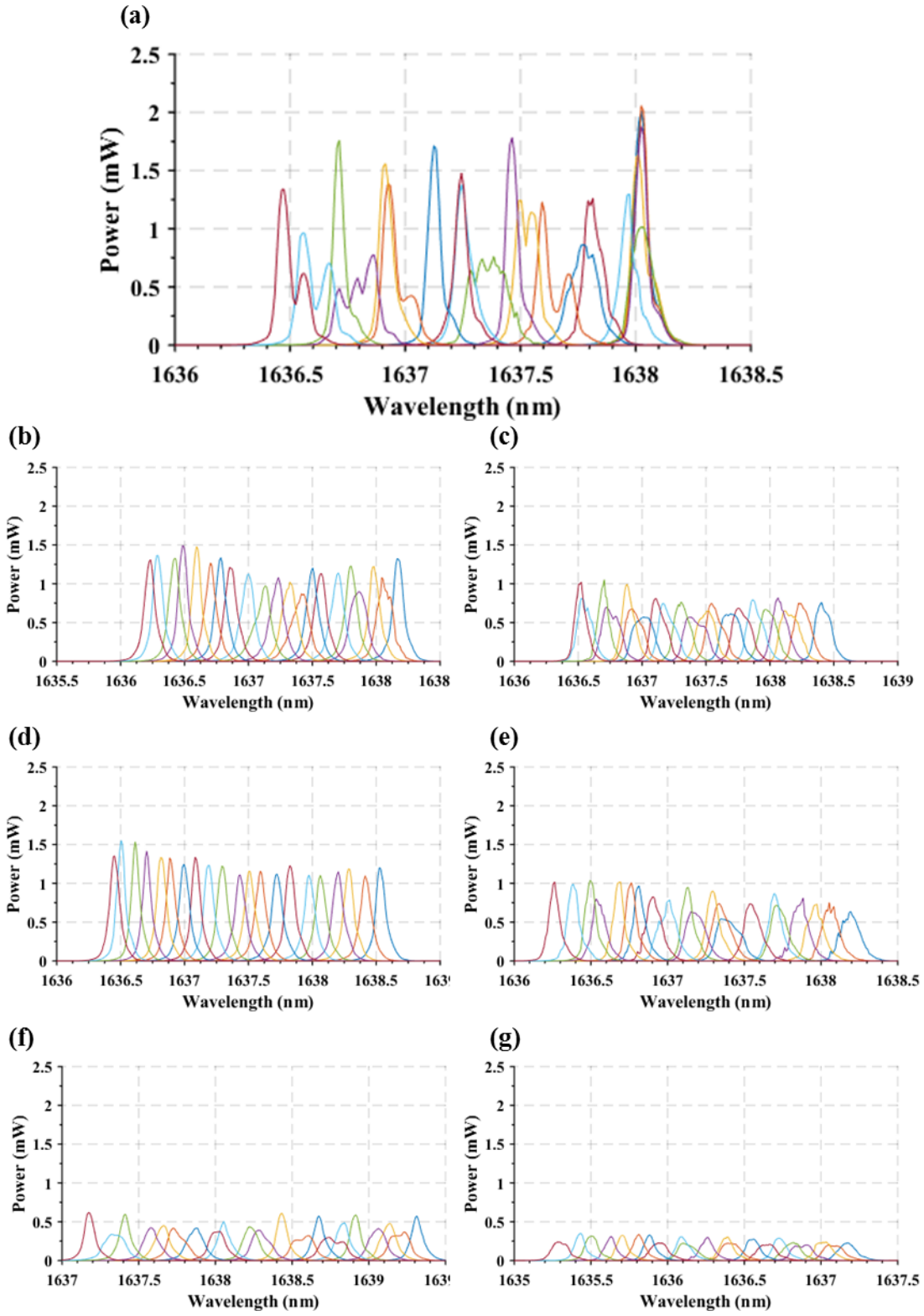

Figure 6.12 Laser spectra of FC-AOTF tuned cavity at closely spaced wavelengths for net frequency shifts of (a) 0 kHz, (b) 10 kHz, (c) -10 kHz, (d) +30 kHz, (e) -30 kHz, (f) +100 kHz, (g) -100 kHz. An OSA resolution setting of 0.05 nm was used.

When setting the frequency shift equal to ±10 kHz, the spectral shape did not vary as much, and did not exhibit side-lobes as often.

By increasing the frequency shift to +30 kHz, the side-lobes were eliminated at all measured wavelengths, and the spectra were more stable than those for all other frequency shifts. When using a -30 kHz frequency shift, the spectral shape still exhibited some variation across operating wavelengths.

Further increasing the magnitude of the frequency shift to ±100 kHz resulted in significant power reduction, and the spectra again displayed unwanted side-lobes and variation with wavelength. For frequency shifts with magnitudes beyond ~200 kHz, lasing was not observed.

A comparison between the spectra of the laser at ~1637 nm for a +30 kHz frequency shift with that from the single QC-AOTF tuned SOA cavity is shown in Figure 6.13. The +30 kHz frequency shift of the FC-AOTF pair is orders of magnitude smaller than the 35.6 MHz for the single QC-AOTF at this wavelength, and the ~0.1 nm resolution limited linewidth with the FC-AOTF pair is significantly narrower than the ~0.3 nm measured when tuning with the single QC-AOTF.

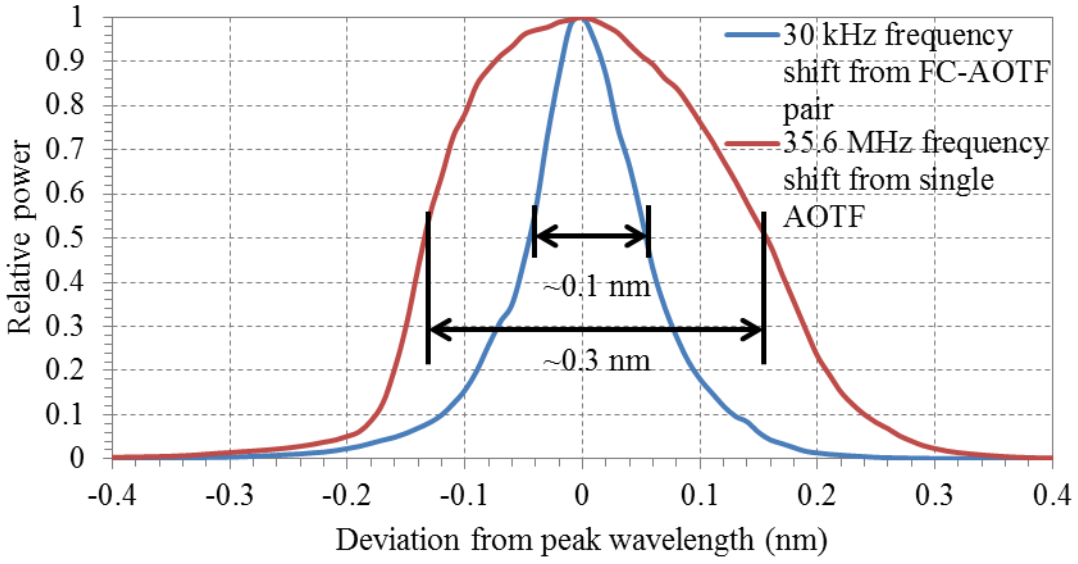

Figure 6.13 Comparison between spectra centred at 1637 nm for the SOA ring cavities tuned with the single QC-AOTF and the FC-AOTF pair. The QC-AOTF results in a 35.6 MHz frequency shift of the diffracted light while the FC-AOTF was driven to produce a +30 kHz frequency shift.

6.4.2 Comparison

The power and tuning ranges of the SOA ring-cavity when tuned with the FC-AOTF pair, driven to produce no net shift, was similar to the cavity tuned with a single QC-AOTF from Section 5.3. Both cavities had >140 nm, 3 dB tuning ranges with maximum power levels >5 mW.

A comparison between the spectral qualities of the two ring-cavities is shown in Table 6.2, with results from the FC-AOTF pair driven to produce both a 0 kHz and +30 kHz frequency shift included.

Etalon effects were not observed for the ~35 MHz shifts with the QC-AOTF. However, with a 0 kHz shift from the FC-AOTF pair, significant changes in spectral shape with operating wavelength were observed. This is attributed to the frequency shift per round trip of the cavities. The double pass of the AOTF per round trip leads to a ~70 MHz shift for the single QC-AOTF. This will act to both prevent the build-up of intra-cavity interference over multiple round trips, and broaden the laser's spectral output. When operating the FC-AOTF pair with no net shift narrower linewidths are possible, however interference is allowed to build up.

To narrow the linewidth of the SOA ring-cavity laser while avoiding intra-cavity interference, the FC-AOTF pair can be driven to produce a frequency shift that is both large enough to disturb intra-cavity interference, and small enough to avoid significantly broadening the spectral output. For the ring-cavity laser, a +30 kHz frequency shift was found to meet these requirements and led to 0.1 nm, resolution limited linewidths with no unwanted intra-cavity interference observed.

Table 6.2 Comparison between SOA ring cavity tuned with the single QC-AOTF and the FC-AOTF pair with 0 kHz and +30 kHz net shift.

	Single QC-AOTF	**FC-AOTF pair**	
Frequency shift	~35 MHz	0 kHz	+30 kHz
3 dB linewidth (nm)	0.3	0.07 (resolution limited) only when tuned to avoid side-lobes	0.1 (resolution limited)
Presence of etalon effect	No	Yes	No

When tuning the FC-AOTF pair with net frequency shifts of magnitude ≥100 kHz, the effect of intra-cavity interference was again observed in the spectrum. This is attributed to the reduced efficiency and change in the overall spectral filter shape of the FC-AOTF pair. For sufficiently large frequency separations the overlap of the individual filter passbands reduces, leading to a change in the overall filter shape, which becomes broader and less efficient. Consequently, when placed within a cavity this allows other intra-cavity feedback mechanisms such as etalons to influence the laser output, despite the frequency shift. If the FC-AOTF pair was designed such that the filter passbands of each AOTF overlapped when driven at frequencies separated by ±100 kHz, it should be possible to reduce the intra-cavity interference effect that was observed for frequency shifts of ±100 kHz in Figure 6.12, and the spectra should look similar to that for a +30 kHz frequency shift in the current system.

A more generalised comparison between sources tuned with a single AOTF and a FC-AOTF pair has not been made here since the single AOTF was based on quasi-collinear AO interaction while the FC-AOTF pair used non-collinear interaction. Future testing with other AOTF configurations would provide more generalised conclusions.

6.5 Summary

In this chapter, we examined the impact of the frequency compensating AOTF pair on the performance of the SOA ring-cavity and compared the results to those from Chapter 5. First, the FC-AOTF pair is characterised and compared with the single QC-AOTF. The larger drive power requirements and broader acoustic and optical filter bandwidths for the FC-AOTF can be attributed to its non-collinear AO interaction compared to the quasi-collinear interaction with the QC-AOTF.

Placing the FC-AOTF pair in the ring cavity and operating with no net frequency shift resulted in significant variation of spectral shape at the output as a function of operating wavelength. This differed from the performance of the cavity when tuned by a frequency shifting QC-AOTF. The difference in performance between the two laser cavities is attributed to the zero net frequency shift of the FC-AOTF pair, which allowed interference to build up over multiple round trips and rendered the cavity sensitive to etalon effects.

To prevent this interference from building up a small frequency shift was imposed with the FC-AOTF pair. It was found that a 30 kHz frequency shift was significant enough to disturb these intra-cavity interference effects while small enough to reduce the linewidth from the 0.3 nm observed with the QC-AOTF to <0.1 nm with the FC-AOTF pair (which was resolution limited by the OSA). To the best of our knowledge, this is the first demonstration of a frequency shifting AOTF being used to suppress intra-cavity interference and etalon effects in a tunable laser.

Chapter 7
Conclusion

7.1 Introduction

Throughout this thesis the performance and limitations of AOTF tuned semiconductor laser cavities were investigated. A number of AOTF tuned sources were characterised in constant wavelength, wavelength swept, and wavelength agile operation. Following this, the effect of the frequency shift caused by acousto-optic (AO) interaction was investigated by constructing a tunable source with a frequency compensating AOTF (FC-AOTF) pair. The aim of this section is to summarise the work done in each chapter, and present possible directions for future work.

7.2 Summary

In Chapter 1, a range of applications for tunable sources were presented, including laser surgery, optical coherence tomography, material processing, and differential light detection and ranging. The advantages an agile source which can be discretely tuned or rapidly swept in these applications were discussed.

In Chapter 2, the operating principles of tunable lasers were presented. This included the influence of the tunable filter and intra-cavity interference on the operating wavelength of a laser, and how a frequency shifting filter makes the condition for longitudinal cavity mode formation invalid. Several tuning mechanisms were compared, and the advantages of an AOTF identified. It provides agile purely electronic control of

the power and wavelength of the filtered light. Different gain media were compared, and semiconductors identified as being suitable for testing the performance of AOTF tuned sources owing to their broad tuning ranges and availability across all wavelengths >0.4 nm.

In Chapter 3, two tunable sources based on mechanical movement of diffraction gratings were developed. The first was a tunable thulium-doped fibre laser that was suitable for characterising OH absorption in bulk silica, which is of interest for possible upgrades to gravitational wave detectors. It operated from 1920 – 2060 nm, with powers ≥1.3 W. This fibre source currently supports other research activities within OzGrav. The second source was a standing wave, diffraction grating tuned cavity that used a superluminescent diode (SLED) as the gain medium. The source was broadly tunable and had an output power in the 5 – 10 mW range. Etalon effects from the SLED were present in the output, and were attributed to reflections from the diode facets. This source was important for subsequent characterisation of AOTFs.

In Chapter 4, the background theory of AOTF operation was presented, and a quasi-collinear AOTF (QC-AOTF) was characterised using the grating tuned source built in Chapter 3. The AOTF's maximum efficiency was ~78%, which occurred at 200 mW of RF drive power, which was within the specifications of the AOTF. The AOTF had an optical 3 dB filter bandwidth of ~2.4 nm and acoustic filter bandwidth of ~48 kHz. The 2.4 nm bandwidth was larger than the 2 nm specification, and was attributed to the alignment of the beam during this measurement and the beam diameter being smaller than recommended. Temporal measurements of the AOTF diffracted beam revealed a total 29 µs "switch on" and "switch off" time. This was comprised of an 8 µs latency and a 21 µs AO interaction region. The latency arose from the time for the acoustic wave to travel from the transducer to the input facet where it reflects and propagates along the AOTFs interaction region.

In Chapter 5, two electronically controlled, QC-AOTF tuned cavities were characterised. Agile operation of these sources was possible by avoiding inertial effects of mechanical tuning methods. The first source was a standing wave cavity which used the same SLED from the grating tuned source in Chapter 3. It had a broad 160 nm, 3 dB tuning range with powers >10 mW across this region. Similar to the diffraction grating tuned SLED cavity in Chapter 3, the laser displayed etalon effects in its spectrum, preferring to operate on longitudinal modes separated by ~0.3 nm which correspond to

resonance within the SLED chip. When operating as a swept source, the laser could sweep at rates up to 10^5 nm/s without significant spectral broadening or reduction in output power. However, etalon effects remained present. During wavelength agile operation, if discretely moving between wavelengths then 29 µs switch times were achieved, which corresponded to the switch time of the AOTF. However, during the transition between wavelengths significant power modulation occurred. It was possible to reduce power modulation during the switch by sweeping the laser between the two operating wavelengths.

The unwanted etalon effect was eliminated by constructing an AOTF tuned ring-cavity using a semiconductor optical amplifier (SOA) as the gain medium. The resulting tunable source had a similar 3 dB tuning range to the SLED standing wave cavity of 150 nm, with powers >5 mW across this region. No etalon effects were observed in the output spectrum, and linewidths of ~0.3 nm were achieved. During swept operation, instantaneous linewidths of $\sim 0.2 - 0.4$ nm were observed up to sweep rates of 2×10^5 nm/s. These sweep rates are similar to those previously reported in cavities tuned with a QC-AOTF. The instantaneous linewidth significantly narrowed when changing from constant wavelength operation to down-sweeping in wavelength at a rate of 1.38×10^4 nm/s. This was attributed to the sweep rate of the filter closely matching the rate of frequency shift due to AO interaction.

While the SLED standing wave cavity was a more compact cavity than the SOA ring cavity, in principle the ring cavity can be made compact by removing unnecessary fibre coupling. This would enable a compact, broadly tunable source in the mW level with fast sweep rates for a single AOTF-tuned semiconductor source.

In Chapter 6, the effect of the frequency shift from AO interaction on the output spectrum was investigated using a FC-AOTF pair. The QC-AOTF from the SOA ring cavity was replaced with the FC-AOTF pair, which allowed user control over the frequency shift of the diffracted light. When there was no frequency shift, interference was allowed to build up over multiple round trips, rendering the cavity sensitive to etalon effects. However, a +30 kHz frequency shift was significant enough to disturb these intra-cavity interference effects while being small enough to reduce the linewidth from the 0.3 nm observed with the QC-AOTF to <0.1 nm with the FC-AOTF. This is, to the best of our knowledge, the first demonstration of a frequency shifting AOTF being used to suppress intra-cavity interference and etalon effects.

Over the course of this project, an understanding of the qualities and limitations of AOTF-tuned sources has been developed. Sources with sweep rates similar to the fastest reported for QC-AOTF tuned devices were constructed, and the first demonstration of suppressing intra-cavity interference and etalon effects with frequency shifting AOTFs was presented.

7.3 Future work

The work undertaken in this project opens up areas for further research to be undertaken. These include gaining access to other wavelengths, and multi-wavelength operation.

7.3.1 Access to other wavelengths

The availability of direct bandgap semiconductors which can cover wavelengths from 0.4 – 2.2 µm allows AOTF-tuned sources to access these regions. Furthermore, the broad tuning range of AOTF's extends beyond the emission range of a single semiconductor, allowing the combination of gain stages which are tuned with a single AOTF. An example of such a configuration is shown in Figure 7.1, where the output of three semiconductors are combined via dichroics and sent through an AOTF which selects lasing off any one of the gain media. Similar gain stage combination has previously been demonstrated with diffraction grating tuned semiconductors [117] and AOTF tuned fibres [118,119].

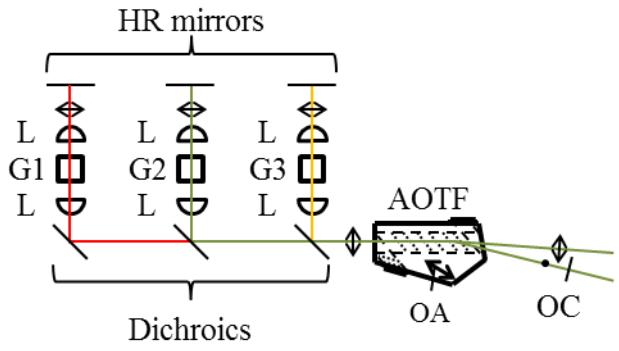

Figure 7.1 Example of AOTF tuned source using a combined gain stage of three semiconductors such that the output wavelength can be tuned across the full emission range of all three semiconductors. L = collimating lenses, G1,G2, and G3 = semiconductor gain media with differing emission wavelengths, OA = optical axis, AOTF = acousto-optic tunable filter, OC = output coupler.

Tunable mid-IR sources with powers <1 W could be achieved directly by an AOTF tuned quantum cascade laser (QCL) source. However, AOTF's operating in this wavelength region typically require large drive powers due its λ^2 dependence. Lower drive power AOTFs operating in the mid-IR require specially designed QC-AOTFs, or resonant acoustic AOTFs [95]. Alternatively, the mid-IR wavelengths could be accessed by the non-linear frequency conversion of AOTF tuned 2 µm sources. Access to the long wave IR has previously been demonstrated using this method with an AOTF tuned thulium-doped fibre laser [120].

7.3.2 Multi-wavelength operation

Throughout this thesis, the sources operated on a single wavelength. It is possible however to observe operation at multiple wavelengths because of the multi-wavelength filtering ability of AOTFs. Previously, multi-wavelength operation has been achieved by applying multiple RF frequencies to the AOTF simultaneously [12,121,122]. These sources suffer instabilities due to gain competition [12,121] and are susceptible to wavelength drift due to temperature variations of the AOTF [122]. Additionally, as the separation between the operating wavelengths decreases, beating between the RF drive frequencies will occur, leading to modulation in the output power [18].

Wavelength stability for dual wavelength operation has been improved by applying a third RF frequency such that the total RF power driving the AOTF remains the same [123]. An alternative way of achieving multi-wavelength operation which has not previously been investigated is to spatially separate the two acoustic frequencies within a QC-AOTF by modulating between RF frequencies, as shown in Figure 7.2. This could be advantageous for operating on closely spaced wavelengths as it avoids beating of the RF frequencies.

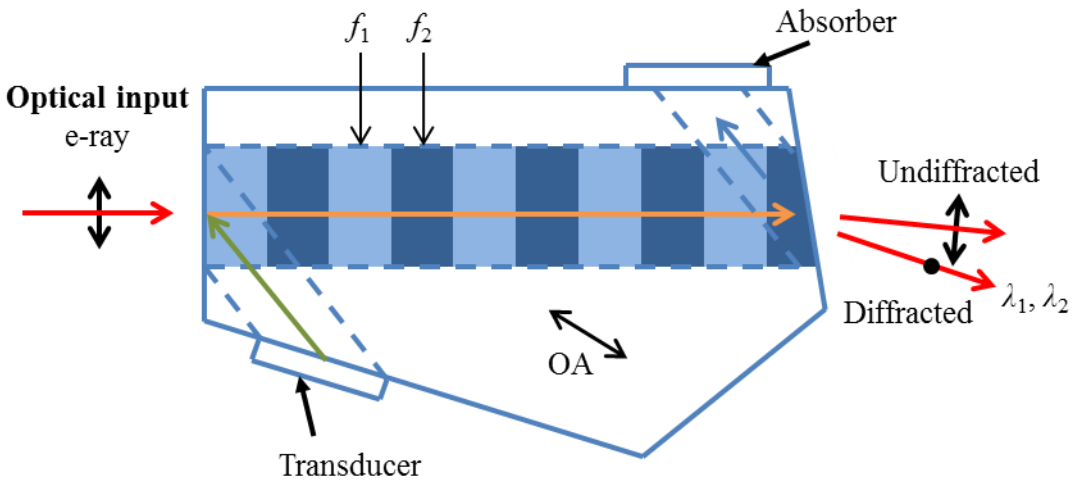

Figure 7.2 Possible method of dual wavelength operation in future work for AOTF tuned sources. The driving frequency to the AOTF is modulated between frequencies f_1 and f_2, which interact with optical wavelengths λ_1 and λ_2, respectively. Both frequencies may be present within the AO interaction region for fast enough modulation. Consequently, λ_1 and λ_2 can be simultaneously diffracted, allowing simultaneous lasing at both wavelengths. OA = optical axis.

References

[1] P. Cerny, “Developing thulium lasers for depth-selective scalpels,” *SPIE Newsroom*, 2006.

[2] V. J. Srinivasan, R. Huber, I. Gorczynska, J. G. Fujimoto, J. Y. Jiang, P. Reisen, and A. E. Cable, “High-speed, high-resolution optical coherence tomography retinal imaging with a frequency-swept laser at 850 nm,” *Opt. Lett.*, vol. 32, no. 4, pp. 361–363, 2007.

[3] O. O. Ahsen, Y. K. Tao, B. M. Potsaid, Y. Sheikine, J. Jiang, I. Grulkowski, T.-H. Tsai, V. Jayaraman, M. F. Kraus, J. L. Connolly, J. Hornegger, A. Cable, and J. G. Fujimoto, “Swept source optical coherence microscopy using a 1310 nm VCSEL light source,” *Opt. Express*, vol. 21, no. 15, pp. 18021–18033, 2013.

[4] C. L. Hagen and S. T. Sanders, “Investigation of multi-species (H_2O_2 and H_2O) sensing and thermometry in an HCCI engine by wavelength-agile absorption spectroscopy,” *Meas. Sci. Technol.*, vol. 18, no. 7, pp. 1992–1998, 2007.

[5] J. Barrientos Barria, A. Dobroc, H. Coudert-Alteirac, M. Raybaut, N. Cézard, J. B. Dherbecourt, T. Schmid, B. Faure, G. Souhaité, J. Pelon, J. M. Melkonian, A. Godard, and M. Lefebvre, “Simultaneous remote monitoring of atmospheric methane and water vapor using an integrated path DIAL instrument based on a widely tunable optical parametric source,” *Appl. Phys. B Lasers Opt.*, vol. 117, no. 1, pp. 509–518, 2014.

[6] W. Streifer and J. R. Whinnery, “Analysis of a dye laser tuned by acousto-optic filter,” *Appl. Phys. Lett.*, vol. 17, no. 8, pp. 335–337, 1970.

[7] D. J. Taylor, S. E. Harris, S. T. K. Nieh, and T. W. Hansch, “Electronic tuning of a dye laser using the acousto-optic filter,” *Appl. Phys. Lett.*, vol. 19, no. 8, pp. 269–271, 1971.

[8] S. Wada, K. Akagawa, and H. Tashiro, “Electronically tuned Ti : sapphire laser,” *Opt. Lett.*, vol. 21, no. 10, pp. 731–733, 1996.

[9] J. Geng, S. Wada, N. Saito, and H. Tashiro, “Frequency structure in an electronically tuned Ti:sapphire laser: periodic appearance of static fringes in

both homodyne and heterodyne Michelson interferometers," *Opt. Lett.*, vol. 24, no. 22, pp. 1635–1637, 1999.

[10] S. H. Yun, D. J. Richardson, D. O. Culverhouse, and B. Y. Kim, "Wavelength-Swept Fiber Laser with Frequency Shifted Feedback and Resonantly Swept Intra-Cavity Acoustooptic Tunable Filter," *IEEE J. Sel. Top. Quantum Electron.*, vol. 3, no. 4, pp. 1087–1096, 1997.

[11] G. A. Coquin and K. W. Cheung, "Electronically Tunable External-Cavity Semiconductor Laser," *Electron. Lett.*, vol. 24, no. 10, pp. 599–600, 1988.

[12] G. Coquin, K. W. Cheung, and M. M. Choy, "Single- and Multiple-Wavelength Operation of Acoustooptically Tuned Semiconductor Lasers at 1.3 μm," *Quantum Electron.*, vol. 25, no. 6, pp. 1575–1579, 1989.

[13] M. V. Shramenko, A. Chamorovskiy, H.-C. Lyu, A. a. Lobintsov, K. Karnowski, S. D. Yakubovich, and M. Wojtkowski, "Tunable semiconductor laser at 1025-1095 nm range for OCT applications with an extended imaging depth," *SPIE*, vol. 9312, p. 93123B, 2015.

[14] A. Chamorovskiy, "Superlum Application Note: Tunable Semiconductor Laser with Continuous Tuning in 880-1010 nm Spectral Range Application Note," 2015.

[15] N. Park, S. Chun, G.-H. Han, and C.-S. Kim, "Acousto-Optic–Based Wavelength-Comb-Swept Laser for Extended Displacement Measurements," *Sensors*, vol. 17, no. 4, p. 740, 2017.

[16] P. Zorabedian, "Tuning Fidelity of Acoustooptically Controlled External-Cavity Semiconductor Lasers," *Light. Technol.*, vol. 13, no. I, pp. 62–66, 1995.

[17] K. Scholle, S. Lamrini, P. Koopmann, and P. Fuhrberg, *2 μm Laser Sources and Their Possible Applications*, no. February 2010. 2010.

[18] J. M. O. Daniel, "Wavelength selection and transverse mode control in high power fibre lasers," University of Southampton, 2013.

[19] S. H. Kim, J. H. Kim, and S. W. Kang, “Nondestructive defect inspection for LCDs using optical coherence tomography,” *Displays*, vol. 32, no. 5, pp. 325–329, 2011.

[20] P. Targowski and M. Wojtkowski, “Optical Coherence Tomography for Artwork Diagnostics,” *Laser Chem.*, vol. 2006, no. 35373, pp. 1–11, 2006.

[21] C. S. Cheung, J. M. O. Daniel, M. Tokurakawa, W. A. Clarkson, and H. Liang, “Optical coherence tomography in the 2-μm wavelength regime for paint and other high opacity materials,” *Opt. Lett.*, vol. 39, no. 22, pp. 6509–6512, 2014.

[22] C. S. Cheung, M. Spring, and H. Liang, “Ultra-high resolution Fourier domain optical coherence tomography for old master paintings,” *Opt. Express*, vol. 23, no. 8, pp. 10145–10157, 2015.

[23] J. G. Fujimoto and W. Drexler, “Introduction to OCT,” in *Optical Coherence Tomography: Technology and Applications*, 2nd ed., W. Drexler and J. G. Fujimoto, Eds. Springer International Publishing Switzerland, 2015.

[24] Z. Michalewska and J. Nawrocki, *Atlas of Swept Source Optical Coherence Tomography*. Springer Nature, 2017.

[25] J. A. Izatt, M. A. Choma, and A.-H. Dhalla, “Theory of Optical Coherence Tomography,” in *Optical Coherence Tomography: Technology and Applications*, 2nd ed., W. Drexler and J. G. Fujimoto, Eds. Springer International Publishing Switzerland, 2015.

[26] C. D. Lu, M. F. Kraus, B. Potsaid, J. J. Liu, W. Choi, V. Jayaraman, A. E. Cable, J. Hornegger, J. S. Duker, and J. G. Fujimoto, “Handheld ultrahigh speed swept source optical coherence tomography instrument using a MEMS scanning mirror,” *Biomed. Opt. Express*, vol. 5, no. 1, pp. 293–311, 2014.

[27] A. Rodríguez Aramendía, “Ophthalmic long-range Swept-Source OCT imaging,” *BE-Optical*. [Online]. Available: http://beoptical.eu/Public/SharedDocs/Schools/BE-OPTICAL_Torun_RODRIGUEZ.pdf. [Accessed: 15-Apr-2019].

[28] H. Liang, R. Lange, B. Peric, and M. Spring, “Optimum spectral window for

imaging of art with optical coherence tomography," *Appl. Phys. B Lasers Opt.*, vol. 111, no. 4, pp. 589–602, 2013.

[29] C. S. Cheung, M. Tokurakawa, J. M. O. Daniel, W. A. Clarkson, and H. Liang, "Long wavelength optical coherence tomography for painted objects," *Opt. Arts, Archit. Archaeol. IV*, vol. 8790, no. May 2013, p. 87900J, 2013.

[30] A. Roesner, P. Abels, A. Olowinsky, N. Matsuo, and A. Hino, "Absorber-free laser beam welding of transparent thermoplastics," *Int. Congr. Appl. Lasers Electro-Optics*, vol. 2008, no. 1, p. M303, 2008.

[31] I. Mingareev, F. Weirauch, A. Olowinsky, L. Shah, P. Kadwani, and M. Richardson, "Welding of polymers using a 2 μm thulium fiber laser," *Opt. Laser Technol.*, vol. 44, no. 7, pp. 2095–2099, 2012.

[32] K. Ertel, H. Linné, and J. Bösenberg, "Injection-seeded pulsed Ti:sapphire laser with novel stabilization scheme and capability of dual-wavelength operation," *Appl. Opt.*, vol. 44, no. 24, p. 5120, 2005.

[33] S. M. Spuler, K. S. Repasky, B. Morley, D. Moen, M. Hayman, and A. R. Nehrir, "Field-deployable diode-laser-based differential absorption lidar (DIAL) for profiling water vapor," *Atmos. Meas. Tech.*, vol. 8, no. 3, pp. 1073–1087, 2015.

[34] M. Wirth, A. Fix, P. Mahnke, H. Schwarzer, F. Schrandt, and G. Ehret, "The airborne multi-wavelength water vapor differential absorption lidar WALES: System design and performance," *Appl. Phys. B Lasers Opt.*, vol. 96, no. 1, pp. 201–213, 2009.

[35] N. Simakov, "Development of components and fibres for the power scaling of pulsed holmium-doped fibre sources," University of Southampton Library, 2017.

[36] A. E. Siegman, *Lasers*. Mill Valley, Calif: University Science Books, 1986.

[37] C. Palmer, "The Physics of Diffraction Gratings," in *Diffraction Grating Handbook*, 5th ed., New York: Newport Corporation, 2005.

[38] M. Optics, “Fiber Fabry-Perot Tunable Filter | FFP-TF.” [Online]. Available: http://www.micronoptics.com/product/fiber-fabry-perot-tunable-filter-ffp-tf/. [Accessed: 09-Mar-2019].

[39] LightMachinery, “Etalon Designer - User’s Guide.” [Online]. Available: https://lightmachinery.com/optical-design-center/etalon-designer/. [Accessed: 12-Mar-2019].

[40] V. B. Voloshinov, “Control of optical radiation by means of collinear and non-collinear acousto-optic devices,” in *2001 IEEE Ultrasonics Symposium. Proceedings. An International Symposium (Cat. No.01CH37263*, 2002, pp. 483–492.

[41] J. T. (Joseph T. Verdeyen, *Laser Electronics*, 3rd ed. Englewood Cliffs, N.J.: Prentice Hall, 1994.

[42] N. P. Barnes, “Transition Metal Solid-State Lasers,” in *Tunable Lasers Handbook*, F. J. Duarte, Ed. San Diego: Academic Press, 1995, pp. 219–291.

[43] M. J. Weber, “Handbook of Laser Wavelengths,” CRC Press LLC, 1999.

[44] P. F. Moulton, “Spectroscopic and laser characteristics of Ti:Al_2O_3,” *J. Opt. Soc. Am. B*, vol. 3, no. 1, pp. 125–133, 1986.

[45] R. C. Powell, L. Xi, X. Gang, and G. Quarles, “Spectroscopic properties of alexandrite crystals,” *Phys. Rev. B, Condens. Matter*, vol. 32, no. September, pp. 2788–2797, 1985.

[46] “Gain medium - rare earth doped fibers,” *Kyoko Inc*. [Online]. Available: https://en.symphotony.com/fiber-lasers/re-doped-fibers/. [Accessed: 25-Feb-2019].

[47] “Semiconductor Lasers,” *RP-Photonics Encyclopedia*. [Online]. Available: https://www.rp-photonics.com/semiconductor_lasers.html. [Accessed: 30-Apr-2019].

[48] Z. Fang, H. Cai, G. Chen, and R. Qu, *Single Frequency Semiconductor Lasers*. Singapore: Springer Singapore, 2017.

[49] F. J. Duarte, *Tunable Lasers Handbook*. 1995.

[50] A. Joullié and P. Christol, "GaSb-based mid-infrared 2-5 μm laser diodes," *Comptes Rendus Phys.*, vol. 4, no. 6, pp. 621–637, 2003.

[51] S. N. Atutov, E. Mariotti, M. Meucci, P. Bicchi, C. Marinelli, and L. Moi, "A 670 nm external-cavity single mode diode laser continuously tunable over 18 GHz range," *Opt. Commun.*, vol. 107, no. 1–2, pp. 83–87, 1994.

[52] C. E. Wieman, K. B. MacAdam, A. Steinbach, and C. Wieman, "A narrow-band tunable diode laser system with grating feedback, and a saturated absorption spectrometer for Cs and Rb," *Collect. Pap. Carl Wieman*, vol. 60, no. 12, pp. 1098–1111, 1992.

[53] Wieman, Carl E. and Leo Hollberg, "Using diode lasers for atomic physics," *Rev. Sci. Instrum.*, vol. 62, no. 1, pp. 1–20, 1991.

[54] J. Reid, M. El-Sherbiny, B. K. Garside, and E. A. Ballik, "Sensitivity limits of a tunable diode laser spectrometer, with application to the detection of NO_2 at the 100-ppt level," *Appl. Opt.*, vol. 19, no. 19, pp. 3349–3354, 1982.

[55] G. Wysocki, R. Lewicki, R. F. Curl, F. K. Tittel, L. Diehl, F. Capasso, M. Troccoli, G. Hofler, D. Bour, S. Corzine, R. Maulini, M. Giovannini, and J. Faist, "Widely tunable mode-hop free external cavity quantum cascade lasers for high resolution spectroscopy and chemical sensing," *Appl. Phys. B Lasers Opt.*, vol. 92, no. 3 SPECIAL ISSUE, pp. 305–311, 2008.

[56] E. de Clercq, G. D. Rovera, S. Bouzid, and A. Clairon, "The LPTF Optically Pumped Primary Frequency Standard," *IEEE Trans. Instrum. Meas.*, vol. 42, no. 2, pp. 457–461, 1993.

[57] M. J. T. Milton, T. D. Gardiner, G. Chourdakis, and P. T. Woods, "Injection seeding of an infrared optical parametric oscillator with a tunable diode laser," *Opt. Lett.*, vol. 19, no. 4, pp. 281–283, 1994.

[58] B. Maisenbacher, E. Leckel, R. Jahn, and M. Pott, "Tunable Laser Source for

Optical Amplifier Testing," *Hewlett-Packard J.*, vol. 44, no. 1, pp. 11–19, 1993.

[59] "LIGO Scientific Collaboration Technical Note: Instrument Science White Paper 2018," 2018.

[60] E. Geerlings, M. Rattunde, J. Schmitz, G. Kaufel, H. Zappe, and J. Wagner, "Widely tunable GaSb-based external cavity diode laser emitting around 2.3 μm," *IEEE Photonics Technol. Lett.*, vol. 18, no. 18, pp. 1913–1915, 2006.

[61] T. Kanai, N. Fujiwara, Y. Ohiso, H. Ishii, M. Shimokozono, and M. Itoh, "2 μm wavelength tunable distributed Bragg reflector laser," *IEICE Electron. Express*, vol. 13, no. 16, pp. 1–5, 2016.

[62] Spectra-Physics, "Velocity Widely Tunable Laser, 1975-2075 nm, Model TLB-6736." [Online]. Available: https://www.newport.com/p/TLB-6736.

[63] W. A. Clarkson, N. P. Barnes, P. W. Turner, J. Nilsson, and D. C. Hanna, "High-power cladding-pumped Tm-doped silica fiber laser with wavelength tuning from 1860 to 2090 nm," *Opt. Lett.*, vol. 27, no. 22, pp. 1989–1991, 2002.

[64] V. Sudesh, T. S. McComb, L. Shah, P. Kadwani, M. Richardson, C. C. C. Willis, and R. A. Sims, "High-power widely tunable thulium fiber lasers," *Appl. Opt.*, vol. 49, no. 32, pp. 6236–6242, 2010.

[65] P. Peterka, I. Kasik, A. Dhar, B. Dussardier, and W. Blanc, "Theoretical modeling of fiber laser at 810 nm based on thulium-doped silica fibers with enhanced $^3H_4$ level lifetime," *Opt. Express*, vol. 19, no. 3, p. 2773, 2011.

[66] "SAF Gain Chips, 1650 nm Center Wavelength," *Thorlabs*. [Online]. Available: https://www.thorlabs.com/newgrouppage9.cfm?objectgroup_id=4046&pn=SAF1091H. [Accessed: 02-Feb-2019].

[67] U. Koren, "Waveguide Based Photonic Integrated Circuits," in *Optoelectronic Integration: Physics, Technology and Applications*, O. Wada, Ed. Boston, MA: Springer US, 1994, pp. 233–272.

[68] "Single Frequency Lasers Tutorial: ECL Tutorial," *Thorlabs*. [Online]. Available: https://www.thorlabs.com/newgrouppage9.cfm?objectgroup_id=9024&tabname=

ECL Tutorial. [Accessed: 03-Feb-2019].

[69] M. R. Matthews, K. H. Cameron, R. Wyatt, and W. J. Devlin, “Packaged frequency-stable tunable 20 kHz linewidth 1.5 μm InGaAsP external cavity laser,” *Electron. Lett.*, vol. 21, no. 3, pp. 113–115, 1985.

[70] S. Saito, O. Nilsson, and Y. Yamamoto, “Oscillation Center Frequency Tuning, Quantum F M Noise, and Direct Frequency Modulation Characteristics,” *Quantum Electron.*, vol. 18, no. 6, pp. 961–970, 1982.

[71] R. Ludeke and E. P. Harris, “Tunable GaAs laser in an external dispersive cavity,” *Appl. Phys. Lett.*, vol. 20, no. 12, pp. 499–500, 1972.

[72] E. T. Peng and C. B. Su, “Properties of an external-cavity traveling-wave semiconductor ring laser,” *Opt. Lett.*, vol. 17, no. 1, pp. 55–57, 1992.

[73] P. Zorabedian and W. R. J. Trutna, “Alignment-stabilized grating-tuned external-cavity semiconductor laser,” *Opt. Lett.*, vol. 15, no. 9, pp. 483–485, 1990.

[74] M. G. Littman and H. J. Metcalf, “Spectrally narrow pulsed dye laser without beam expander,” *Appl. Opt.*, vol. 17, no. 14, pp. 2224–2227, 1978.

[75] N. S. Claxton, T. J. Fellers, and M. W. Davidson, “Laser Scanning Confocal Microscopy,” *Dep. Opt. Microsc. Digit. Imaging, Florida State Univ. Tallahassee*, 2006.

[76] Zeiss, *LSM 510 laser scanning microscope*. 1998.

[77] K. W. Cheung, M. M. Choy, and H. Kobrinski, “Electronic Wavelength Tuning Using Acoustooptic Tunable Filter with Broad Continuous Tuning Range and Narrow Channel Spacing,” *IEEE Photonics Technol. Lett.*, vol. 1, no. 2, pp. 38–40, 1989.

[78] J. L. Jackel, M. S. Goodman, J. E. Baran, W. J. Tomlinson, G. Chang, S. Member, M. Z. Iqbal, G. H. Song, K. Bala, C. A. Brackett, D. A. Smith, S. Member, R. S. Chakravarthy, S. Member, R. H. Hobbs, D. J. Fritz, R. W. Ade,

and K. M. Kissa, “Acousto-Optic Tunable Filters (AOTF’s) for Multiwavelength Optical Cross-Connects: Crosstalk Considerations,” *J. Light. Technol.*, vol. 14, no. 6, pp. 1056–1066, 1996.

[79] H. Issa, V. Quintard, A. Pérennou, and A. Sakkour, “Double pass in acousto-optic tunable filter for telecommunication network,” *Opt. Eng.*, vol. 53, no. 7, p. 75103, 2014.

[80] C. Stedham, M. Draper, J. Ward, E. Wachman, and C. Pannell, “A novel acousto-optic tunable filter for use in hyperspectral imaging systems,” 2008.

[81] L. Gao, S. I. Herriot, and K. H. Wagner, “Novel approach to RF photonic signal processing using an ultrafast laser comb modulated by traveling-wave tunable filters,” *IEEE J. Sel. Top. Quantum Electron.*, vol. 12, no. 2, pp. 315–329, 2006.

[82] O. Kozlova, A. Sadouni, D. Truong, S. Briaudeau, and M. Himbert, “Tunable transportable spectroradiometer based on an acousto-optical tunable filter: Development and optical performance,” *Rev. Sci. Instrum.*, vol. 87, no. 12, p. 125101, 2016.

[83] J. Xu and R. Stroud, *Acousto-optic devices: principles, design, and applications*. New York: Wiley, 1992.

[84] S. Valle, “Design and application of high performance Acousto-Optic Tunable Filters,” University of Glasgow (United Kingdom), 2017.

[85] N. Uchida, “Optical Properties of Single-Crystal Paratellurite (TeO_2),” *Phys. Rev. B*, vol. 4, no. 10, pp. 3736–3745, 1971.

[86] J. G. Berny, J. P. Bourgoin, and B. Ayrault, “Dispersion des indices de refraction du molybdate de plomb (PbMoO4) et de la paratellurite (TeO2),” *Opt. Commun.*, vol. 6, no. 4, pp. 383–387, 1972.

[87] G. Georgiev, D. A. Glenar, and J. J. Hillman, “Spectral characterization of acousto-optic filters used in imaging spectroscopy,” *Appl. Opt.*, vol. 41, no. 1, pp. 209–217, 2002.

[88] Y. Ohmachi, N. Uchida, and N. Niizeki, “Acoustic Wave Propagation in TeO2 Single Crystal,” *J. Acoust. Soc. Am.*, vol. 51, no. 1B, pp. 164–168, 1972.

[89] P. A. Gass and J. R. Sambles, “Accurate design of a noncollinear acousto-optic tunable filter,” *Opt. Lett.*, vol. 16, no. 6, pp. 429–431, 1991.

[90] S. E. Harris and R. W. Wallace, “Acousto-optic tunable filter,” *J. Opt. Soc. Am.*, vol. 59, no. 6, pp. 744–747, 1969.

[91] J. A. Kusters, D. A. Wilson, and D. L. Hammond, “Optimum crystal orientation for acoustically tuned optical filters,” *J. Opt. Soc. Am.*, vol. 64, no. 4, pp. 434–440, 1974.

[92] T. Yano and A. Watanabe, “New noncollinear acousto-optic tunable filter using birefringence in paratellurite,” *Appl. Phys. Lett.*, vol. 24, no. 6, pp. 256–258, 1974.

[93] I. C. Chang, “Noncollinear acousto-optic filter with large angular aperture,” *Appl. Phys. Lett.*, vol. 25, no. 7, pp. 370–372, 1974.

[94] V. B. Voloshinov, “Close to collinear acousto-optical interaction in paratellurite,” *Opt. Eng.*, vol. 31, no. 10, pp. 2089–2094, 1992.

[95] J. D. Ward, S. Valle, C. Pannell, and N. P. Johnson, “Acousto-Optic Tunable Filters (AOTFs) Optimised for Operation in the 2-4μm region,” in *Journal of Physics: Conference Series*, 2015, vol. 619, pp. 1–4.

[96] V. Quintard, H. Issa, and A. Pérennou, “Dynamic Behavior of a Multi-wavelength Acousto-optic Filter,” *Phys. Procedia*, vol. 70, pp. 770–773, 2015.

[97] V. Y. Molchanov, V. B. Voloshinov, and O. Y. Makarov, “Quasi-collinear tunable acousto-optic paratellurite crystal filters for wavelength division multiplexing and optical channel selection,” *Quantum Electron.*, vol. 39, no. 4, pp. 353–360, 2009.

[98] E. V. Andreeva, S. N. Il’chenko, M. A. Ladugin, A. A. Lobintsov, A. A. Marmalyuk, M. V. Shramenko, and S. D. Yakubovich, “Broadband semiconductor optical amplifiers of the spectral range 750 - 1100 nm,” *Quantum Electron.*, vol. 43, no. 11, pp. 994–998, 2013.

[99] V. B. Voloshinov and N. V. Polikarpova, “Acousto-optic investigation of propagation and reflection of acoustic waves in paratellurite crystal,” *Appl. Opt.*, vol. 48, no. 7, pp. C55–C66, 2009.

[100] V. M. Kodach, D. J. Faber, and T. G. Van Leeuwen, “Wavelength swept Ti:sapphire laser,” *Opt. Commun.*, vol. 281, no. 19, pp. 4975–4978, 2008.

[101] T. P. Lee and C. E. Zah, “Wavelength-Tunable and Single-Frequency Semiconductor Lasers for Photonic Communications Networks,” *IEEE Commun. Mag.*, vol. 27, no. 10, pp. 42–52, 1989.

[102] M. V Shramenko, E. V Andreeva, D. S. Mamedov, V. R. Shidlovski, and S. D. Yakubovich, “NIR semiconductor laser with fast broadband tuning,” in *SPIE*, 2006, vol. 6079, p. 60791M–1–60791M–8.

[103] E. V Andreeva, P. I. Lapin, V. V Prokhorov, V. R. Shidlovski, M. V Shramenko, and S. D. Yakubovich, “Novel Superluminescent Diodes and SLD-based Light Sources for Optical Coherence Tomography,” in *Optical Coherence Tomography and Coherence Techniques III*, 2007, vol. 6627, p. 662703.

[104] Y. O. Kostin, M. A. Ladugin, A. A. Lobintsov, A. A. Marmalyuk, A. Y. Chamorovsky, M. V Shramenko, and S. D. Yakubovich, “Semiconductor lasers with a continuous tuning range above 100 nm in the nearest IR spectral region,” *Quantum Electron.*, vol. 45, no. 8, pp. 697–700, 2015.

[105] G.-H. Han, S.-W. Cho, N. S. Park, C.-S. Kim, and S. C. Bondy, “Electro-Optic Swept Source Based on AOTF for Wavenumber-Linear Interferometric Sensing and Imaging,” *Fibers*, vol. 4, no. 14, 2016.

[106] A. Chamorovskiy, M. V. Shramenko, A. A. Lobintsov, and S. D. Yakubovich, “Narrow linewidth broadband tunable semiconductor laser at 840 nm with dual acousto-optic tunable configuration for OCT applications,” *SPIE*, vol. 9697, p. 96972T, 2016.

[107] V. R. Shidlovskii, S. N. Ilchenko, A. A. Lobintsov, M. V. Shramenko, and S. D. Yakubovich, “High-power sweeping semiconductor light sources at 840 nm with up to 100 nm tuning range,” in *Optical Coherence Tomography and Coherence Domain Optical Methods in Biomedicine XVI*, 2012, vol. 8213, p. 82133A.

[108] Superlum, “Swept Wavelength Tunable Semiconductor Lasers, Broadsweepers.” [Online]. Available: https://www.superlumdiodes.com/broadsweepers.htm. [Accessed: 01-Aug-2018].

[109] A. Gambell, N. Simakov, M. Ganija, P. J. Veitch, A. Hemming, J. Haub, J. Munch, and J. M. O. Daniel, “A Tunable Laser from 1610 – 1760 nm Using a Narrowband Acousto-Optic Tunable Filter,” in *Australia and New Zealand Conference on Optics and Photonics 2017 (ANZCOP 2017)*, 2017.

[110] M. Choma, M. Sarunic, C. Yang, and J. Izatt, “Sensitivity advantage of swept source and Fourier domain optical coherence tomography,” *Opt. Express*, vol. 11, no. 18, pp. 2183–9, 2003.

[111] B. R. Biedermann, W. Wieser, C. M. Eigenwillig, T. Klein, and R. Huber, “Dispersion, coherence and noise of fourier domain mode locked lasers,” *Opt. Express*, vol. 17, no. 12, pp. 9947–9961, 2009.

[112] B. R. Biedermann, W. Wieser, C. M. Eigenwillig, T. Klein, and R. Huber, “Direct measurement of the instantaneous linewidth of rapidly wavelength-swept lasers,” *Opt. Lett.*, vol. 35, no. 22, pp. 3733–3735, Nov. 2010.

[113] Thorlabs, “L-Band Booster Optical Amplifiers (BOAs), 1590 - 1625 nm.” [Online]. Available: https://www.thorlabs.com/newgrouppage9.cfm?objectgroup_id=3991.

[114] Y. Wang, N. Saito, S. Wada, and H. Tashiro, “Narrowband, Widely Electronically Tuned Ti:Sapphire Laser,” in *Summaries of Papers Presented at the Lasers and Electro-Optics. CLEO ’02. Technical Diges*, 2002, vol. 1, pp. 508–509.

[115] Y. Wang, N. Saito, S. Wada, and H. Tashiro, “Narrow-band , widely electronically tuned frequency-shifted feedback laser,” *Opt. Lett.*, vol. 27, no. 7, pp. 515–517, 2002.

[116] J. D. Ward and C. N. Pannell, “Matched pair of AOTFs with net zero frequency-

shift," *Phys. Procedia*, vol. 70, no. 0, pp. 914–917, 2015.

[117] W. Y. Oh, S. H. Yun, G. J. Tearney, and B. E. Bouma, "Wide tuning range wavelength-swept laser with two semiconductor optical amplifiers," *IEEE Photonics Technol. Lett.*, vol. 17, no. 3, pp. 678–680, 2005.

[118] J. M. O. Daniel, M. Tokurakawa, and W. A. Clarkson, "Power-scalable wavelength-agile fibre laser source at two-microns," in *5th EPS-QEOD Europhoton '12 (31/08/12)*, 2012, no. August, p. 17.

[119] M. Tokurakawa, J. M. O. Daniel, C. S. Chenug, H. Liang, and W. A. Clarkson, "Ultra-broadband wavelength-swept Tm-doped fiber laser using wavelength-combined gain stages," *Opt. Express*, vol. 23, no. 1, p. 471, 2015.

[120] F. Gutty, A. Grisard, C. Larat, D. Papillon, M. Schwarz, B. Gerard, R. Ostendorf, M. Rattunde, J. Wagner, and E. Lallier, "140 W peak power laser system tunable in the LWIR," *Opt. Express*, vol. 25, no. 16, p. 18897, 2017.

[121] N. Saito, S. Wada, and H. Tashiro, "Dual-wavelength oscillation in an electronically tuned Ti:sapphire laser," *J. Opt. Soc. Am. B*, vol. 18, no. 9, p. 1288, 2001.

[122] M. Yumoto, Y. Maeda, N. Saito, T. Ogawa, M. Yamashita, and S. Wada, "Multi-wavelength spectroscopic application using rapid and random wavelength-tuned mid-infrared light source," *Jpn. J. Appl. Phys.*, vol. 49, no. 1, p. 10209, 2010.

[123] M. Yumoto, Y. Maeda, N. Saito, T. Ogawa, M. Yamashita, and S. Wada, "Wavelength stabilization of dual-wavelength oscillation in electronically tuned Ti:Al2O3 laser," *Appl. Phys. Express*, vol. 3, no. 1, p. 12701, 2010.